



FABRICATION AND CHARACTERIZATION OF HIGH  
EFFICIENCY III-NITRIDE/ORGANIC HYBRID  
NANO-STRUCTURES FOR SOLID STATE WHITE LIGHTING

A THESIS  
SUBMITTED FOR THE DEGREE OF DOCTOR OF PHILOSOPHY (PH.D.)  
IN THE DEPARTMENT OF ELECTRONIC AND ELECTRICAL  
ENGINEERING

THE RESULTS, DISCUSSIONS AND CONCLUSIONS PRESENTED HEREIN ARE IDENTICAL TO THOSE IN THE PRINTED VERSION. THIS ELECTRONIC VERSION OF THE THESIS HAS BEEN EDITED SOLELY TO ENSURE CONFORMANCE WITH COPYRIGHT LEGISLATION AND ALL EXCISIONS ARE NOTED IN THE TEXT. THE FINAL, AWARDED AND EXAMINED VERSION IS AVAILABLE FOR CONSULTATION VIA THE UNIVERSITY LIBRARY.

**RICHARD SMITH**

**Supervisor: Professor Tao Wang**

THE UNIVERSITY OF SHEFFIELD  
2013



---

# Contents

---

<b>Abstract</b>	<b>7</b>
<b>Acknowledgements</b>	<b>9</b>
<b>1 Introduction</b>	<b>13</b>
1.1 Introduction . . . . .	13
1.1.1 The Energy Crisis . . . . .	13
1.1.2 Lighting Technologies . . . . .	14
1.2 The History of Nitride Semiconductors . . . . .	15
1.3 Current Challenges and Limitations . . . . .	18
References . . . . .	23
<b>2 Background</b>	<b>28</b>
2.1 Semiconductors . . . . .	28
2.1.1 Band Structure . . . . .	28
2.1.2 Electrons, Holes and Excitons . . . . .	30
2.1.3 Doping . . . . .	31
2.1.4 Compound semiconductors . . . . .	31
2.1.5 Semiconductor Optics . . . . .	32
2.1.6 Optical Transitions in Semiconductors . . . . .	32
2.1.7 Low Dimensional Structures . . . . .	34
2.1.8 p-n Junctions . . . . .	35
2.2 III-nitride Semiconductors . . . . .	37
2.2.1 Crystal Structure . . . . .	37
2.2.2 Polarization and the Quantum Confined Stark Effect . . . . .	37
2.2.3 Growth of III-Nitride Materials . . . . .	38
2.2.4 Substrates . . . . .	39
2.2.5 Localization Effects . . . . .	39
2.2.6 White LEDs . . . . .	40
2.3 Organic Semiconductors . . . . .	41
2.3.1 Hybrid White LEDs . . . . .	42
References . . . . .	45

<b>3</b>	<b>Experimental Techniques</b>	<b>50</b>
3.1	Optical Characterization . . . . .	50
3.1.1	Photoluminescence . . . . .	50
3.1.2	Photoluminescence Excitation . . . . .	51
3.1.3	Time Resolved Photoluminescence . . . . .	52
3.1.4	Confocal Microscopy . . . . .	57
3.1.5	X-ray Diffraction . . . . .	57
3.2	Device Fabrication . . . . .	58
3.2.1	Thin film Deposition Techniques . . . . .	58
3.2.2	Dry Etching Techniques . . . . .	59
3.2.3	Organic Materials Deposition Techniques . . . . .	59
	References . . . . .	59
<b>4</b>	<b>Self Assembled InGaN/GaN MQW Nanorod Arrays</b>	<b>63</b>
4.1	InGaN/GaN Multiple Quantum Well Structures . . . . .	64
4.2	Nanorod Fabrication . . . . .	72
4.3	Characterization of InGaN/GaN MQW Nanorods . . . . .	74
4.3.1	InGaN/GaN MQW Nanorod Carrier Recombination Dynamics . . . . .	77
4.4	Summary . . . . .	83
	References . . . . .	83
<b>5</b>	<b>Non-Radiative Energy Transfer from InGaN MQW Nanorod Arrays to a Light Emitting Polymer</b>	<b>89</b>
5.1	Hybrid Organic / Inorganic Structures for LEDs using Non-radiative Energy Transfer . . . . .	89
5.2	Light Emitting Polymer Deposition and Characterization . . . . .	94
5.3	Hybrid Structures . . . . .	98
5.3.1	Hybrid Organic/Inorganic Nanorod White Emitting Structures Using FRET . . . . .	98
5.4	Summary . . . . .	104
	References . . . . .	105
<b>6</b>	<b>Exciton Localization and its Effect on Non-radiative Energy Transfer in III-Nitride based Organic/Inorganic Hybrids</b>	<b>109</b>
6.1	Localization Effects in III-Nitride Materials . . . . .	109
6.2	Energy Transfer Dependence on Localization . . . . .	110
6.3	Temperature Dependent Optical Properties of InGaN/GaN MQW Nanorods	112
6.4	Temperature Dependent Non-radiative Energy Transfer due to Exciton Localization . . . . .	114
6.5	Summary . . . . .	119
	References . . . . .	119
<b>7</b>	<b>Surface Passivation of InGaN/GaN MQW Nanorods and the Effect on Non-radiative Energy Transfer</b>	<b>121</b>
7.1	Background . . . . .	121
7.2	Sample Preparation and Optical Characterization . . . . .	122
7.3	Enhanced FRET due to Passivation of Nanorods . . . . .	125
7.4	Dependence of Energy Transfer on Surface State Passivation . . . . .	128
7.5	Summary . . . . .	130
	References . . . . .	130



<b>8</b>	<b>Conclusions and Further Work</b>	<b>133</b>
8.1	Summary of Results . . . . .	133
8.2	Further Work . . . . .	135



---

## Abstract

---

In this work, methods of increasing the efficiency of InGaN/GaN based quantum well structures have been investigated based on the use of self assembly nanostructuring techniques and the fabrication of hybrid organic/inorganic white light emitting structures. The aim of investigating efficiency improvements in these structures is to enable the development of higher efficiency white LEDs for the purposes of general illumination.

InGaN/GaN multiple quantum well (MQW) nanorod arrays were fabricated by a top-down, post growth technique, and the exciton dynamics have been investigated by a number of advanced optical facilities. The internal quantum efficiency (IQE) has been significantly improved as a result of being fabricated nanostructure, leading to significant change in recombination lifetime of carrier and enhancing the lateral confinement of the exciton in the in-plane quantum well.

Blue emitting InGaN/GaN MQW nanorods were used to fabricate hybrid organic / inorganic white light emitting structures, by spin coating light emitting polymer films on the top of the nanorods. This allows the use of non-radiative, near-field coupling of quantum well and light emitting polymer excitons. The high efficiency non-radiative coupling was investigated by examining the change in exciton dynamics in the MQW. The non-radiative energy transfer process was found to have a fast rate of  $0.76\text{ns}^{-1}$ , competing with the non-radiative recombination pathways of the MQW.

The non-radiative energy transfer efficiency was found to increase by a factor of 6.7 with increasing temperature from 7K to 300K as a result of the thermal de-localization of MQW excitons. The increase in non-radiative energy transfer efficiency is caused by both the change in exciton dimensionality and the increase in excitonic diffusion length.

The effect of surface states on the optical properties of the InGaN/GaN MQW nanorod arrays was examined with the use of silicon nitride films to passivate surface states. An increase in MQW IQE and recombination lifetime was observed for the passivated nanorods. The passivation of nanorods was found to increase the non-radiative energy transfer coupling efficiency in the hybrid organic / inorganic white light emitting structures. This effect is attributed to the reduction in surface depletion region due to the passivation of surface states leading to an increased exciton density in the outer region of the nanorods allowing stronger non-radiative energy transfer coupling.



---

## Acknowledgements

---

Many people have assisted me in the process of this project greatly and I wish to offer my gratitude for all of their help and assistance. Firstly, I am very grateful to my supervisor Professor Tao Wang, for supporting me through my Ph.D. studies, giving me the opportunity to develop the skills and knowledge and opening the door for me to the interesting and exciting area of III-nitride opto-electronics.

I wish to thank Dr. Jie Bai for all of her training and a huge amount fabrication assistance. Dr. Qi Wang, for his training in optical characterization techniques, and lengthy discussions on all things nitrides. Dr. Bin Liu, for his help and advice, and the many hours spent in the optics lab.

Professor Wang's III-nitrides group has grown significantly since I started my Ph.D. studies, as I have learned much from working with all the members, I thank the growth team, Yipin Gong, Kun Xing, Yu Xiang, Benbo Xu for their work in providing me with the high quality samples I needed and for their help in all matters growth. Paul Renwick, Jon Benton, Modestos Athanasiou, Hao Tang, my thanks for useful discussions and all the hours spent at the white board testing out ideas.

I have not only relied on the extensive technical support of Paul Haines, Jon Milner and Dave Morris to keep everything working but have also gained a lot of practical skills through their patient help. I also wish to thank the many members of the EEE workshop for their work in producing all of the components I have required and also helping me improve my technical drawing skills from my original 'sketches'.

I am grateful for Neil Lowrie and all those involved in the E-futures DTC for my funding, support and the E-futures experience.

Finally I am indebted to my family for their constant support. I owe so much to my parents, from fostering scientific curiosity in me from a young age and for supporting me all the way. I am grateful for my sister who has always been an example to me, even as the younger sibling.

I couldn't have made it through my Ph.D. at all without the love, support and motivation of my wife, thank you. 1.



---

## List Of Publications

---

### Journal Publications

**R. Smith, B. Liu, J. Bai, T. Wang.** “Hybrid III-nitride/organic semiconductor nanostructures with high efficiency non-radiative energy transfer for white light emitters”*Nano Lett.*, 13 (7), pp 3042-3047, (2013)

**M. Athanasiou, T. K. Kim, B. Liu, R. Smith and T. Wang.** “Fabrication of two-dimensional InGaN/GaN photonic crystal structure using a modified nanosphere lithography technique”*Appl. Phys. Lett.*, 102, 191108, (2013)

**B. Liu, R. Smith, J. Bai, Y. P. Gong, T. Wang.** “Exciton recombination dynamics and emission enhancement mechanism of violet, blue, and green emission InGaN/GaN quantum well nanorods”*Appl. Phys. Lett.*, 103, 101108, (2013)

**P. Renwick, H. Tang, Q. Wang, R. Smith, and T. Wang** “Enhanced internal quantum efficiency of an InGaN/GaN quantum well as a function of silver thickness due to surface plasmon coupling” *Phys. Stat. Sol. C, Vol.8, Issue 7-8, Page 2176, July 2011*

**R. Smith, B. Liu, J. Bai, T. Wang.** “Significant increase in non-radiative energy transfer efficiency in hybrid organic/inorganic white light emitters by passivation of surface states in InGaN/GaN MQW nanorods”*In preparation(2013)*

**R. Smith, B. Liu, J. Bai, T. Wang.** “Characterization of the effects of exciton localization on Non-radiative energy transfer between InGaN MQW nanorods and a light emitting polymer in novel hybrid organic inorganic devices”*In preparation(2013)*

### Conference Oral Presentations

**R. Smith, B. Liu, J. Bai and T. Wang** “High Efficiency Non-Radiative Energy Transfer in Novel White Light Emitting Hybrid Organic/Inorganic Structures Using InGaN/GaN Nanorod Arrays”*International Conference on Nitride Semiconductors, Washington D.C. Aug. 2013*

**R. Smith, B. Liu, J. Bai, K. Xing, Y.P. Gong and T. Wang** “An optical investigation of high quality non-polar (a-plane) and semi-polar (11-22) InGaN/GaN MQWs grown on sapphire using nanorod overgrowth technique”*UK Nitrides Consortium Sheffield July. 2013*

**R. Smith, B. Liu, J. Bai and T. Wang** “An Investigation of Non-radiative Energy Transfer Between InGaN/GaN MQWs and a Light Emitting Polymer in Novel Hybrid Nanorod Array Structures”*UK Nitrides Consortium Cardiff Jan. 2013*

**R. Smith, J. Bai, Q. Wang and T. Wang** “Enhanced non-radiative energy transfer coupling of GaN/InGaN MQW nanorods to a light-emitting polymer”*UK Nitrides Consortium Bath Jan. 2012*



### **1.1 Introduction**

This chapter seeks to identify the context of this thesis and introduce the motivation and potential benefits of this area of research. The significant benefits and potential of III-nitride based semiconductor optoelectronics will be introduced before looking at the challenges that face this research area. The challenges facing III-nitrides will highlight some of the interesting and important research opportunities. The scientific and technical detail will be included in Chapter 2.

#### **1.1.1 The Energy Crisis**

The Intergovernmental Panel on Climate Change (IPCC), the UN official independent scientific body set up to examine earth's climate, now states that it is a "very high confidence" that anthropogenic carbon emissions are the cause of the climate change seen since the start of the industrial revolution [1]. As such, reductions in carbon emissions are required to abate the potential problems associated with significant global climate change. Electrical power generation is still dominated by carbon intensive sources such as coal and natural gas, efforts are being made to increase the proportion of electrical power generated by low-carbon, renewable sources such as wind turbines, solar cells, and solar thermal power plants. The penetration of low carbon power generation technologies still remains low and as such energy demand reduction policies are becoming increasingly prominent and necessary. Alongside the need to reduce carbon emissions by energy consumption reduction, there is also a further motivation for energy demand reduction measures, energy security and resource depletion. Most electrical energy is still produced by means of fossil fuels which are inherently finite resources, as demand for these resources increases and their availability decreases, the prices of electrical energy increase

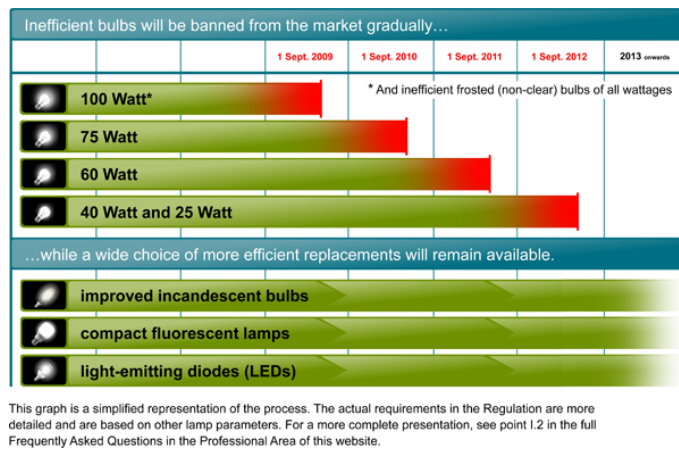


Figure 1.1: The phase out of inefficient incandescent lighting sources brought into effect by European legislation [6]

and supply becomes vulnerable to lack of resources.

In response to the looming energy crisis, many bodies globally are working on initiatives to reduce energy usage through demand reduction, for example in the UK the Department of Energy and Climate Change (DECC) have been conducting consultations in order to determine future policy steps to reduce energy demand [2]. Globally, lighting is a major consumer of energy, with 1.9Gt of CO<sub>2</sub> emitted per year due to lighting applications [3]. Any improvement in the efficiency of lighting technologies can therefore have a significant impact on energy usage and CO<sub>2</sub> emissions.

## 1.1.2 Lighting Technologies

Several different lighting technologies are regularly in use today, from high performance electrical lighting to gas and kerosene lamps which are still in use in the developing world. The incandescent light bulb has changed little since it's development by Edison, with luminous efficacies still now only approaching 16 lm/W [4]. Incandescent lighting works on the principal of increasing the temperature of a filament to generate thermionic emission, this is the major efficiency limiting factor as most energy is emitted as heat. The development of fluorescent lamps allowed higher luminous efficacies several times higher than that of incandescents. Fluorescent lamps work on the principle of gas discharge, where a gas is electrically excited and atomic transitions in the gas release photons, phosphor materials are used to down-convert the emitted light into the visible spectrum. Fluorescent lamps have enjoyed much success due to their reasonably high luminous efficacies, taking a 53% market share in 2012 (including compact fluorescent (CFL)) [5]. Although compact fluorescent lamps have made it possible to use fluorescent lamps in more compact designs, they still have relatively large footprints and are not scalable over a wide range of sizes. As fluorescent lamps are based on mercury vapour discharge, they rely on the use of toxic mercury which, alongside inefficient incandescent lamps, faces a gradual phase out by European legislation[6], as shown in Figure 1.1.

Image not available in electronic version.  
Please find original at citation in the text.

Figure 1.2: The luminous efficacies of various lighting technologies plotted for the year of their development by Narukawa et al. [4]

Light Emitting Diodes (LEDs) are ubiquitous in the modern world, from humble beginnings as simple low luminous flux indicators. LEDs now are used for numerous uses including those that require high luminous fluxes such as back-lighting for liquid crystal displays (LCDs), projectors, car headlamps and general illumination. During the last two decades nitride LEDs have been developed at a significant rate to be able to compete with existing lighting technologies as shown in Figure 1.2. In order to be a competitive technology, LED performance has to be significantly better than other technologies owing to the inherently more expensive techniques required such as epitaxial growth and packaging.

## 1.2 The History of Nitride Semiconductors

The first visible light emitting LED was demonstrated in 1962 using a GaAsP heterostructure [7]. Since then the III-V semiconductor materials have been used to create LEDs with a variety of emission wavelengths. The limitation of the GaAsP system is that the bandstructure of the material becomes indirect when the phosphorous mole fraction increases to a level above  $GaAs_{1-x}P_x$  for  $x = 0.49$  [8]. It wasn't until the realisation of good quality direct, wide-bandgap semiconductors based on the III-nitrides that the full visible spectrum, and therefore white LEDs became a practical possibility. Before the arrival of GaN based blue LEDs the only way to create blue emitting LEDs was with indirect SiC resulting in extremely low efficiencies with EQE reaching a maximum of 0.03% at an emission wavelength of 470nm [9]. The utility of the III-nitride semiconductors comes from the wide range of bandgaps achievable with ternary and quaternary alloys of Al/In/Ga-N reaching from the UV with AlN at 6.2eV and InN at 0.7eV as seen in Figure 1.3. Until significant breakthroughs in the late 1980's and early 1990's, work was limited

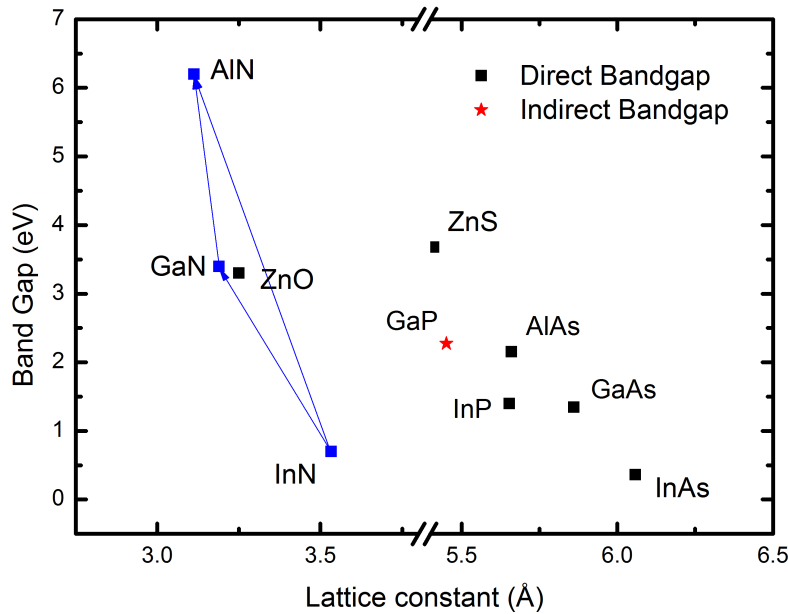


Figure 1.3: The bandgap energies of various semiconductors plotted against their lattice constants

to examining the growth, structural and material properties of gallium nitride thin films, limited by the low crystal quality and inability to grow p-type GaN.

GaN and the related III-nitrides had been a subject of research on a relatively minor scale over the 20th century since the first synthesis of a group III nitride material, AlN in 1907 [10]. In 1969 Maruska et al. succeeded in growing single crystalline GaN using the hydride vapour phase epitaxy (HVPE) crystal growth technique [11] (growth techniques will be covered in more detail in Chapter 2). This breakthrough allowed the direct band structure of GaN to be experimentally measured by optical absorption, and the wide band gap measured as 3.39eV. This practical demonstration of the potential of III-nitride materials as direct wide bandgap semiconductors was followed by attempts to apply these new materials to optoelectronic devices. An electroluminescent GaN metal/insulator/semiconductor LED grown by HVPE was reported in 1971 by Pankove et al. [12]. Although an important development, the performance of this metal/insulating/n-type structured device was significantly hindered by the lack of p-type GaN. In the same year, single crystal GaN was also grown by Metal Organic Chemical Vapour Deposition (MOCVD) [13], this constituted a significant step in III-nitride development due to the utility of MOCVD as a growth technique capable of mono-layer deposition, which is a prerequisite for the growth of the types of device structures required for optoelectronics such as quantum wells and heterostructures.

Following these achievements, the continuation of III-nitride research was carried out mainly by groups in Japan and this is where the next significant breakthroughs were made. Throughout the 1980's the focus was on improvements in material synthesis, improving

the crystal quality of epitaxially grown III-nitride materials. One of the significant barriers was to achieve high quality smooth films on the foreign substrates that were available. In 1986, Amano and Akasaki developed the well-known two-step approach using MOCVD to generate high quality films, namely, a thin AlN nucleation layer is initially deposited at a low temperature on a sapphire substrate (at 600°C), before the growth of high temperature GaN layer at 1030°C [14, 15]. This two step technique has the effect of forming polycrystalline AlN on the sapphire surface which acts as a high density of nucleation centres for the high temperature GaN growth. The GaN growth then laterally coalesces essentially blocking propagation of defects from the low crystal quality AlN nucleation layer. This technique marked a significant milestone in the development of epitaxial growth of GaN with the high crystal qualities required for the fabrication of optoelectronic devices and will be covered in detail in Chapter 2. Nakamura demonstrated that this two step process can also be used to produce high quality GaN films using a low temperature GaN nucleation layer [16].

The major breakthrough allowing the development of high efficiency nitride semiconductor devices was the ability to grow and activate p-type gallium nitride with reasonable conductivity. Despite the ability to incorporate Mg into GaN films with concentrations high enough for doping, films were still found to be strongly resistive, Amano et al. used Low Energy Electron Beam Irradiation (LEEBI) to treat the GaN:Mg layers activating the p-type properties [17]. After exposure to the LEEBI, the resistivity dropped to  $35\Omega\text{ cm}$  from  $> 10^8\Omega\text{ cm}$  for the untreated samples. The activation step was found to result from the presence of hydrogen in the GaN:Mg, with the formation of Mg:H complexes. The activation step removed the hydrogen allowing the magnesium to act as a p-type dopant. Shuji Nakamura demonstrated that the p-type activation could be achieved with a post growth thermal annealing of the GaN:Mg film [18]. This development is of significant importance as it allowed the growth of GaN p-n junctions using MOCVD and commercially applicable technologies.

Following the work allowing the MOCVD growth of high quality GaN films on sapphire substrates and the development of repeatable p-doping techniques, development then focussed on addressing the potential of III-nitrides as short wavelength LEDs and laser diodes (LDs). In 1993 Nakamura demonstrated visible light emission using InGaN, after growing InGaN/InGaN MQW superlattices [19]. In the following year, Nakamura built on this development to produce electroluminescence through the use of InGaN/AlGaIn double-heterostructures to produce blue emitting LEDs [20]. With the demonstration of these improvements and the long anticipated potential of III-nitride based optoelectronics beginning to be realised, interest in III-nitride research expanded hugely as can be seen from Figure 1.4 by Akasaki [21] showing the number of GaN related research papers increasing significantly through the early 1990s.

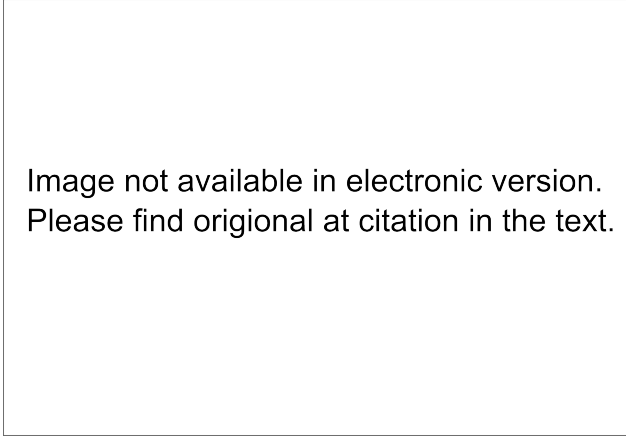


Image not available in electronic version.  
Please find original at citation in the text.

Figure 1.4: The number of papers published with keywords GaN as a function of publication year from Akasaki and Amano [21]

### 1.3 Current Challenges and Limitations

Despite the successes that III-nitride semiconductors have enjoyed in the last two decades, significant challenges still prevent III-nitride based white LEDs reaching their theoretical potential. White light sources are predicted to reach maximal spectral luminous efficacies of between 250 – 350lm/W depending on the quality of the colour (colour rendering index) [22]. In order to achieve these spectral luminous efficacies, high device efficiencies are required such as the Internal Quantum Efficiency (IQE), External Quantum Efficiency (EQE) and wall-plug efficiency. The quantum efficiencies describe the conversion of the injected excited carriers to photons, in the case of IQE, only the fraction of generated photons compared to excited carriers is considered, for EQE the extraction of photons out of the device is also considered. The wall-plug efficiency describes the total power conversion efficiency of the device, including the IQE, light extraction efficiency (LEE) and electrical losses (such as parasitic resistances or current leakage).

#### Substrates

Unlike silicon, germanium and other III-V semiconductors such as GaAs, GaN single crystal boules cannot be grown by the standard equilibrium growth techniques such as the Czochralski method [23] due to the high bonding energy of III-nitride materials [24–26]. As a result, bulk GaN wafers are still not widely available, and are extremely expensive. The majority of III-nitrides grown for commercial purposes are hetero-epitaxially grown on sapphire, silicon carbide or silicon substrates. Hetero-epitaxy poses significant challenges to achieving high quality single crystal structures required for high performance opto-electronics, such as lattice mismatch and differences in thermal expansion coefficients [27]. The most common substrate for III-nitrides is sapphire ( $\alpha - Al_2O_3$ ). Due to the significant lattice mismatch between GaN and sapphire, GaN growth on sapphire proceeds with a rotation around the c-axis of  $60^\circ$  [28]. In order to reduce the lattice mismatch bulk GaN substrates are an area of research, using techniques such as HVPE [29]

to grow thick GaN layers on foreign substrates that can then be separated to become free standing GaN substrates, and the high pressure, high temperature ammonothermal growth using supercritical ammonia to dissolve and re-crystallize GaN powder [24–26]. Both of these techniques however are extremely expensive and face significant challenges in reducing the cost to be competitive with sapphire. Another approach taken has been the use of silicon substrates for GaN growth. The lattice constants and thermal expansion coefficients of GaN and silicon are significantly different. Leading to extensive problems in reducing defect density of the hetero-epitaxial GaN films. The benefit of growth on silicon substrates is that the cost of silicon is lower than sapphire. Larger substrate diameters are available and silicon semiconductor fabrication facilities can be adapted for LED fabrication.

### **Quantum Confined Stark Effect**

As will be covered in more depth in Chapter 2, III-nitride semiconductors are predominantly a wurtzite crystal structure and are polar materials. Due to the symmetry of the wurtzite crystal lattice GaN layers are polar along the c-direction (0001), as such, when subjected to strain, the III-nitride semiconductors exhibit a piezo-electric field. As there is a lattice mismatch between GaN, InN and AlN, growth of hetero-structures of different III-nitrides and their alloys introduces strain to the lattice and leads to piezoelectric fields. As visible light emitting diodes are based on InGa<sub>x</sub>N multiple quantum wells with GaN barriers, a piezoelectric field is generated across the quantum wells. Analogous to the stark effect in atomic spectra where an external electric field shifts the nucleus and electrons in opposite directions this piezoelectric field separates electron and hole wavefunctions in the quantum well active region and reduces the radiative recombination lifetime, and hence efficiency. GaN and InN have similar spontaneous polarization coefficients, as such in InGa<sub>x</sub>N/GaN structures, the piezoelectric fields dominate over spontaneous polarization fields [30]. The characteristic effects of QCSE on carriers in a quantum well are discussed in more detail in Chapter 2, including a red-shift in emission wavelength and an increase in the radiative recombination lifetime due to the reduction in electron-hole wavefunction overlap. In order to address the visible wavelength region, alloys of InGa<sub>x</sub>N are used to achieve the corresponding band gap energies. Due to the increasing lattice mismatch between GaN and InGa<sub>x</sub>N with increasing In composition, longer emission wavelengths face significantly stronger QCSE, reducing the efficiency of longer emission wavelength III-nitride based devices.

Attempts to abate QCSE in III-nitride devices are either focused on reducing strain in the InGa<sub>x</sub>N/GaN structures or growing structures in other orientations to reduce the component of piezoelectric field in the confinement direction of InGa<sub>x</sub>N quantum wells. Strain relaxation can be induced by different methods, either the use of strain relaxing buffer layers such as superlattices [31] to change the effective lattice constant of the material, or the use of nanostructures [32–34] allowing strain relaxation in lattice mismatched films.

The majority of III-nitride opto-electronics are grown on c-plane sapphire substrates where the polarization direction is in the (0001) growth direction, if substrates of another orientations are used, with a reduced or zero component of the c-projection in the growth direction, the piezoelectric field across the quantum wells can be reduced or removed. This can significantly improve the performance of InGaN/GaN quantum well structures due to the significant reduction in QCSE [35–38].

The growth or fabrication of nanostructures such as nanorods or nanoholes through epitaxial planar surfaces of InGaN/GaN quantum well structures is an increasingly popular method of generating strain relaxation in InGaN quantum wells. Numerous reports using nanorods [33, 34, 39] and other nanostructures [32] have investigated nanostructuring related strain relaxation. Through the breaking of the crystal lattice in the plane of the quantum wells, the lattice can relax to a more energetically favourable relaxed state, and by the Poisson effect, a change in the effective lattice constant in the plane of the quantum well will correlate to a change in the vertical effective lattice constant. Due to the fact that nanostructures can be fabricated after standard growth using cost effective self assembly techniques [33, 40], this approach to reducing QCSE and therefore increasing IQE is currently an active area of research with significant potential performance benefits.

## **Efficiency Droop**

In order to achieve the highest light output from an LED at the lowest cost, ideally, LEDs would be operated at high efficiencies under high injection current regimes in order to maximize the light output per device. Unfortunately III-nitride based LEDs exhibit behaviour described as efficiency droop, where the highest device efficiency occurs at low injection current densities, and the efficiency drops with increased injection current. This effect is shown in Figure 1.5 by Cho et al. [41], where efficiency droop can be seen in violet, blue and green emitting InGaN LEDs. As the effect of efficiency droop is so potentially detrimental to the performance of the high brightness LEDs required for general illumination purposes, droop remains a significant focus of research in III-nitrides. The cause(s) of efficiency droop are still a matter of much debate in the III-nitride community with many different proposed causes and no overriding consensus of a single cause. The main theories still under consideration are indirect Auger recombination [42], current leakage [41] and Density Affected Defect Recombination (DADR) [43, 44].

Auger related processes were proposed as the cause of the efficiency droop phenomenon in 2007 by Shen et al. of Phillips Lumileds company [45]. Auger recombination requires three carriers, either an electron and two holes or two electrons and one hole. As the electron and hole recombine, the energy is transferred to the third carrier, instead of being released from the crystal as a photon. The Auger recombination process will be discussed in detail in Chapter 2. The initial report used photoluminescence to investigate the Auger recombination in InGaN MQWs using recombination rate equations to determine the Auger coefficient. In 2013 a report was published by Iveland et al. with direct



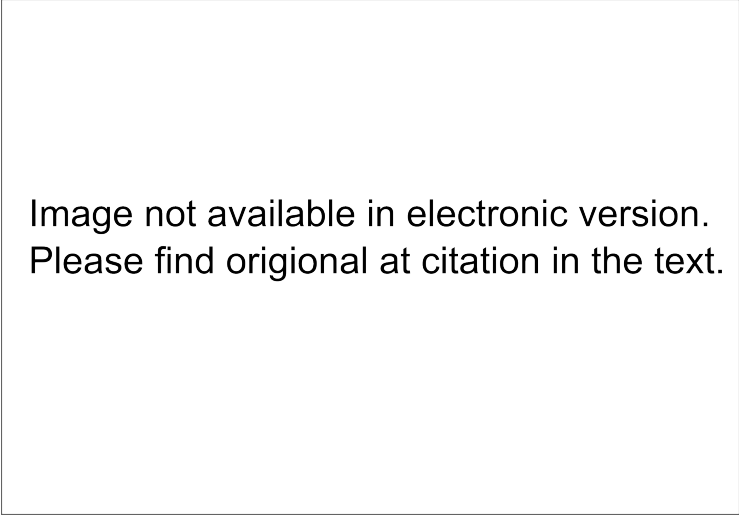


Image not available in electronic version.  
Please find original at citation in the text.

Figure 1.5: Efficiency droop of InGaN MQW based LEDs of various wavelengths by Cho et al. [41]

observation of high energy electrons associated with indirect Auger recombination in an InGaN LED device under electrical injection [42]. In this work the device was cleaved in a vacuum chamber and the cleaved faced coated with caesium. The caeseated surface is able to electroluminesce when electrons with high enough energy to excite caesium atomic transitions collide with the caesium coated surface. Using this technique it was found that under high injection current conditions, photo-emission from a higher energy electron is observed in the caesium electroluminescence, which is attributed to the Auger process.

Regardless of the underlying fundamental physical cause of efficiency droop, it is a phenomenon that exists at high carrier densities, therefore currently, the most effective techniques to combat droop are those those that reduce carrier density in a device. This can be achieved in a number of different ways, such as increasing the active volume of a device, and therefore reducing effective carrier density. This either requires the use of large area devices (increasing cost per device) or the use of thicker active regions, which is typically not possible in polar structures due to the limitations of the quantum confined stark effect. Another approach to reduce carrier density is to reduce the radiative recombination lifetime of carriers in the active region in order to reduce the overall carrier density. Reducing recombination lifetimes can be achieved by increasing electron/hole wavefunction overlap by reducing the piezoelectric field across quantum wells by either strain relaxation or growth of quantum wells in non-polar orientations.

## **White LEDs**

There are a range of issues effecting the performance of white LEDs, from colour quality issues to colour stability [46]. Furthermore, there are significant intellectual property rights issues surrounding phosphors [47]. Early white LEDs had particularly low CRI values with blue heavy spectra. One of the most significant barriers to the widespread

Image not available in electronic version.  
Please find original at citation in the text.

Figure 1.6: An image from Krames et al. [50] showing the quantum efficiencies of LEDs of different materials systems at various wavelengths. The so called "green gap" between high efficiency blue and red emitting LEDs is clear. With the human eye responsivity plot centred in the green/yellow spectral region

adoption of LEDs for general illumination is the significantly higher price compared to other lighting technologies. Increasing production capacity and competition are driving down LED prices yet some obstacles remain for the newer LED manufacturers particularly throughout China. One of these issues is the control over phosphor intellectual property by the well established LED manufactures and in particular Nichia due to their history as a phosphor company. The phosphor materials used in white LEDs currently are based on the use of rare earth metals such as yttrium, cerium and europium. Due to their scarce nature, rare earth metals are extracted at a small number of sites around the world, as such the market for rare earth metals (and therefore white LED phosphors) is strictly controlled [48, 49]. This situation reduces competition and can drive up prices of phosphor materials, affecting the white LED market.

The problem facing mixed, discrete colour LEDs (e.g. red, green, blue or red, yellow, green, blue) is the lack of high efficiency LEDs emitting in the spectral region between blue and red, termed the green gap. Due to the large lattice mismatch between InN and GaN, the high indium composition InGa<sub>N</sub> alloys required to achieve emission at wavelengths longer than the blue spectral region lead to very significant QCSE that limits performance. The green gap can be seen in Figure 1.6. Red emitting LEDs with good EQE values are achievable using the AlInGaP materials system, however at wavelengths below 560nm the bandgap becomes indirect and high efficiencies are no longer achievable [50]. Due to these issues, along with the inherently higher costs associated with growing fabricating and packaging three or more individual LEDs, mixed colour LEDs are not currently competitive in performance or price with down-conversion LEDs.

Due to the dual issues of phosphor performance and the phosphor market, alternative routes to generating white light using LEDs are an interesting and important prospect. The potential solutions are either to find alternative down-conversion materials or to use entirely LED based solutions, for example mixtures of blue, green and red emitting LEDs.

Any material that absorbs shorter wavelength visible light and re-emits at longer visible wavelengths can potentially be used as a phosphor material. In practical terms, in-order to produce high luminous efficacy white LEDs, the conversion efficiency of the material must be high, to minimize conversion losses, and the emission wavelengths must be in the correct region to properly replicate a white emission spectrum.

Light emitting organic molecules and polymers can display extremely high photoluminescence quantum yields (photons emitted / photons absorbed), with modern organic light emitting materials having photoluminescence quantum yields of 85% [51]. A wide variety of organic materials have been synthesised during the development of organic LEDs and some specifically for hybrid organic/inorganic LED applications [52]. Guha et al. demonstrated the potential of hybrid organic/inorganic LEDs in 1997, using a commercial Nichia InGaN based blue LED and an organic fluorescent down conversion layer constituting of organic materials of the coumarin class [53]. In this case, the organic down-conversion material was acting directly as a phosphor replacement. In the same year a separate report also demonstrated hybrid organic/inorganic devices emitting white light using poly-phenylenevinylene (PPV) derivatives [54].

Other routes have also been used as phosphor replacement down-conversion, other than fluorescent organic materials. Another area of strong research interest is the use of colloidal quantum dots. Typically produced from II-VI, and less commonly III-V semiconductor materials, colloidal quantum dots or nano crystals have sizes on the order of tens of nanometres creating three dimensionally confined carriers and as such typically have spectrally narrow emission peaks. Lee et al. used a mixture of colloidal quantum dots of different emission wavelengths suspended in a polymer matrix as a colour conversion medium to generate white light under LED photo-excitation [55].

These approaches allow some of the issues with traditional phosphor materials to be addressed. Traditional phosphors still dominate commercially available white LEDs due to the immaturity of these promising, newer technologies. More recent research has focused on novel uses of down-conversion materials allowing the use of high efficiency non-radiative coupling of down-conversion material to III-nitride LED. This will be covered in detail in Chapter 2.

## References

<sup>1</sup>IPCC, *Summary for Policymakers. In: Climate Change 2007: The Physical Science Basis. Contribution of Working Group I to the Fourth Assessment Report of the Intergovernmental Panel on Climate Change*, technical report (Cambridge University Press, Cambridge, United Kingdom and New York, NY, USA, 2007).

<sup>2</sup>DECC, *Electricity Demand Reduction: Consultation on options to encourage permanent reductions in electricity use*, technical report November (Department of Energy and Climate Change, 2012).

- <sup>3</sup>M. Levine, D. Urge-Vorsatz, K. Blok, L. Geng, D. Harvey, S. Lang, G. Levermore, S. MongameliMehlwana, A. Mirasgedis, Novikova, J. Rilling, and H. Yoshino, *Residential and commercial buildings. In Climate Change 2007: Mitigation. Contribution of Working Group III to the Fourth Assessment Report of the Intergovernmental Panel on Climate Change*, technical report (Cambridge University Press, Cambridge, United Kingdom and New York, NY, USA. 1, 2007), pages 402–403.
- <sup>4</sup>Y. Narukawa, M. Ichikawa, D. Sanga, M. Sano, and T. Mukai, “White light emitting diodes with super-high luminous efficacy”, *Journal of physics d: applied physics* **43**, 354002 (2010).
- <sup>5</sup>I. McKinsey & Company, *Lighting the way: Perspectives on the global lighting market*, technical report (McKinsey & Company, Inc., 2012).
- <sup>6</sup>EuropeanCommission, *EU Energy Saving Light Bulbs*.
- <sup>7</sup>N. Holonyak and S. F. Bevacqua, “COHERENT (VISIBLE) LIGHT EMISSION FROM GaAsP JUNCTIONS”, *Applied physics letters* **1**, 82 (1962).
- <sup>8</sup>M. G. Craford, R. W. Shaw, A. H. Herzog, and W. O. Groves, “Radiative recombination mechanisms in GaAsP diodes with and without nitrogen doping”, *Journal of applied physics* **43**, 4075 (1972).
- <sup>9</sup>C. A. Yuan, C. N. Han, H. M. Liu, and W. D. van Driel, “SolidState Lighting Technology in a Nutshell”, in *Solid state lighting reliability: components to systems*, edited by W. D. van Driel and X. J. Fan (Springer, 2012), pages 19–21.
- <sup>10</sup>F. A. Ponce and D. P. Bour, “Nitride-based semiconductors for blue and green light-emitting devices”, *Nature* **386**, 351–359 (1997).
- <sup>11</sup>H. P. Maruska and J. J. Tietjen, “THE PREPARATION AND PROPERTIES OF VAPOR-DEPOSITED SINGLE-CRYSTAL-LINE GaN”, *Applied physics letters* **15**, 327 (1969).
- <sup>12</sup>J. Pankove, E. Miller, and J. Berkeyheiser, “GaN electroluminescent diodes”, in 1971 international electron devices meeting (1971), pages 78–78.
- <sup>13</sup>H. M. Manasevit, F. M. Erdmann, and W. I. Simpson, “The Use of Metalorganics in the Preparation of Semiconductor Materials”, *Journal of the electrochemical society* **118**, 1864 (1971).
- <sup>14</sup>K. Hiramatsu, S. Itoh, H. Amano, I. Akasaki, N. Kuwano, T. Shiraishi, and K. Oki, “Growth mechanism of GaN grown on sapphire with AlN buffer layer by MOVPE”, *Journal of crystal growth* **115**, 628–633 (1991).
- <sup>15</sup>H. Amano, N. Sawaki, I. Akasaki, and Y. Toyoda, “Metalorganic vapor phase epitaxial growth of a high quality GaN film using an AlN buffer layer”, *Applied physics letters* **48**, 353 (1986).
- <sup>16</sup>S. Nakamura, “GaN Growth Using GaN Buffer Layer”, *Japanese journal of applied physics* **30**, L1705–L1707 (1991).

- <sup>17</sup>H. Amano, M. Kito, K. Hiramatsu, and I. Akasaki, “P-Type Conduction in Mg-Doped GaN Treated with Low-Energy Electron Beam Irradiation (LEEBI)”, *Japanese journal of applied physics* **28**, L2112–L2114 (1989).
- <sup>18</sup>S. Nakamura, T. Mukai, M. Senoh, and N. Iwasa, “Thermal Annealing Effects on P-Type Mg-Doped GaN Films”, *Japanese journal of applied physics* **31**, L139–L142 (1992).
- <sup>19</sup>S. Nakamura, T. Mukai, M. Senoh, S.-i. Nagahama, and N. Iwasa, “In<sub>x</sub>Ga(1-x)N/In<sub>y</sub>Ga(1-y)N superlattices grown on GaN films”, *Journal of applied physics* **74**, 3911 (1993).
- <sup>20</sup>S. Nakamura, T. Mukai, and M. Senoh, “Candela-class high-brightness InGaN/AlGaIn double-heterostructure blue-light-emitting diodes”, *Applied physics letters* **64**, 1687 (1994).
- <sup>21</sup>I. Akasaki and H. Amano, “Breakthroughs in Improving Crystal Quality of GaN and Invention of the p-n Junction Blue Light Emitting Diode”, *Japanese journal of applied physics* **45**, 9001–9010 (2006).
- <sup>22</sup>T. W. Murphy, “Maximum spectral luminous efficacy of white light”, *Journal of applied physics* **111**, 104909 (2012).
- <sup>23</sup>P. Y. Yu and M. Cardona, “Introduction”, in *Fundamentals of semiconductors*, Graduate Texts in Physics (Springer Berlin Heidelberg, Berlin, Heidelberg, 2010), pages 1–18.
- <sup>24</sup>Q. Bao, M. Saito, K. Hazu, K. Furusawa, Y. Kagamitani, R. Kayano, D. Tomida, K. Qiao, T. Ishiguro, C. Yokoyama, and S. F. Chichibu, “Ammonothermal Crystal Growth of GaN Using an NH<sub>4</sub>F Mineralizer”, *Crystal growth & design* **13**, 4158–4161 (2013).
- <sup>25</sup>R. Kucharski, M. Zajac, R. Doradzinski, M. Rudzinski, R. Kudrawiec, and R. Dwilinski, “Non-polar and semi-polar ammonothermal GaN substrates”, *Semiconductor science and technology* **27**, 024007 (2012).
- <sup>26</sup>R. Dwilinski, R. Doradzinski, J. Garczynski, L. Sierzputowski, R. Kucharski, M. Zajac, M. Rudzinski, R. Kudrawiec, W. Strupinski, and J. Misiewicz, “Ammonothermal GaN substrates: Growth accomplishments and applications”, *Physica status solidi (a)* **208**, 1489–1493 (2011).
- <sup>27</sup>T. Hanada, “Basic Properties of ZnO, GaN, and Related Materials”, in *Oxide and nitride semiconductors se - I*, Vol. 12, edited by T. Yao and S.-K. Hong, *Advances in Materials Research* (Springer Berlin Heidelberg, 2009), pages 1–19.
- <sup>28</sup>B. Gil, “Stress Effects on Optical Properties”, in *Gallium nitride ii* (Academic Press, 1999), pages 209–271.
- <sup>29</sup>T. Paskova, D. a. Hanser, and K. R. Evans, “GaN Substrates for III-Nitride Devices”, *Proceedings of the IEEE* **98**, 1324–1338 (2010).
- <sup>30</sup>F. Bernardini and V. Fiorentini, “Spontaneous versus Piezoelectric Polarization in III-V Nitrides: Conceptual Aspects and Practical Consequences”, *Physica status solidi (b)* **216**, 391–398 (1999).

- <sup>31</sup>a. D. Bykhovski, B. L. Gelmont, and M. S. Shur, “Elastic strain relaxation and piezo-effect in GaN-AlN, GaN-AlGaN and GaN-InGaN superlattices”, *Journal of applied physics* **81**, 6332 (1997).
- <sup>32</sup>C.-F. Lin, J.-H. Zheng, Z.-J. Yang, J.-J. Dai, D.-Y. Lin, C.-Y. Chang, Z.-X. Lai, and C. S. Hong, “High-efficiency InGaN-based light-emitting diodes with nanoporous GaN:Mg structure”, *Applied physics letters* **88**, 083121 (2006).
- <sup>33</sup>Q. Wang, J. Bai, Y. P. Gong, and T. Wang, “Influence of strain relaxation on the optical properties of InGaN/GaN multiple quantum well nanorods”, *Journal of physics d: applied physics* **44**, 395102 (2011).
- <sup>34</sup>T.-H. Hsueh, H.-W. Huang, C.-C. Kao, Y.-H. Chang, M.-C. Ou-Yang, H.-C. Kuo, and S.-C. Wang, “Characterization of InGaN/GaN Multiple Quantum Well Nanorods Fabricated by Plasma Etching with Self-Assembled Nickel Metal Nanomasks”, *Japanese journal of applied physics* **44**, 2661–2663 (2005).
- <sup>35</sup>K.-C. Kim, M. C. Schmidt, H. Sato, F. Wu, N. Fellows, Z. Jia, M. Saito, S. Nakamura, S. P. DenBaars, J. S. Speck, and K. Fujito, “Study of nonpolar m-plane InGaN/GaN multiquantum well light emitting diodes grown by homoepitaxial metal-organic chemical vapor deposition”, *Applied physics letters* **91**, 181120 (2007).
- <sup>36</sup>C. H. Chiu, S. Y. Kuo, M. H. Lo, C. C. Ke, T. C. Wang, Y. T. Lee, H. C. Kuo, T. C. Lu, and S. C. Wang, “Optical properties of a-plane InGaN/GaN multiple quantum wells on r-plane sapphire substrates with different indium compositions”, *Journal of applied physics* **105**, 063105 (2009).
- <sup>37</sup>K. Xing, Y. Gong, J. Bai, and T. Wang, “InGaN/GaN quantum well structures with greatly enhanced performance on a-plane GaN grown using self-organized nano-masks”, *Applied physics letters* **99**, 181907 (2011).
- <sup>38</sup>G. a. Garrett, H. Shen, M. Wraback, A. Tyagi, M. C. Schmidt, J. S. Speck, S. P. DenBaars, and S. Nakamura, “Comparison of time-resolved photoluminescence from InGaN single quantum wells grown on nonpolar and semipolar bulk GaN substrates”, *Physica status solidi (c)* **6**, S800–S803 (2009).
- <sup>39</sup>H.-S. Chen, D.-M. Yeh, Y.-C. Lu, C.-Y. Chen, C.-F. Huang, T.-Y. Tang, C. C. Yang, C.-S. Wu, and C.-D. Chen, “Strain relaxation and quantum confinement in InGaN/GaN nanoposts”, *Nanotechnology* **17**, 1454–1458 (2006).
- <sup>40</sup>J. Bai, Q. Wang, and T. Wang, “Characterization of InGaN-based nanorod light emitting diodes with different indium compositions”, *Journal of applied physics* **111**, 113103 (2012).
- <sup>41</sup>J. Cho, E. F. Schubert, and J. K. Kim, “Efficiency droop in light-emitting diodes: Challenges and countermeasures”, *Laser & photonics reviews* **7**, 408–421 (2013).

- <sup>42</sup>J. Iveland, L. Martinelli, J. Peretti, J. S. Speck, and C. Weisbuch, “Direct Measurement of Auger Electrons Emitted from a Semiconductor Light-Emitting Diode under Electrical Injection: Identification of the Dominant Mechanism for Efficiency Droop”, *Physical review letters* **110**, 177406 (2013).
- <sup>43</sup>J. Hader, J. V. Moloney, and S. W. Koch, “Density-activated defect recombination as a possible explanation for the efficiency droop in GaN-based diodes”, *Applied physics letters* **96**, 221106 (2010).
- <sup>44</sup>J. Hader, J. V. Moloney, and S. W. Koch, “Temperature-dependence of the internal efficiency droop in GaN-based diodes”, *Applied physics letters* **99**, 181127 (2011).
- <sup>45</sup>Y. C. Shen, G. O. Mueller, S. Watanabe, N. F. Gardner, A. Munkholm, and M. R. Krames, “Auger recombination in InGaN measured by photoluminescence”, *Applied physics letters* **91**, 141101 (2007).
- <sup>46</sup>a. a. Setlur, J. J. Shiang, and U. Happek, “Eu[2+]-Mn[2+] phosphor saturation in 5 mm light emitting diode lamps”, *Applied physics letters* **92**, 081104 (2008).
- <sup>47</sup>CompoundSemiconductors, “Yole LED phosphor IP is shaping the industry”, *Compound semiconductor* (2012).
- <sup>48</sup>T. WHITAKER, “LED phosphor suppliers are affected by China’s rare-earth export quotas”, *Leds magazine*, 35 (2011).
- <sup>49</sup>H. V. Demir, S. Nizamoglu, T. Erdem, E. Mutlugun, N. Gaponik, and A. Eychmüller, “Quantum dot integrated LEDs using photonic and excitonic color conversion”, *Nano today* **6**, 632–647 (2011).
- <sup>50</sup>M. R. Krames, O. B. Shchekin, R. Mueller-Mach, G. O. Mueller, L. Zhou, G. Harbers, and M. G. Craford, “Status and Future of High-Power Light-Emitting Diodes for Solid-State Lighting”, *Journal of display technology* **3**, 160–175 (2007).
- <sup>51</sup>H. Nakanotani, K. Masui, J. Nishide, T. Shibata, and C. Adachi, “Promising operational stability of high-efficiency organic light-emitting diodes based on thermally activated delayed fluorescence.”, *Scientific reports* **3**, 2127 (2013).
- <sup>52</sup>N. J. Findlay, C. Orofino-Peña, J. Bruckbauer, S. E. T. Elmasly, S. Arumugam, A. R. Inigo, A. L. Kanibolotsky, R. W. Martin, and P. J. Skabara, “Linear oligofluorene-BODIPY structures for fluorescence applications”, *Journal of materials chemistry c* **1**, 2249 (2013).
- <sup>53</sup>S. Guha, R. A. Haight, N. A. Bojarczuk, and D. W. Kisker, “Hybrid organic-inorganic semiconductor-based light-emitting diodes”, *Journal of applied physics* **82**, 4126 (1997).
- <sup>54</sup>F. Hide, P. Kozodoy, S. P. DenBaars, and A. J. Heeger, “White light from InGaN/conjugated polymer hybrid light-emitting diodes”, *Applied physics letters* **70**, 2664 (1997).
- <sup>55</sup>J. Lee, V. C. Sundar, J. R. Heine, M. G. Bawendi, and K. F. Jensen, “Full Color Emission from II-VI Semiconductor Quantum Dot-Polymer Composites”, *Advanced materials* **12**, 1102–1105 (2000).

# CHAPTER 2

---

## Background

---

### 2.1 Semiconductors

Semiconducting materials lie between conductors, with the potential for electrical charge to flow freely and insulators, that prohibit charge flow. To explain the cause of this behaviour we first have to examine the electrical properties of solid state materials. In the solid state, atoms are bonded together through the interaction of the outer shell electrons of each atom. The nature of the bonding is related to the atomic structure, with electrons finding the most favourable (lowest) energy state. These bonding or valence electrons are locked in orbitals in between the atoms of a solid, holding the structure together in a lattice. Depending on the electronic structure of the lattice it is possible for some electrons to be unbound and free to move through the lattice and hence conduct charge.

#### 2.1.1 Band Structure

From atomic physics, the electron energy levels are quantized due to the wavelike nature of electrons allowing the possibility of interference between electrons. This leads to the electron orbitals of an atom being quantized. The de Broglie relationship, Equation 2.1, relates a wavelength  $\lambda$  to a particle of momentum  $p$  where  $h$  is Planck's constant.

$$\lambda = \frac{h}{p} \quad (2.1)$$

$$E = \frac{hc}{\lambda} \quad (2.2)$$

From this relationship it follows that increasing the energy of an electron orbiting an atom will have the inverse effect of reducing the wavelength of the electron. If the number of wavelengths in an electron orbital is a non-integer number, the electron wavefunction will



interfere with itself, leading to the condition that only integer factors of the lowest energy (ground state) electron wavelength are allowed. This gives atoms a set of discrete, bound electron energy levels up to the ionization energy where the electron is no-longer bound to the atom.

When atoms are held together in a lattice, these discrete electron energy levels overlap. The effect of this overlap is that the energy levels spread out to form bands. The valence band contains electrons that are involved in the inter-atomic bonds and have insufficient free energy to freely move through the lattice and the conduction band which contains electrons with free energy high enough to allow them to move freely through the lattice. As electrons are fermions, they are subject to the Pauli exclusion principle in that no two electrons can occupy an identical quantum state. The distribution is described by the Fermi-Dirac distribution:

$$f(E, E_F, T) = \left( \exp \left( \frac{E - E_F(T)}{K_B T} \right) + 1 \right)^{-1} \quad (2.3)$$

Where  $E_F(T)$  is the Fermi level of the material. This describes the occupation of states as a function of temperature. The wavenumber  $k$  of a charge carrier is related to wavelength by Equation 2.4 and momentum by Equation 2.5, for  $\hbar = \frac{h}{2\pi}$ . The band structure of a material can be plotted in terms of energy and wavenumber and is called the dispersion relation.

$$k = \frac{2\pi}{\lambda} \quad (2.4)$$

$$k = \frac{p}{\hbar} \quad (2.5)$$

The difference in energy between the conduction band minimum and valence band maximum is the bandgap of the material, this corresponds to the minimum amount of energy that an electron requires to be promoted from valence band maximum into the conduction band minimum. This bandgap can be either direct or indirect depending on whether the transition between bands requires a change in  $k$  and therefore momentum. The dispersion relation in Figure 2.1 shows the difference between a direct and an indirect semiconductor. It is clear that for the direct bandgap material, a transition from the conduction band minimum to the valence band maximum requires no change in  $k$ . This is in contrast to the indirect bandgap material where a change in  $k$  is required. For indirect bandgap materials this change in momentum must be supplied before a transition can take place, this requires interaction with the lattice to change the momentum of the carrier. Indirect transitions are therefore slower than direct bandgap transitions.

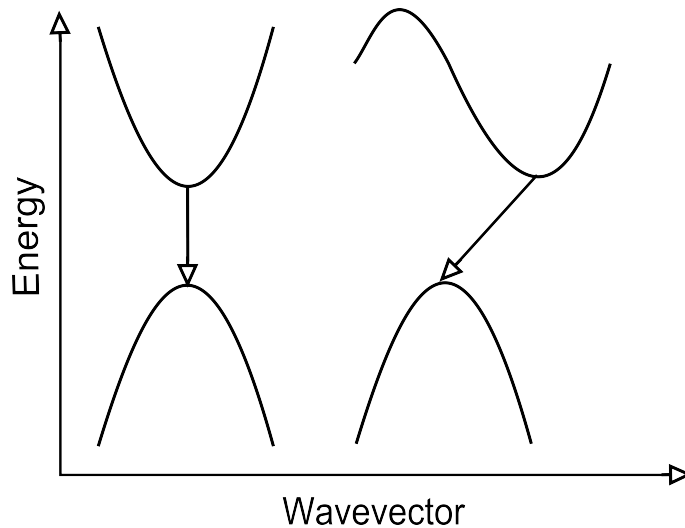


Figure 2.1: A schematic showing the simplified band structure of a direct and an indirect semiconductor

## 2.1.2 Electrons, Holes and Excitons

### Electrons in a Periodic Potential

Electrons in a semiconductor material are the negative charge carriers. In order to move freely through the lattice they must have enough free energy to exist in the conduction band. Following Kittel [1], an electron moving through a semiconductor lattice can be expressed as a wave moving through the periodic potential of the lattice. Under these conditions the electron effective mass is modified to  $m^*$  where

$$m^* = \hbar^2 \left[ \frac{d^2 E}{dk^2} \right]^{-1} \quad (2.6)$$

When an electron absorbs energy greater than the bandgap energy  $E_g$ , it is promoted to the conduction band and is free to move through the lattice, this electron state in the valence band is now vacant. This state, which is effectively a lack of an electron, is able to move through the lattice as an electron does. This hole is a quasi-particle with a positive mass  $m_h$  and a positive electron charge  $e$ . As such the hole is able to move in the valence band. It responds by moving in the opposite direction to an electron under the influence of an electric field.

### Excitons

Electrons and holes, with their opposite charges, experience a coulombic attractive force when in close proximity. This allows them to form a stable bound pair called an exciton. The model of a hydrogen atom with a single positive and a single negative charge can be used to describe an exciton. Energy is used in breaking of the bonding of an exciton and as such, excitonic recombination occurs at an energy below the bandgap (this is shown schematically in 2.2). Using the hydrogen atom model [2] the exciton

binding energy  $E_{ex}$  can be expressed as:

$$E_{ex}(n) = -\frac{\mu}{m_0} \frac{1}{\epsilon_r^2} \frac{R_H}{n^2} \quad (2.7)$$

Where,

$$\frac{1}{\mu} = \frac{1}{m_e^*} + \frac{1}{m_h^*} \quad (2.8)$$

and  $\epsilon_r$  is the relative dielectric constant and  $R_H$  is the Rydberg energy. The Rydberg energy is the energy required to completely ionize a ground state electron from a hydrogen atom ( $13.61eV$ ). The emission from excitonic recombination then occurs at an energy lower than the bandgap energy ( $E_g$ ) by the exciton binding energy  $E = E_g - E_{ex}$ . The optical properties of excitons will be covered in 2.1.5. For GaN, the free exciton binding energy is around  $20 - 23meV$  [3]. This makes room temperature stable excitons possible in GaN. Excitons in other III-nitrides and nitride nanostructures will be discussed in 2.1.7

### 2.1.3 Doping

In a perfect semiconductor material, with no defects or impurities, all electrons exist as valence electrons unless ionised into the conduction band. This situation is not practically possible and the inclusion of impurities into semiconductor materials is of significant importance. The inclusion of other elements into a semiconductor can dramatically change the carrier characteristics in the host material, this inclusion is called doping. For III-V materials such as GaN, the group III element provides three valence electrons, where as the group V element provides five. If a group IV element such as Si takes the place of a Ga atom, an extra valence electron is added to the system creating an excess of electrons, known as n-type doping. Likewise, if a group II element such as magnesium replaces a gallium atom, the system is now deficient of a valence electron, which can be seen as equivalent to adding holes to the system. This is p-type doping. In order to release the excess carriers produced by dopant atoms, they must first be thermally ionized. A good dopant therefore should have a low ionization energy relative to the thermal energy of the lattice. The addition of dopants causes the position of the Fermi level to change relative to conduction and valence bands. n-type doping leads to the Fermi level moving closer to the conduction band, and p-type doping causes the Fermi level to move towards the valence band.

### 2.1.4 Compound semiconductors

Other than the group IV semiconductors such as silicon and germanium, compound semiconductors are also of great technological importance such as the group III-V semiconductors GaAs, GaN. Compound semiconductors can be binary as in these two examples or made up of more complex alloys such as ternary AlGaIn, or quaternary AlInGaIn. Compound semiconductors tend to exhibit partially ionic bonding due to the relative sizes

Material	Bandgap Energy	Corresponding Wavelength
GaAs	1.43 eV	870 nm
InAs	0.36 eV	3444 nm
InN	0.7 eV	1771 nm
GaN	3.44 eV	364 nm
AlN	6.2 eV	200 nm
CdS	2.42	512 nm
ZnSe	2.7 eV	459 nm

Table 2.1: The bandgap energy of various common semiconductor materials with corresponding band gap wavelengths

of the different atoms involved. This partial ionicity leads to typically larger bandgaps than the elemental semiconductors[4]. The bandgaps of compound semiconductors can be continually tuned between the constituent binary compounds for example by varying the In mole fraction in InGaN, bandgaps spanning the entire visible spectrum are accessible. The change in bandgap with alloy composition is described by Vegard's law, an empirical relationship between alloy composition and bandgap.

$$E_g(\text{In}_x\text{Ga}_{1-x}\text{N}) = xE_g^{\text{InN}} + (1-x)E_g^{\text{GaN}} - bx(1-x) \quad (2.9)$$

Where  $b$  is the bowing parameter[5]. For InGaN however, the bowing factor has been found to change with indium content making  $b(x)$ [6].

### 2.1.5 Semiconductor Optics

The interaction between carriers in the semiconductor and photons allows for interesting optical processes to take place due to the band gap of semiconducting materials. Using Equation 2.2 energy is expressed in units of electron volts . We find that the band gaps of the common semiconductor materials from Table 2.1 [7] correspond to wavelengths of optical significance from infra-red to ultraviolet depending on material. The region between conduction and valence bands contains no charge carrier states due to the periodicity of the band structure. The only way for an excited electron in the conduction band to relax back to the valence band is to lose the bandgap energy  $E_g$ . This can be a radiative process, by emission of a photon, or a non-radiative process where the energy is lost by non-optical means such as heat in the form of lattice vibrations.

### 2.1.6 Optical Transitions in Semiconductors

Some of the potential carrier recombination mechanisms are highlighted in 2.2. An incident photon with energy larger than the bandgap energy  $E_{h\nu} > E_g$  can be absorbed by an electron, promoting the electron up to the conduction band and leaving a hole in the valence band. The electron can quickly lose the excess energy above the conduction band edge  $E_g - E_{h\nu}$  by emission of phonons (lattice vibrations or heat). Statistically it is more

energetically stable for the electron to lose the bandgap energy and recombine with the hole in the valence band than to remain in an excited state [2]. After a characteristic time, termed the spontaneous emission lifetime, the electron emits a photon of energy  $E_g$  and returns to the valence band. It is also possible for a free exciton to recombine in the same way, in this situation the energy of the emitted photon is reduced by the exciton binding energy  $E_g - E_{excitonbinding}$ . When donor-acceptor recombination occurs the emitted photon energy is reduced by the activation energy of the respective dopants. It is also for the excited electron to non-radiatively recombine with the hole in the valence band. The mechanisms for non-radiative recombination can be that the electron loses energy as heat dropping down to the intermediate energy levels of defects in the lattice. Auger recombination is also possible, this is a three particle process. Where a recombining electron and hole transfer their energy into a exciting a third carrier to an excited high energy state.

The recombination lifetime of the material is determined by the radiative recombination lifetime and the non-radiative recombination lifetime as shown in Equation 2.10 where  $\tau_r$  and  $\tau_{nr}$  are the radiative and non-radiative lifetimes respectively. The non-radiative lifetime is sensitive to the quality of the material (e.g. defect density) and indirectly to temperature as many non-radiative recombination centres are frozen out at low temperature when the thermal energy is lower than the defect activation energy. The free exciton lifetime in gallium nitride at low temperature has been found to be  $295ps$  [8].

$$\frac{1}{\tau} = \frac{1}{\tau_r} + \frac{1}{\tau_{nr}} \quad (2.10)$$

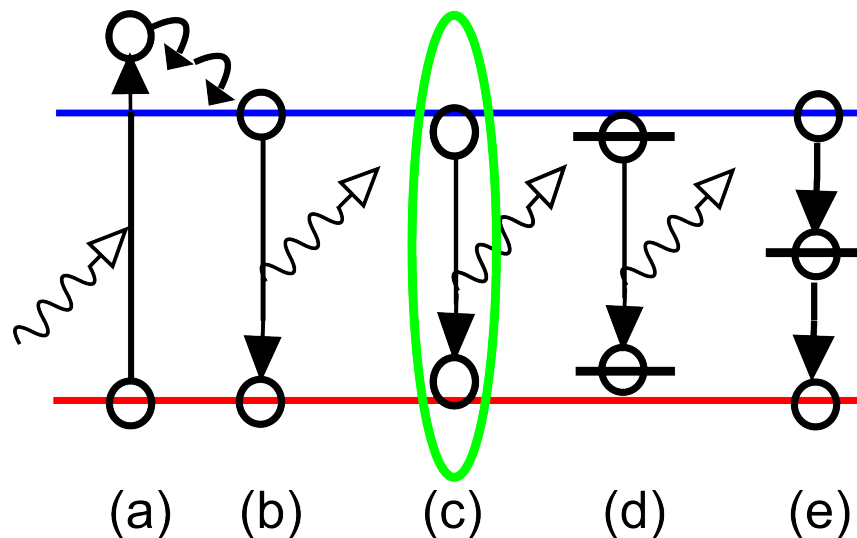


Figure 2.2: Possible carrier excitation and relaxation mechanisms. (a) absorption of a photon with  $E > E_g$  (b) Spontaneous emission from band edge (c) Excitonic recombination (d) Donor acceptor recombination (e) Non-radiative recombination via defects or deep level states

## 2.1.7 Low Dimensional Structures

Through precise control of the growth of semiconductor materials it is possible to alternate between different alloy compositions within several atomic layers ( $\sim 0.1$ - $10$ 's of nm). Structures on such small scales allow the potential to control carriers due to spatial confinement effects. The de Broglie energy of an electron in the conduction band of a bulk semiconductor is given by Equation 2.1. Where the momentum of the electron is due to the thermal kinetic energy of the electron in three dimensions is given by Equation 2.11 [9].

$$E_{thermal} = \frac{p_{(x,y,z)}^2}{2m_e^*} \quad (2.11)$$

With the de Broglie wavelength of the electron of

$$\lambda \approx \frac{h}{\sqrt{m_e^* k_B T}} \quad (2.12)$$

When the length scales of a structure become smaller than the de Broglie wavelength of carriers in the material, the energies of such particles become quantized. This is analogous to the discrete energy levels of electrons in an atom. Such effects are quantum in nature. This is typically derived for the ‘particle in a box’ example using Equation 2.13 the time dependent Schrödinger equation in one dimension. Following Phillips [10].

$$-\frac{\hbar^2}{2m} \frac{\partial^2}{\partial x^2} \Psi(x, t) + V(x) \Psi(x, t) = i\hbar \frac{\partial}{\partial t} \Psi(x, t) \quad (2.13)$$

Where  $\hbar$  is the reduced Planck's constant,  $m$  is the mass of the particle,  $\Psi(x, t)$  is the wavefunction of the particle,  $V(x, t)$  is the potential energy of the particle and  $i$  is  $\sqrt{-1}$ . For a particle moving inside a box with zero potential in the region  $0 < x < a$  and no wavefunction outside the box, a freely propagating wavefunction of

$$\Psi(x) = N \sin k_n x e^{-iE_n t/\hbar} \quad (2.14)$$

yields that the energy of the particle is expressed by Equation 2.15.  $n$  is an integer, giving that the allowed energy of a particle in an infinite box is quantized in integer values of  $n$ .

$$E_n = \frac{\hbar^2 k_n^2}{2m} \quad (2.15)$$

Where:

$$k_n = \frac{n\pi}{a} \quad (2.16)$$

These quantum confined structures are also termed low dimensional structures, with this one dimensional quantum well structure showing confinement in one dimension and no confinement in the other two spatial dimensions. The quantum well structures can be practically realised by growing alternate layers of semiconductor materials with different

bandgaps. For example, GaN has a bandgap of  $3.4eV$  and an alloy of InGaN has a smaller bandgap, which depends on the relative content of In and Ga (InN bandgap being  $0.7eV$ ). A charge carrier can be confined in a thin layer of InGaN between barrier layers of GaN. In typical usage it is common to use several quantum wells together to increase the active area this is termed multiple quantum wells (MQW). Figure 2.3 shows the band structure of a single InGaN/GaN quantum well with the electron and hole wavefunctions  $n = 1$  and  $n = 2$  levels.

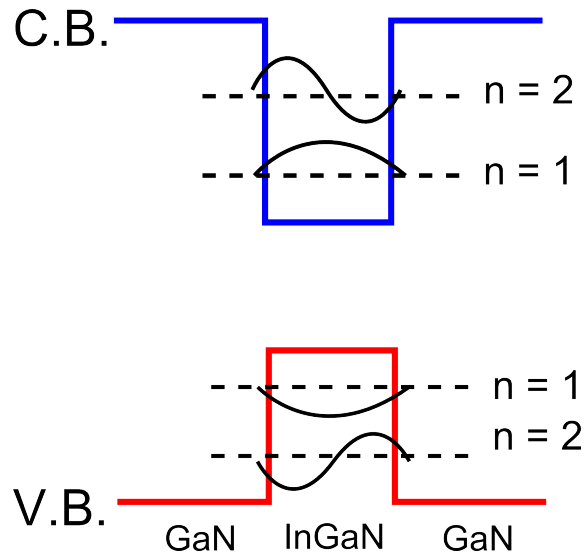


Figure 2.3: An InGaN/GaN quantum well with schematic electron and hole wavefunctions shown in the conduction and valence bands respectively

The use of such quantum well structures has multiple benefits for light emitting structures. The confinement of carriers in the quantum well region acts as a trap, where carriers injected into the device remain until electrons drop back down to the valence band emitting their excess energy as either light or heat. Control of the quantum well thickness also allows the bandgap to be precisely controlled. This is evident from Equation 2.16 as the wavenumber is dependent on the width of the well.

### Excitons in Quantum Confined Structures

As discussed in Section 2.1.2, electron-hole pairs can coulombically combine into excitons. In quantum confined structures the electron-hole wavefunctions are spatially confined which can significantly influence the exciton binding energy of excitons within the nanostructure[11]. The exciton binding energy in InGaN quantum wells can be significantly higher than that of the bulk semiconductor of the order of  $50meV$  [12].

### 2.1.8 p-n Junctions

When a p-doped and n-doped semiconductor are brought together the excess of electrons in the n-type and the excess of holes in the p-type combine in the interface. Electrons

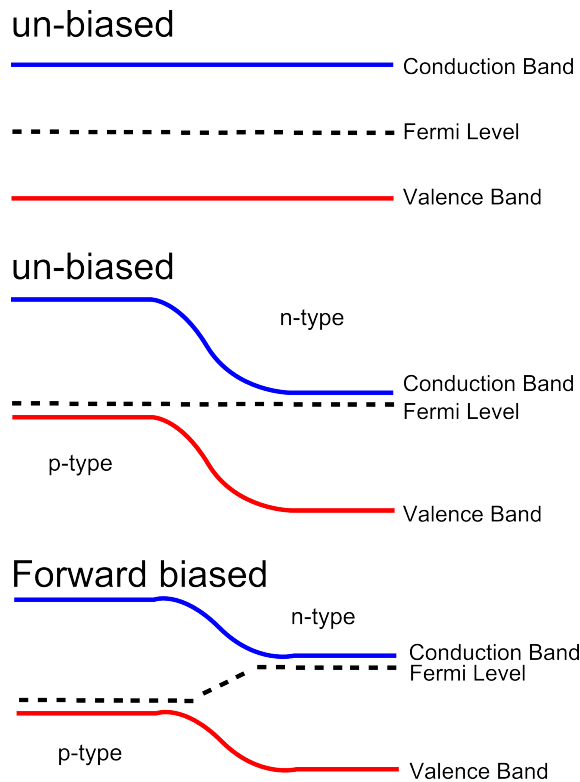


Figure 2.4: Band structures of an un-doped semiconductor, an unbiased p-n junction and a p-n junction under forward bias

flow from the n-type into the p-type and create a depletion region where donors and acceptors are ionized. The effect of this p-n junction is shown in Figure 2.4, the valence and conduction bands are bent to meet. When an electric field is applied to this structure current is only able to flow under forward bias. The voltage reduces the depletion region width, electrons flow into the n-type and holes into the p-type. Under reverse bias, the electric field increases the depletion region width and restricts the flow of carriers.

## Light Emitting Diodes

Light emitting diodes (LEDs) are a special case of a diode where the injected carriers are allowed to radiatively recombine across the bandgap. In diodes such as those based on Si that is an indirect bandgap material, recombination at the junction is dominated by non-radiative processes. Using direct bandgap materials such as the III-nitrides allows radiative recombination processes to dominate converting the energy loss of carriers across the bandgap into light. The wavelength of the emission from an LED is therefore determined by the bandgap of the material used. In order to achieve white emission there are three main methods: Mixing components of different colours such as red, green, blue. Through the use of a blue emitting nitride LED coupled with a colour converting phosphor material. The use of a UV emitting LED to excite red, green and blue phosphors. Due to the practical benefits of using a single device and a single material, by far the most prevalent device used commercially is a blue emitting InGaN/GaN quantum well based LED coupled to a blue absorbing, yellow emitting phosphor material as a colour



converter.

## 2.2 III-nitride Semiconductors

Semiconductors made using the III-V elements have been a focus of research and industrial interest for many decades due to the useful range of bandgaps from infra-red through to ultra-violet and the fact that many materials in this group are direct bandgap semiconductors. The most well established III-V semiconductors are the arsenide (GaAs, InAs etc.) and phosphide (InP, GaAsP, etc.) materials. During the 1980's and 1990's work in Japan opened up the huge potential of III-nitride based semiconductors. The breakthrough was a commercially viable technique to successfully p-doped nitride materials. This allowed the first useful devices to be fabricated. The III-nitride semiconductors, AlN and GaN are wide bandgap semiconductors with UV bandgaps of  $6.2eV$  and  $3.44eV$  respectively, InN has a narrower bandgap of  $0.7eV$ . Through the alloying of these materials it is possible to produce ternary and quaternary semiconductors with bandgaps from infrared to ultraviolet. The most commonly used material for LEDs is the ternary alloy InGaN, with In compositions of between 10 – 30%. The bandgap wavelength can be controlled from blue to green [13–15].

### 2.2.1 Crystal Structure

III-Nitride materials can exist in both the cubic and wurtzite crystal structures. Predominantly, GaN materials for commercial and research purposes are wurtzite due to the stability of these materials. Cubic III-nitride materials have been studied for since the early stages of the development of III-nitride materials mainly using Molecular Beam Epitaxy as the lower growth temperatures allow the successful growth of stable cubic phase III-nitrides.

### 2.2.2 Polarization and the Quantum Confined Stark Effect

The III-nitride materials are predominantly wurtzite lattice structure, polarity in the (0001) c-axis in the wurtzite configuration. III-nitride materials inherently exhibit spontaneous polarization due to the symmetry of the wurtzite lattice and can exhibit piezoelectric polarization fields when strained [16]. This causes problems when alloys of Ga,In,Al-nitride are grown due to the different lattice constants of each material. The lattice constants of GaN are  $a = 0.319nm$ ,  $c = 0.5185nm$  while for InN  $a = 0.3533nm$  and  $c = 0.5693nm$  [17]. The effect of this is that if a layer of InGaN is grown on top of a layer of GaN the InGaN experiences compressive strain due to the lattice constant difference. For a piezoelectric material this strain results in an electric field across the material. The effect of this electric field is especially significant for the quantum well structures that are important for LEDs where it generates the quantum confined stark effect (QCSE). In

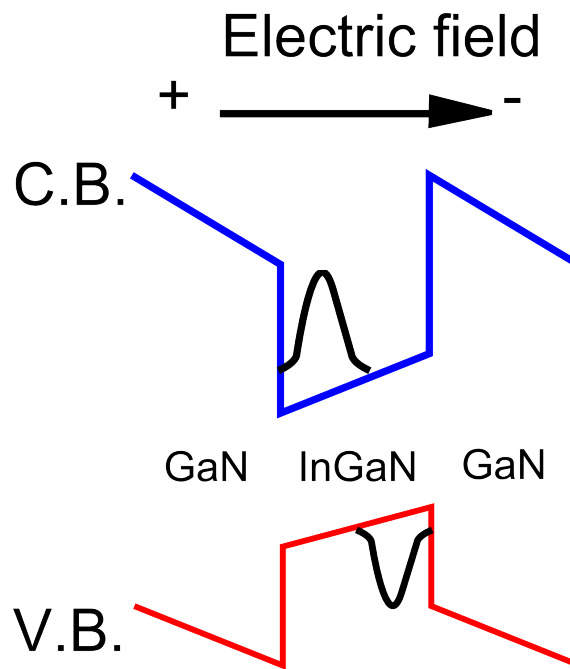


Figure 2.5: An InGaN/GaN quantum well the effect of the quantum confined Stark effect on schematic electron and hole wavefunctions shown as the bands are tilted and the wavefunction overlap is reduced

a quantum confined structure such as a quantum well when an applied electric field is in the direction of confinement the confined wavefunctions are modified by the field. In the case of a quantum well, the electron wavefunction in the conduction band and the hole wavefunction in the valence band are separated as the electron and hole have opposite charge and therefore are bent in opposite directions by the electric field [18]. This effect has been widely studied for over 15 years [19] and is a well known problem for standard InGaN/GaN MQW structures where the electric field is in the *c*-axis, the same orientation as the confinement of the quantum wells. The effect is shown in Figure 2.5. By separating the electron and hole wavefunctions the probability of a direct optical transition across the bandgap is reduced, leading to an increase in the radiative recombination lifetime and lower efficiency optoelectronic devices. As such QCSE presents a major efficiency limiting issue for visible emitting LEDs grown on *c*-plane sapphire.

### 2.2.3 Growth of III-Nitride Materials

The two main growth techniques used for the other III-V semiconductors can also be used for III-nitrides, metal organic chemical vapour deposition (MOCVD) and molecular beam epitaxy (MBE). The predominant method in the mass production of LEDs is MOCVD due to the high volume and throughput possible with this system. All samples used in this work were grown by MOCVD by members of the Sheffield nitrides group.

## MOCVD

A variant of the wide spread chemical vapour deposition techniques, MOCVD uses metal organic materials as sources for the deposition. The basic process of MOCVD involves reacting metal organic precursors on a substrate to form III-nitride materials. The metal organic sources are tri-methyl aluminium, tri-methyl gallium and tri-methyl indium (TMA, TMG, TMI respectively). A carrier gas (hydrogen or nitrogen) is bubbled through the metal organic source which carries the metal organic source with it as a vapour. The carrier gas is then passed over the growth substrate to supply the group III element. Ammonia is used as the nitrogen source. This also flows over the substrate and the two are made to react at the substrate by increasing the substrate temperature. Due to the bonding energy of nitride materials, high substrate temperatures are required for the growth of nitrides compared to other III-V semiconductors.

### 2.2.4 Substrates

Whereas many semiconductor material systems are able to use homo-epitaxy (growth on a substrate of identical material) III-nitride substrates are still prohibitively expensive due to the difficulties in producing them. The most common substrate for the growth of III-nitride materials is sapphire. Typically III-Nitride films are grown in the c-plane (0001) direction where the c-axis, spontaneous and polarization fields are perpendicular to the wafer surface (in the growth direction). This growth method leads to the QCSE problem discussed previously. Over the last decade great efforts have been made to attempt to grow III-nitrides in different polar orientations so that the polarized axis (0001) is perpendicular or at a non-parallel angle to the growth direction. In the first case where the polarization field is perpendicular to the growth direction, a quantum well structure has no electric field in the direction of quantum confinement and therefore there is no QCSE effect, this orientation is termed non-polar. For the polarization field at an angle between parallel and perpendicular, the component parallel to the growth direction is reduced, this is termed semi-polar. So far, hetero-epitaxy using sapphire to grow non-polar gallium nitride has met with mixed results. Other substrates such as  $LiAlO_2$  have been used to grow GaN and InGaN/GaN quantum wells [20–23]. Growth on sapphire using patterned area growth, overgrowth techniques, three-dimensional growth, and homo epitaxy are all being investigated internationally [24–27]

### 2.2.5 Localization Effects

The effect of localization on the local band structure is shown in Figure 2.6, the localization centres appear as local fluctuations in the bandgap of the material. These localization centres with lower bandgap energy are able to trap carriers. The depth of these localization centres determines the degree of localization behaviour in the material. Typically in InGaN materials the average localization energies or depths  $E_{loc}$  are on the order

of tens of meV [28, 29]. This is comparable to the thermal energy  $kT = 26\text{meV}$  at room temperature which means that depending on the temperature of the material, carriers are either able to perform a thermally assisted hop between localization centres or to become fully de-localized (as represented in Figure 2.6). Using low quality non-polar InGaN/GaN MQWs grown on sapphire, it has been found that the localization depth can be as high as  $175\text{meV}$  for a  $3\text{nm}$  quantum well width [22]. Due to the values of localization depth being comparable to the thermal energy  $kT$  at room temperature, the radiative emission spectrum of a sample as a function of temperature shows artefacts of the localization and de-localization of carriers as the thermal energy is varied in relation to the localization energy. Disordered systems such as InGaN alloys with In clustering can exhibit an s-shaped dependence on emission energy with increasing temperature. The cause of this temperature dependence has been related to the change in dominant recombination from radiative at low temperatures ( $T < 70\text{K}$ ) to non-radiative at higher temperatures, changing the probability of diffusion to local potential minima and to non-radiative recombination centres [30].

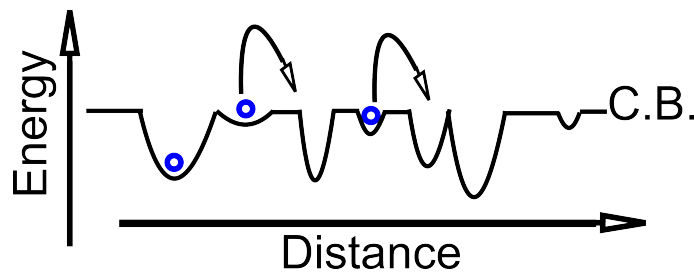


Figure 2.6: Localization shown in the conduction band as a function of position

## Nanorods

In recent years there has been significant interest in III-nitride based nanorod structures. The formation of nanorods leads to changes in the material and optical properties compared to a standard two-dimensional epi-wafer. These effects range from the relaxation of strain (and piezo-electric field) [31], the use of periodic arrays of nanorods to create photonic crystal effects [32, 33] to the use of nanorods arrays as overgrowth templates to increase the crystal quality of heteroepitaxial materials [26]. The properties of InGaN/GaN quantum well nanorods will be studied in Chapter 4.

### 2.2.6 White LEDs

White light is based on the response of the eye to the solar spectrum, as such, a typically white spectrum is close to black body radiation at a temperature of  $6000\text{K}$  (similar to the temperature of the surface of the sun). The human eye has evolved in this lighting environment and in order to make lighting conditions comfortable. Artificial light should reasonably closely match this spectral profile. The successes of InGaN based blue

emitting LEDs paved the way for the use of entirely solid state white lighting. The most straightforward route to producing white light with LEDs would be to combine LEDs with overlapping spectra through the entire visible range to best replicate the solar spectrum. In practice however, LEDs are not available at all wavelengths of the visible spectrum, especially with reasonable efficiencies. Due to these limitations the two most common routes to generate white light are the use of discrete red, green and blue LEDs (RGB), or the use of a short wavelength blue LED coupled with a down-conversion phosphor material to convert a portion of the blue emission to longer wavelengths.

## 2.3 Organic Semiconductors

The history of organic semiconductors is considerably shorter than that of inorganic semiconductors. However organic semiconductors have come to prominence in recent years. As opposed to consisting of hard, crystalline materials of silicon or III-V materials, organic semiconductors are carbon based molecules. As semiconductors they exhibit behaviour similar to classical semiconductors, with forbidden energy bands and electrical conduction only above these band gap energies. The mechanisms generating these properties are different to those of the classical semiconductors and will be discussed in the section. The development of organic semiconducting materials has been driven by the application of organic optoelectronics, particularly the organic LED (OLED) and organic photo voltaic(OPV). In a similar fashion to the development of inorganic LEDs, early work examined luminescence of some novel materials under the application of relatively high voltages. The first significant breakthrough in the development of organic optoelectronic devices came with the demonstration of the first organic LED [34] using a dual organic layer diode heterostructure. This approach allowed significantly higher electrical injection efficiencies to be achieved resulting in light emission at a far lower electrical bias and therefore higher device efficiencies. Following this initial work, device efficiencies were improved significantly through the use of alternative organic semiconductor materials such as conjugated organic polymers particularly in the work carried out at the Cavendish laboratory [35].

Organic semiconductors possess a band structure analogous to that of inorganic semiconductors. Due to the overlap of bonds within molecules, discrete atomic transitions become molecular bands. These bands are termed the highest occupied molecular orbital (HOMO) and the lowest unoccupied molecular orbital (LUMO) analogous to the valence and conduction bands respectively. Conjugated bonds in organic materials consist of  $\pi$  orbitals which form a delocalized  $\pi$  orbital bond between long chains of carbon atoms (shown schematically in Figure 2.8). These delocalized electron orbitals allow the conduction of electrons in conjugated organic molecules analogous to delocalized electrons free to move in the conduction band of an inorganic semiconductor.

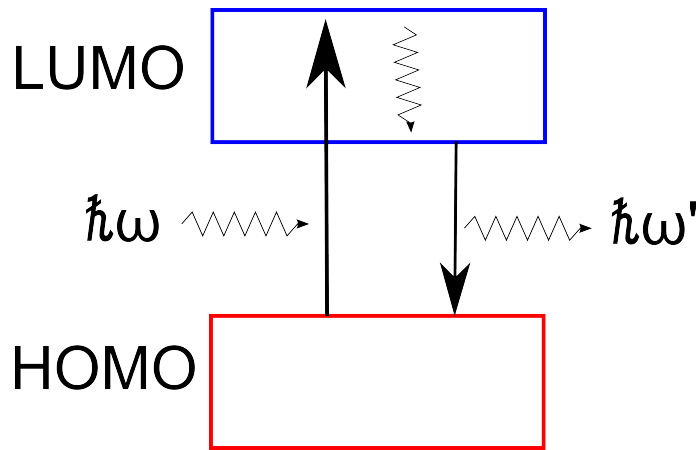


Figure 2.7: The HOMO and LUMO bands of a molecule, with optical transitions displayed, absorption of a photon of energy  $\hbar\omega$ , non-radiative relaxation, and radiative recombination with release of phonon with energy  $\hbar\omega'$

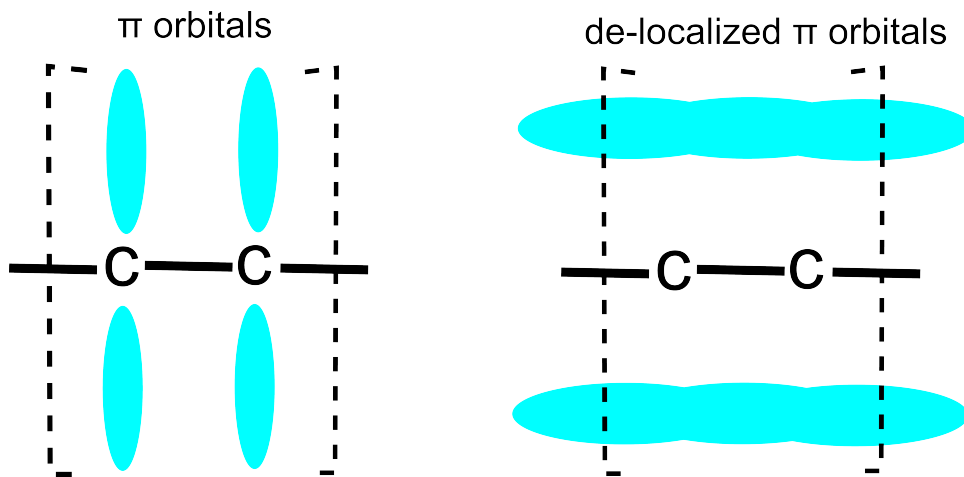


Figure 2.8: Bonded carbon atoms in a chain, showing the  $\pi$  orbitals and the delocalized, conjugated  $\pi$  orbitals that allow carrier transport

### 2.3.1 Hybrid White LEDs

Commercially available LEDs typically use the blue emitting InGaN/GaN MQW LED radiatively pumping a yellow emitting phosphor system. With the development of organic semiconducting molecules capable of exhibiting similar optical properties to direct bandgap inorganic semiconductor devices were demonstrated using blue emitting InGaN LEDs as a radiative pump for a light emitting polymer [36] as well as UV LEDs with multicoloured polymer blends to achieve white light emission [37]. It is predicted that it is possible to utilize a different coupling mechanism between InGaN quantum wells and an organic light emitter under specific conditions [38]. The coupling mechanism proposed was Forster Resonant Energy Transfer (FRET). Andrews [39] used quantum electrodynamics calculations to show that FRET is the near field asymptote of radiative energy transfer, where instead of the transfer of energy between two resonant dipoles by exchange of a photon, a coupling of the near-fields of two dipoles energy can be exchanged by a virtual photon. As a near field coupling the effect requires very low separation of

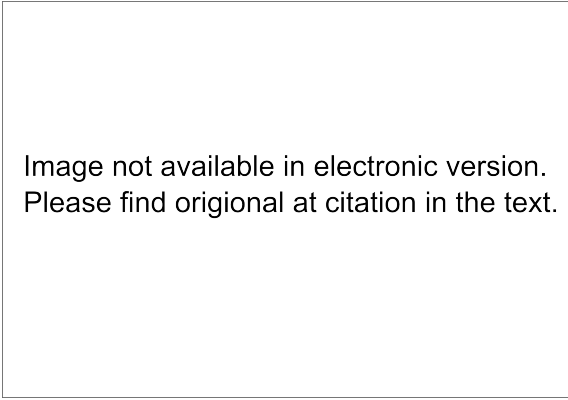


Image not available in electronic version.  
Please find original at citation in the text.

Figure 2.9: A schematic taken from [40], showing their non-radiative energy transfer pumped white emitting structure. With InGaN quantum well excitons non-radiatively coupled to down converting quantum dots through the thin top barrier layer. Re-printed from Nature Publishing

the donor dipole and acceptor dipole on the order of  $< 10\text{nm}$  [38]. In this regime the donor dipole is an InGaN quantum well exciton and the acceptor dipole is an exciton in the organic material.

A working example was demonstrated where an InGaN quantum well based structure was used to non-radiatively pump a layer of semiconductor nanocrystals as a down-converting material using FRET[40]. The method used reduce donor/acceptor dipole separation was a single InGaN quantum well with a thin top GaN barrier (3nm), a layer of CdSe/ZnS nanocrystal quantum dots with absorption overlapping the InGaN quantum well emission was deposited on top of this thin top barrier. A schematic from this work is shown in Figure 2.9. Through the use of time resolved photoluminescence measurements the presence of FRET based energy transfer between the InGaN quantum well and the CdSe/ZnS was demonstrated.

Further work was carried out by Heliotis et al. [41], using a similar device structure with a single InGaN quantum well and thin top GaN barrier, this time non-radiatively coupled to an organic light emitting polymer (F8DP). In this work three InGaN single quantum well samples were grown with different capping layer heights of 2.5, 4 and 15nm a layer of F8DP deposited on the surface. Increasing the separation of InGaN quantum well and F8DP excitons it was possible to move out of the range of the near-field non-radiative energy transfer effect. Exploiting the fact that F8DP shows no temperature dependence in photoluminescence emission whereas InGaN has a highly temperature sensitive emission intensity. Temperature dependent photoluminescence measurements were carried out. The difference in temperature dependence of the emission of each sample was used to highlight the energy transfer mechanisms in place.

Attempts were made to increase the efficiency of such hybrid devices by employing higher efficiency InGaN/GaN multiple quantum well structures as opposed to lower efficiency single quantum wells, in order to maintain the low separation needed for the non-radiative energy transfer various nano-structuring techniques have been applied to the

Image not available in electronic version.  
Please find original at citation in the text.

Figure 2.10: An image from [42], showing a schematic of the two nanostructured samples designed to couple InGaN quantum wells to nanocrystal quantum dots by non-radiative energy transfer.

III-nitride. Chanyawadee et al. [42] used InGaN/GaN MQWs as the non-radiative energy transfer donor to pump CdSe/CdS nanocrystal quantum dots as the down converter. In order to reduce MQW exciton, nanocrystal exciton separation a set of nano-pits were etched through the quantum well layers. Nano-imprint lithography was used to mask a pattern of nano dots and dashes. These were etched through the MQW layer for one sample and for a second sample the etch was stopped before reaching the quantum well layer. The holes were filled with the CdSe/CdS nanocrystals, giving one sample with low exciton separation and one with large exciton separation. Time resolved photoluminescence was used to show the change in carrier lifetime as carriers were non-radiative transferred out of the quantum wells in the low separation structure.

InGaN/GaN MQW nanorod structures were fabricated using a top down etch technique by Nizamoglu et al. [43]. Nanocrystal quantum dots were then deposited in the space between nanorods in contact with the quantum well sidewalls. This approach allows the separation between quantum well excitons and nanocrystal to be reduced. Using a time resolved investigation of the MQW decay dynamics, the reduction in carrier lifetime was used to demonstrate non-radiative energy transfer from MQW to nanocrystals.

The exact dependence of non-radiative energy transfer rate on exciton separation is determined by several factors. It was demonstrated Hill et al. [44] that the original theoretical model proposed by Theore Förster in 1946 for non-radiative energy transfer between two point source molecules is significantly modified for different molecule geometries. The Langmuir-Blodgett technique was used to fabricate highly ordered two dimensional films of molecules deposited with a carefully controlled spacer molecule layer, by changing the number of mono-layers of spacer between the donor and acceptor film and examining the energy transfer rate. It was found that instead of the  $\Gamma \propto R^{-6}$  dependence of energy transfer rate on dipole separation for point sources. The dependence drops to  $\Gamma \propto R^{-2}$  for highly ordered two dimensional films.

It was predicted in initial theoretical work that, although the FRET process has no inherent temperature dependence, localization of excitons in the donor quantum well could



effect the rate of non-radiative energy transfer to an organic overlayer [38]. This behaviour leads to an indirect temperature dependence of non-radiative energy transfer as quantum well excitons transition between localized and free with thermal energy. This theoretical prediction was confirmed by experimental work recently [45]. Using a single GaN quantum well with AlGaN barriers and a thin (4nm) AlGaN top barrier, coupled to a light emitting polymer (F8BT), the temperature dependence of energy transfer between GaN quantum well and F8BT was examined as a function of temperature using temperature dependent time resolved photoluminescence measurements. The temperature dependence is actually an exciton localization dependence, caused by the relationship between dipolar coupling and dipole wavevector given in Equation 2.17 from Rindermann et al.[45] where  $k$  is the in-plane wavevector amplitude,  $d$  is dipole separation.

$$V(k, d) \propto ke^{-kd} \quad (2.17)$$

Due to the dependence of non-radiative energy transfer rate on dipole orientation, localization, wavevector and exciton type (Wannier-Mott, Frenkel) it is not always possible to determine the exact coupling geometry in some systems, especially nanostructured systems. It has been observed with many different approaches that the upper limit for non-radiative energy transfer from an InGaN quantum well to an acceptor material lies between 5-10nm dipole separation [38, 41, 46, 47].

## References

- <sup>1</sup>C. Kittel, *Introduction to Solid State Physics*, Eighth (John Wiley & Sons, inc, 2005).
- <sup>2</sup>M. Fox, *Optical Properties of Solids*, Second (Oxford University Press, 2010).
- <sup>3</sup>J. F. Muth, J. H. Lee, I. K. Shmagin, R. M. Kolbas, H. C. Casey, B. P. Keller, U. K. Mishra, and S. P. DenBaars, "Absorption coefficient, energy gap, exciton binding energy, and recombination lifetime of GaN obtained from transmission measurements", *Applied physics letters* **71**, 2572 (1997).
- <sup>4</sup>P. Y. Yu and M. Cardona, "Introduction", in *Fundamentals of semiconductors*, Graduate Texts in Physics (Springer Berlin Heidelberg, Berlin, Heidelberg, 2010), pages 1–18.
- <sup>5</sup>C. G. Van de Walle, M. McCluskey, C. Master, L. Romano, and N. Johnson, "Large and composition-dependent band gap bowing in In<sub>x</sub>Ga<sub>1-x</sub>N alloys", *Materials science and engineering: b* **59**, 274–278 (1999).
- <sup>6</sup>P. G. Moses and C. G. Van de Walle, "Band bowing and band alignment in InGaN alloys", *Applied physics letters* **96**, 021908 (2010).
- <sup>7</sup>C. F. Klingshrin, *Semiconductor Optics*, Third (Springer, 2007).

- <sup>8</sup>G. E. Bunea, W. D. Herzog, M. S. Unlu, B. B. Goldberg, and R. J. Molnar, “Time-resolved photoluminescence studies of free and donor-bound exciton in GaN grown by hydride vapor phase epitaxy”, *Applied physics letters* **75**, 838–840 (1999).
- <sup>9</sup>M. Fox, “Low Dimensional Semiconductor Structures”, in *Quantum optics an introduction* (Oxford University Press, Cambridge, 2006) Chap. D, pages 333–338.
- <sup>10</sup>A. C. Phillips, *Introduction to Quantum Mechanics* (Wiley, 2003).
- <sup>11</sup>S. F. Chichibu, Y. Kawakami, and T. Sota, “Emission Mechanisms and Excitons in GaN and InGaN Bulk and QWs”, in *Introduction to nitride semiconductor blue lasers and light emitting diodes*, edited by S. Nakamura and S. F. Chichibu (CRC PRESS, 2000), pages 153–270.
- <sup>12</sup>J. I. Lee, C. M. Lee, J. Y. LEEM, K.-S. Lim, and I. K. Han, “Optical properties of InGaN/GaN multiple quantum wells”, *Journal of the korean physical society* **41**, 386–389 (2002).
- <sup>13</sup>V. Davydov, A. Klochikhin, V. Emtsev, D. Kurdyukov, S. Ivanov, V. Vekshin, F. Bechstedt, J. Furthmüller, J. Aderhold, J. Graul, A. Mudryi, H. Harima, A. Hashimoto, A. Yamamoto, and E. Haller, “Band Gap of Hexagonal InN and InGaN Alloys”, *Physica status solidi (b)* **234**, 787–795 (2002).
- <sup>14</sup>M. D. McCluskey, C. G. Van de Walle, L. T. Romano, B. S. Krusor, and N. M. Johnson, “Effect of composition on the band gap of strained InGaN alloys”, *Journal of applied physics* **93**, 4340 (2003).
- <sup>15</sup>C. H. Chiu, S. Y. Kuo, M. H. Lo, C. C. Ke, T. C. Wang, Y. T. Lee, H. C. Kuo, T. C. Lu, and S. C. Wang, “Optical properties of a-plane InGaN/GaN multiple quantum wells on r-plane sapphire substrates with different indium compositions”, *Journal of applied physics* **105**, 063105 (2009).
- <sup>16</sup>B. Gil, “Stress Effects on Optical Properties”, in *Gallium nitride ii* (Academic Press, 1999), pages 209–271.
- <sup>17</sup>A. Zubrilov, *Properties of Advanced Semiconductor Materials GaN, AlN, InN, BN, SiC, SiGe* (John Wiley & Sons, inc, 2001), pages 49–66.
- <sup>18</sup>S. Chichibu, a. Abare, M. Mack, M. Minsky, T. Deguchi, D. Cohen, P. Kozodoy, S. Fleischer, S. Keller, and J. Speck, “Optical properties of InGaN quantum wells”, *Materials science and engineering b* **59**, 298–306 (1999).
- <sup>19</sup>P. Perlin, C. Kisielowski, V. Iota, B. a. Weinstein, L. Mattos, N. a. Shapiro, J. Kruger, E. R. Weber, and J. Yang, “InGaN/GaN quantum wells studied by high pressure, variable temperature, and excitation power spectroscopy”, *Applied physics letters* **73**, 2778 (1998).
- <sup>20</sup>P. Waltereit, O. Brandt, A. Trampert, H. Grahn, J. Menniger, M. Ramsteiner, M. Reiche, and K. Ploog, “Nitride semiconductors free of electrostatic fields for efficient white light-emitting diodes”, *Nature* **406**, 865–8 (2000).

- <sup>21</sup>Y. Sun, O. Brandt, S. Cronenberg, S. Dhar, H. Grahn, K. Ploog, P. Waltereit, and J. Speck, “Nonpolar In<sub>x</sub>Ga<sub>1-x</sub>N/GaN(11-00) multiple quantum wells grown on  $\gamma$ -LiAlO<sub>2</sub>(100) by plasma-assisted molecular-beam epitaxy”, *Physical review b* **67**, 041306 (2003).
- <sup>22</sup>T. S. Ko, T. C. Lu, T. C. Wang, J. R. Chen, R. C. Gao, M. H. Lo, H. C. Kuo, S. C. Wang, and J. L. Shen, “Optical study of a-plane InGa<sub>N</sub>/Ga<sub>N</sub> multiple quantum wells with different well widths grown by metal-organic chemical vapor deposition”, *Journal of applied physics* **104**, 093106 (2008).
- <sup>23</sup>H. D.R., C. MitchM., L. J.L., and H. M., “Optical Investigations of Non-polar -plane In-GaN/GaN Multiple Quantum Wells Grown on LiAlO (100) by Using MOVPE”, *Journal of the korean physical society* **55**, 250 (2009).
- <sup>24</sup>C. Netzel, C. Mauder, T. Wernicke, B. Reuters, H. Kalisch, M. Heuken, A. Vescan, M. Weyers, and M. Kneissl, “Strong charge carrier localization interacting with extensive nonradiative recombination in heteroepitaxially grown m-plane GaInN quantum wells”, *Semiconductor science and technology* **26**, 105017 (2011).
- <sup>25</sup>T. Paskova, “Development and prospects of nitride materials and devices with nonpolar surfaces”, *Physica status solidi (b)* **245**, 1011–1025 (2008).
- <sup>26</sup>K. Xing, Y. Gong, J. Bai, and T. Wang, “InGa<sub>N</sub>/Ga<sub>N</sub> quantum well structures with greatly enhanced performance on a-plane Ga<sub>N</sub> grown using self-organized nano-masks”, *Applied physics letters* **99**, 181907 (2011).
- <sup>27</sup>S. Srinivasan, M. Stevens, F. a. Ponce, H. Omiya, and T. Mukai, “Carrier dynamics and electrostatic potential variation in InGa<sub>N</sub> quantum wells grown on {1122} Ga<sub>N</sub> pyramidal planes”, *Applied physics letters* **89**, 231908 (2006).
- <sup>28</sup>S. Chichibu, T. Sota, K. Wada, and S. Nakamura, “Exciton localization in InGa<sub>N</sub> quantum well devices”, *Journal of vacuum science & technology b: microelectronics and nanometer structures* **16**, 2204 (1998).
- <sup>29</sup>J. H. Na, R. a. Taylor, K. H. Lee, T. Wang, A. Tahraoui, P. Parbrook, a. M. Fox, S. N. Yi, Y. S. Park, J. W. Choi, and J. S. Lee, “Dependence of carrier localization in InGa<sub>N</sub>/Ga<sub>N</sub> multiple-quantum wells on well thickness”, *Applied physics letters* **89**, 253120 (2006).
- <sup>30</sup>Y.-H. Cho, G. H. Gainer, a. J. Fischer, J. J. Song, S. Keller, U. K. Mishra, and S. P. DenBaars, “S-shaped temperature-dependent emission shift and carrier dynamics in In-GaN/GaN multiple quantum wells”, *Applied physics letters* **73**, 1370 (1998).
- <sup>31</sup>Q. Wang, J. Bai, Y. P. Gong, and T. Wang, “Influence of strain relaxation on the optical properties of InGa<sub>N</sub>/Ga<sub>N</sub> multiple quantum well nanorods”, *Journal of physics d: applied physics* **44**, 395102 (2011).
- <sup>32</sup>H. Kitagawa, M. Fujita, T. Suto, T. Asano, and S. Noda, “Green GaInN photonic-crystal light-emitting diodes with small surface recombination effect”, *Applied physics letters* **98**, 181104 (2011).

- <sup>33</sup>M. Athanasiou, T. K. Kim, B. Liu, R. Smith, and T. Wang, “Fabrication of two-dimensional InGaN/GaN photonic crystal structure using a modified nanosphere lithography technique”, *Applied physics letters* **102**, 191108 (2013).
- <sup>34</sup>C. W. Tang and S. a. VanSlyke, “Organic electroluminescent diodes”, *Applied physics letters* **51**, 913 (1987).
- <sup>35</sup>J. H. Burroughes, D. D. C. Bradley, A. R. Brown, R. N. Marks, K. Mackay, R. H. Friend, P. L. Burns, and A. B. Holmes, “Light-emitting diodes based on conjugated polymers”, *Nature* **347**, 539–541 (1990).
- <sup>36</sup>S. Guha, R. A. Haight, N. A. Bojarczuk, and D. W. Kisker, “Hybrid organic-inorganic semiconductor-based light-emitting diodes”, *Journal of applied physics* **82**, 4126 (1997).
- <sup>37</sup>G. Heliotis, P. N. Stavrinou, D. D. C. Bradley, E. Gu, C. Griffin, C. W. Jeon, and M. D. Dawson, “Spectral conversion of InGaN ultraviolet microarray light-emitting diodes using fluorene-based red-, green-, blue-, and white-light-emitting polymer overlayer films”, *Applied physics letters* **87**, 103505 (2005).
- <sup>38</sup>D. Basko, G. La Rocca, F. Bassani, and V. Agranovich, “Förster energy transfer from a semiconductor quantum well to an organic material overlayer”, *The european physical journal b* **8**, 353–362 (1999).
- <sup>39</sup>D. Andrews, “A unified theory of radiative and radiationless molecular energy transfer”, *Chemical physics* **135**, 195–201 (1989).
- <sup>40</sup>M. Achermann, M. a. Petruska, S. Kos, D. L. Smith, D. D. Koleske, and V. I. Klimov, “Energy-transfer pumping of semiconductor nanocrystals using an epitaxial quantum well.”, *Nature* **429**, 642–6 (2004).
- <sup>41</sup>G. Heliotis, G. Itskos, R. Murray, M. Dawson, I. Watson, and D. Bradley, “Hybrid Inorganic/Organic Semiconductor Heterostructures with Efficient Non-Radiative Energy Transfer”, *Advanced materials* **18**, 334–338 (2006).
- <sup>42</sup>S. Chanyawadee, P. G. Lagoudakis, R. T. Harley, M. D. B. Charlton, D. V. Talapin, H. W. Huang, and C.-H. Lin, “Increased color-conversion efficiency in hybrid light-emitting diodes utilizing non-radiative energy transfer.”, *Advanced materials (deerfield beach, fla.)* **22**, 602–6 (2010).
- <sup>43</sup>S. Nizamoglu, B. Guzelturk, D.-W. Jeon, I.-H. Lee, and H. V. Demir, “Efficient nonradiative energy transfer from InGaN/GaN nanopillars to CdSe/ZnS core/shell nanocrystals”, *Applied physics letters* **98**, 163108 (2011).
- <sup>44</sup>J. Hill, S. Heriot, O. Worsfold, T. Richardson, A. Fox, and D. Bradley, “Controlled Förster energy transfer in emissive polymer Langmuir-Blodgett structures”, *Physical review b* **69**, 041303 (2004).
- <sup>45</sup>J. Rindermann, G. Pozina, B. Monemar, L. Hultman, H. Amano, and P. Lagoudakis, “Dependence of Resonance Energy Transfer on Exciton Dimensionality”, *Physical review letters* **107**, 236805 (2011).

- <sup>46</sup>S. Blumstengel, S. Sadofev, C. Xu, J. Puls, and F. Henneberger, “Converting Wannier into Frenkel Excitons in an Inorganic/Organic Hybrid Semiconductor Nanostructure”, *Physical review letters* **97**, 237401 (2006).
- <sup>47</sup>V. M. Agranovich, Y. N. Gartstein, and M. Litinskaya, “Hybrid resonant organic-inorganic nanostructures for optoelectronic applications.”, *Chemical reviews* **111**, 5179–214 (2011).

---

## Experimental Techniques

---

### 3.1 Optical Characterization

Optical characterization techniques allow for properties of a material to be measured non-destructively. Many material properties can be determined and investigated using optical techniques such as the bandgap, band offset, alloy composition and impurity and defect presence [1].

#### 3.1.1 Photoluminescence

Photoluminescence (PL) involves the optical excitation of carriers in the material through the use of a light source with a photon energy higher than the bandgap of the material. In order to achieve high enough populations of excited carriers in the material lasers are used as excitation sources due to the high power density achievable with lasers. The discrete wavelength of a laser also allows photons of a specific energy to be delivered to the system. This can be useful when only a specific material in a sample is to be excited. For example, the GaN band edge is 363nm. A laser with a wavelength longer than this will pass through the GaN layer. When blue emitting (450nm) InGaN quantum well samples are used, a 375nm laser diode has been used to photo-excite carriers specifically only in the InGaN wells. In order to examine the emission properties of the sample a spectrometer must be used to analyse the emitted light.

A schematic of the photoluminescence system used in this work is shown in Figure 3.3. A 375nm laser diode has been used to excite the blue emitting InGaN quantum well samples used as the basis of white emitting structures. Samples are held in an closed loop cryogen optical cryostat, this allows the sample temperature to be varied between 12K and 325K. As discussed in section 2.2.5, this allows the thermal energy of carriers to be varied while examining the PL emission of the sample to determine localization

related effects. The emission from the sample is collected and focused by 2" UV fused silica lens into a 320mm focal length monochromator (Horiba iHR320). The monochromator uses blazed holographic gratings with groove densities of 1200lines/mm and centre wavelengths of 330nm and 500nm giving a dispersion of 1.34nm/mm at the exist slit of the monochromator. The dispersed emission signal is detected by a cooled Hamamatsu GaAs photomultiplier tube(PMT). To collect a spectrum the exit slit of the monochromator is set to allow a particular bandwidth of the dispersed light to fall on the PMT. The monochromator grating is then scanned through the desired range and an intensity reading from the PMT taken at specific predetermined wavelength steps.

### 3.1.2 Photoluminescence Excitation

Where photoluminescence is a measurement of the intensity of emission from a sample as a function of emission wavelength, photoluminescence excitation spectroscopy is the measuring of luminescence intensity of a sample as a function of excitation wavelength. In this case the PL emission intensity of a fixed wavelength is used by fixing the position of the detector monochromator described for the PL measurements previously discussed. In order to achieve this, a tunable excitation source is required. For the GaN and InGaN materials system with emission wavelengths in the visible, the range of excitation wavelengths required is in the UV-vis range from around 250 – 500nm. It is currently difficult to achieve such a wide range of continuously tunable wavelengths using laser based systems, as a result the main practical implementation of PLE for III-nitrides involves the use of a broad band light source such as a XE arc lamp dispersed by a monochromator to select a discrete excitation wavelength.

In order to examine the materials properties of III-nitrides samples in more detail a PLE system was built. The detection system is based around the same system as the PL system described in the previous section. The sample is held in a closed loop He cryostat. Emission is collected by a UV-fused silica lens and focused by a second UV-fused silica lens into the detection monochromator. The same monochromator (Horiba iHR320) was used with the same cooled GaAs PMT. For use in the PLE configuration the detector monochromator is fixed at the emission peak of interest. The excitation source is a 450W xenon short arc lamp. This is passed through a 140mm monochromator (Horiba microHR) to disperse the excitation light. The bandwidth is selected by adjusting the exit slit of the monochromator. This is scanned through a wavelength range of interest and an intensity measurement made with the GaAs PMT on the detection monochromator at set intervals. The output intensity of the Xe lamp and the efficiency curve of the excitation monochromator grating are not flat as a function of wavelength. In order remove the system response from the measured PLE spectra a calibrated UV-enhanced Si photodiode was used. The excitation intensity is measured as a function of wavelength using the Si photodiode. This data is calibrated using the calibration data supplied with the photodiode. The spectrum can then be used to correct the PLE spectra measured over the same

range.

The PLE measurement technique does not directly measure the absorption of a sample, but if the relaxation of injected carrier to the band edge is significantly faster than the radiative recombination rate of carriers between band edges then the PLE spectrum can be analogous to absorption in some situations. As it is a measure of photoluminescence intensity, only radiative transitions can be examined. This can be particularly useful when a sample of interest is on a non-transparent substrate. For example a PLE spectrum of an InGaN layer or InGaN quantum wells grown on a sapphire substrate with a GaN buffer layer can be measured as the excitation light only has to pass through the thin top GaN barrier to excite the InGaN, absorption measurements however would not be possible below the GaN bandedge as the GaN buffer layer would fully absorb the transmitted light.

Using PLE measurements to determine the absorption edge of a material can be useful as the difference between the absorption and emission peaks (Stokes like shift) can yield information related to the quality of a sample strain of polar quantum well structures [2]. As quantum well widths are increased the piezoelectric field is also increased, this increase in field strength increases the effect of QCSE leading to a larger shift between absorption and emission peaks. An example of this is shown in Figure 3.2, where three InGaN/GaN MQW samples with differing quantum growth times and therefore different quantum well widths show increasing stokes like shift with increasing well width. It is also possible to resolve excitonic features in PLE spectra as splitting in the valence band or excited state transitions ( $n= 2$  etc.) will be shown as peaks in PL intensity when the excitation energy matches the transition energy [3].

### 3.1.3 Time Resolved Photoluminescence

In order to examine the recombination dynamics of carriers in a material, the photoluminescence can be measured as a function of time, this is time resolved photoluminescence (TRPL). This is particularly useful as the recombination dynamics can be directly probed. In the previous chapter the recombination mechanisms in a quantum well were discussed. Using TRPL it is possible to measure the lifetime  $\tau_{pl}$  from Equation 3.1 and thus the radiative and non-radiative lifetimes. In order to achieve this, the intensity of PL emission from a sample is measured as a function of time after a pulsed excitation of carriers in the material is removed.

$$\frac{1}{\tau_{pl}} = \frac{1}{\tau_r} + \frac{1}{\tau_{nr}} \quad (3.1)$$

$$I(t) = Ae^{-\frac{t}{\tau}} \quad (3.2)$$

The decay lifetime comes from standard exponential decay, where A is a constant, shown in Equation 3.2. For simple systems the photoluminescence decay may be de-



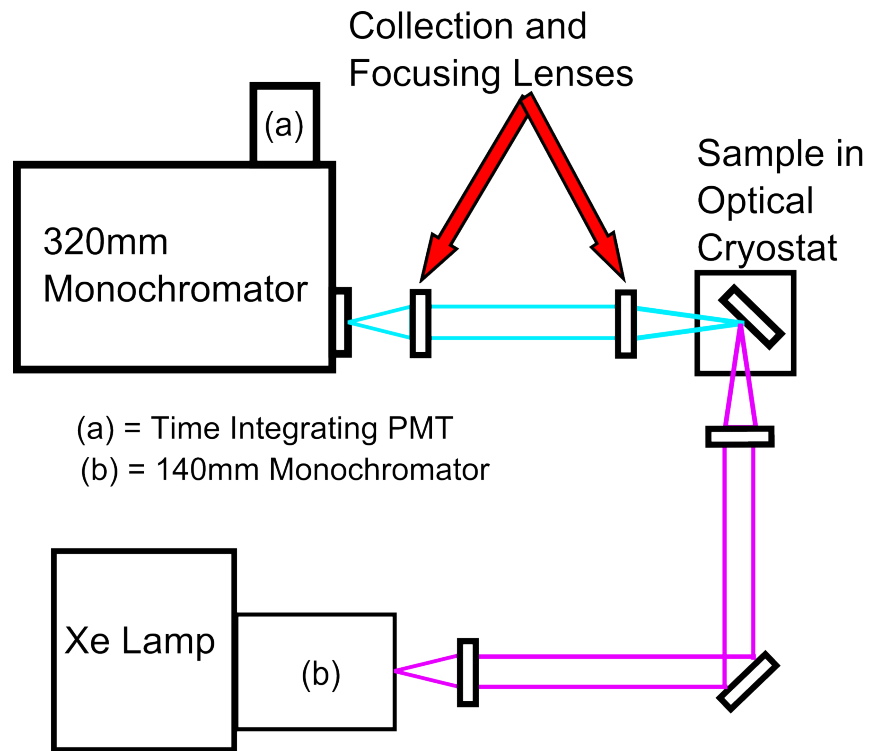


Figure 3.1: A schematic diagram of the photoluminescence excitation system built for this work

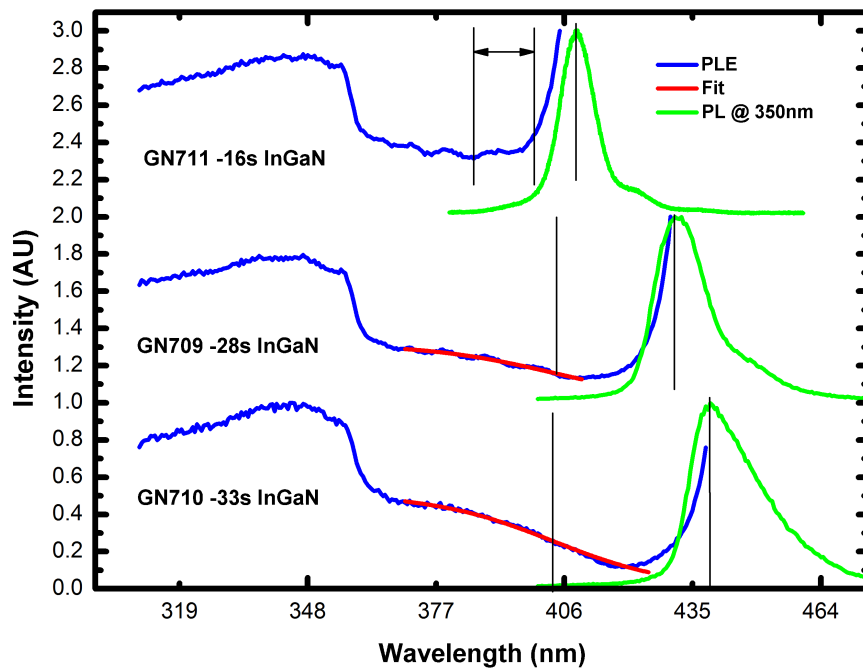


Figure 3.2: Low temperature PL and PLE of three InGaN MQW samples with different quantum well growth times and therefore different quantum well widths. A sigmoidal fit to the InGaN absorption edge is shown for the two samples with larger Stokes like shift

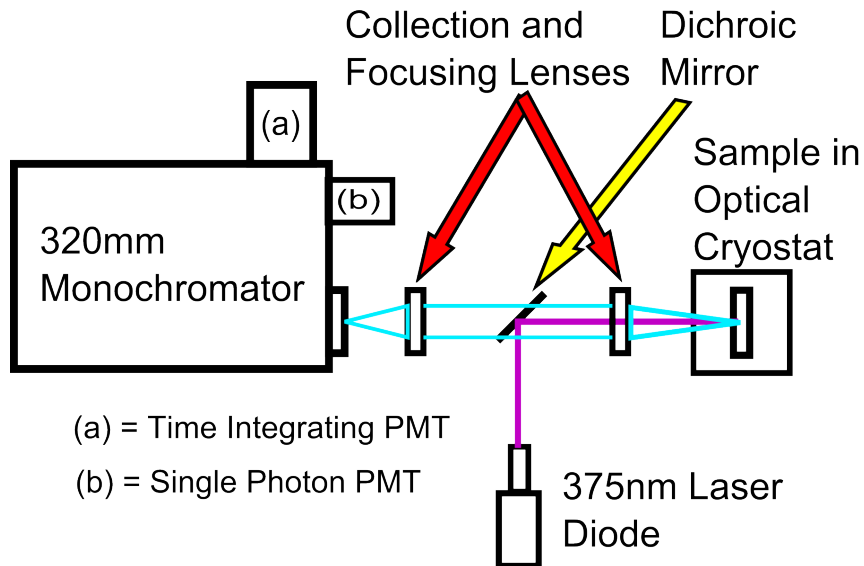


Figure 3.3: A schematic diagram of the time correlated single photon counting system set up for this work

scribed by a single exponential decay function. For nitride systems mono-exponential decays are very rarely seen. The exact nature of the decay profile of a nitride material can vary significantly depending on the material properties. For the most commonly studied standard polar InGaN/GaN quantum well structures, typical decay curves are distinctly non-monoexponential as seen in Figure 3.4. The causes for the non-exponential nature of the decay are most commonly linked to inhomogeneity in the sample. In order to extract decay lifetime parameters from the TRPL of such samples other models have been proposed. One common method is to use a representative lifetime such as the time taken for the PL intensity to decay to  $1/10$  or  $1/e$  of the initial value [4]. Another approach uses a bi-exponential function, this is the sum of two separate exponential decays, shown in Equation 3.3. This model has been used to describe the decay of InGaN/GaN quantum wells, where the two decays correspond to the fast decay( $\tau_1$ ) of free excitons and the slower decay( $\tau_2$ ) of localized excitons [5]. Other decay models are also used, for non-polar InGaN/GaN quantum wells, the decay profile is significantly different due to the lack of QCSE and the increased overlap of electron and hole wavefunctions. The stretched exponential function has been used in other material systems to describe decay in disordered systems [6], where the constant  $\beta$  describes the distribution of states in a disordered system. When applied to non-polar InGaN/GaN MQWs the fast, exponential decay describes free exciton recombination and the slower, stretched exponential relates to relaxation in the disordered localized states [7]. This model is a phenomenological model and fits well to most non-polar InGaN quantum well samples, the exact physical origin of the decay profile is still not fully understood. For most purposes it is only required to measure a relative decay lifetime, to compare between samples and examine how the decay profile changes with temperature of excitation power density. For such binary decay models it is often the case that the free-exciton recombination dominates the

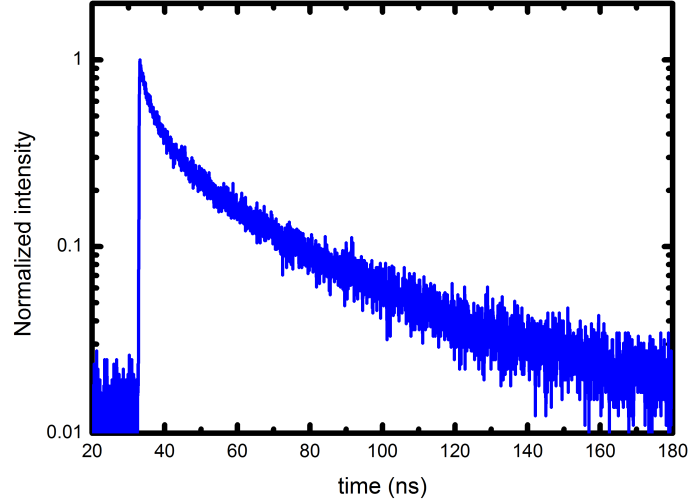


Figure 3.4: Typical decay profile for an InGaN MQW sample, plotted in log scale, the non-mono-exponential shape is apparent

decay to the extent that this can be taken as the representative decay lifetime [8].

$$I(t) = A_1 e^{-\frac{t}{\tau_1}} + A_2 e^{-\frac{t}{\tau_2}} \quad (3.3)$$

$$I(t) = A_1 e^{-\frac{t}{\tau_1}} + A_2 e^{(-\frac{t}{\tau_2})^\beta} \quad (3.4)$$

### Time Correlated Single Photon Counting

In order to measure decay lifetimes on the scale of tens of picoseconds to tens of nanoseconds high speed measurement techniques are required. The system set-up for this work uses the time correlated single photon counting method TCSPC. The basis of this process is to count single photons emitted from the sample after an excitation event and correlate the time of measurement with the end of the excitation pulse. As opposed to real time measurement techniques such as those using streak cameras that require the ability to collect a large number of photons in a burst following an excitation laser pulse. TCSPC measurements can be made with much more simple equipment as the decay profile is made up of many single photon measurements.

The measurement process starts with an excitation laser pulse. Synchronously with this, a trigger signal (SYNC) is sent to counting electronics, the laser pulse excites carriers in the sample and photons are emitted. The emitted photons are collected and focused onto a single photon detector, when a photon triggers the detector a signal is sent to the timing electronics and the time between laser SYNC signal and single photon detection trigger is logged in memory. The process is then repeated until a statistically significant

number of photon pulses and timing data have been built up to produce a histogram of intensity as a function of time. This histogram of many single photon events matches the real-time distribution of intensity as a function of time. For this technique to work, it is prerequisite that the rate of detection of single photons is at maximum between 1-5% of the laser pulse rate. This ensures that the probability of more than one photon arriving at the detector between excitation laser pulses is sufficiently small for multi-photon events to be negligible. The effect of multiple photons arriving at the detector between laser pulses is termed photon pileup. After detection of a photon the detector is unable to detect another photon for a period of time known as deadtime. If another photon arrives at the detector during this time it will not be logged. When photon pileup occurs, it is more likely that the first photon arriving at the detector will trigger it and the later photons are missed. This results in skewing the histogram in favour of early arriver photons giving the impression of a faster decay rate.

The system used works in a modified TCSPC mode, reversed start stop. In this mode of operation, a photon arriving at the detector triggers a pulse. A constant fraction discriminator (CFD) reduces the timing jitter of trigger signals in the system. The CFD output pulse triggers the time to amplitude converter (TAC) in the timing electronics. The next laser pulse and corresponding SYNC signal are received at a later time. This SYNC signal stops the TAC and an analogue to digital converter (ADC) converts the TAC voltage to a digital timing value to be stored in memory. The laser pulse repetition is periodic, allowing the real time delay between laser pulse and CFD to be easily determined. This detection mode allows faster laser repetition rates to be used as the TAC is only started when a photon triggers the detector as opposed to with each laser pulse [9].

The system used is shown in Figure 3.3. A 375nm laser diode from Edinburgh instruments is used as excitation source, this Laser has built in picosecond laser diode driver and emits pulses with a FWHM of 83ps. The laser repetition rate can be set at discrete repetition rates from 20MHz down to 20KHz. The diode driver also provides the SYNC output. The detector used is built around a Hamamatsu hybrid PMT tube that has a single photon response FWHM of 120ps. The detector produced by Becker & Hickl is housed with built in high voltage supplies preamplifier and CFD. The timing electronics are integrated on an SPC130 TCSPC card from Becker & Hickl, taking both CFD and SYNC inputs.

The instrument response function (IRF) is a mixture of all of the timing jitter in each component and can be measured by detecting scattered laser light with the system. Using the monochromator shown in the schematic the detection wavelength is set to the laser peak and an IRF pulse of 150ps FWHM is measured. The measured decay trace of a sample is a convolution of the true decay and the IRF. Removing the IRF by numerical deconvolution is not normally achievable and the solution is to use an iterative reconvolution fitting method. Fluofit software from PicoQuant was used to fit decay traces in this work. A model is chosen such as the biexponential function in Equation 3.3. The decay

curve and IRF are loaded into the software and then initial values are set. The model is then plotted and convoluted with the IRF, this is then plotted against the measured data. An iterative Levenberg-Marquardt fitting is then carried out, setting new parameters and re-convoluting each iteration.

### 3.1.4 Confocal Microscopy

The principle of confocal microscopy is that the excitation light and emission are focused along the same axis. The emission is then focused through a pin hole aperture in order to reject out of focal plane light. This generates an excitation spot (in this case, a 375nm laser diode) focused to a minimal diameter dependent on the magnification, numerical aperture and quality of the objective lens. The emission from the sample is collected by the same objective and then focused onto a pinhole aperture. When the optical elements are aligned such that the emission and excitation share identical paths and the focus of the emission adjusted to produce an image of the laser spot on the pinhole. Any out of focal plane emission or scattered light is rejected[10]. A Witec confocal microscope system (shown in Figure) was used with a 375nm laser diode as excitation source with a Princeton instruments monochromator and an Andor CCD to analyse the emission. This allows for photoluminescence measurements to be made of InGaN quantum well samples with very high spatial resolution. The lateral resolution of a confocal microscope is defined as [10]:

$$FWHM_{lateral} = 0.37 \frac{\lambda^*}{NA} \quad (3.5)$$

Where NA is the numerical aperture of the microscope objective lens, in this case 0.95. And:

$$\lambda^* \approx \sqrt{2} \frac{\lambda_{emission} \lambda_{excitation}}{\sqrt{\lambda_{emission}^2 + \lambda_{excitation}^2}} \quad (3.6)$$

For an excitation wavelength of 375nm and an emission wavelength of 450nm, this gives an approximate lateral resolution of 159nm. The Witec confocal system used has a piezo-electric scan stage that allows the sample to be moved with a 2nm resolution. It is possible to measure a photoluminescence spectrum at a point, move the stage and take a further spectral measurement. In this manner it is possible to build PL maps of a sample with resolution on the order of 160nm.

### 3.1.5 X-ray Diffraction

X-ray diffraction (XRD) is an extremely powerful tool in the characterization of crystal structures. As the wavelength of x-rays is on the order of the lattice spacing in crystal structures ( $\approx 0.1\text{nm}$ ), x-rays may be diffracted by crystal lattices. X-rays reflecting from different atomic planes in a material will be offset by the lattice spacing reaching a detector with a shifted phase, causing interference. The interference is governed by Bragg's



Figure 3.5: The Witec confocal system, with Princeton instruments monochromator and Andor CCD.

law.

$$2d \sin(\theta) = n\lambda \quad (3.7)$$

Where the separation between atomic planes is  $d$ . This allows information about the lattice constants of a crystal to be obtained by examining the angular interference patterns of diffracted x-rays from a crystal surface. In an XRD system, x-rays are generated and monochromated to select a single wavelength close to the lattice spacing. By rotating a sample and x-ray detector in relation to the x-ray source the intensity of the diffracted x-rays patterns can be measured as a function of the angular position. A useful technique is  $\omega - 2\theta$  scanning, where the angle of diffracted x-rays ( $2\theta$ ) is scanned with the detector and the rotation of the incident beam to the sample ( $\omega$ ) is scanned by rotating the sample [11]. This scan can yield the lattice constants of the material, and layer thickness in multi layer materials, through modelling of this data information regarding alloy composition can be extracted. Combining  $\omega - 2\theta$  scans at varying  $\omega$  values two dimensional maps of reciprocal space can be constructed. This allows the relative strain states of different layers to be compared.

## 3.2 Device Fabrication

### 3.2.1 Thin film Deposition Techniques

In the field of semiconductor device fabrication the ability to deposit thin films of materials onto semiconductor wafers after growth is integral to the creation of optoelectronic devices. Various deposition techniques are required to deposit controlled layers of metals and dielectric materials. In this work a variation of the common chemical vapour deposition (CVD) process was used to deposit thin films of dielectric materials silicon nitride and silicon dioxide. CVD processes in general rely on the chemical reaction of precursor

materials on a substrate resulting in the formation of the target material on the substrate surface. This process can be modified through the use of a radio frequency (RF) electric field to generate a plasma, ionizing the precursor gasses, increasing the reaction rate of the precursors, enabling some reactions that otherwise would not be energetically favourable. Plasma enhanced chemical vapour deposition (PECVD) allows films of silicon dioxide and silicon nitride to be deposited with the precursors of  $\text{SiH}_4$  and either  $\text{NO}_2$  or  $\text{NH}_3$  at substrate temperatures of typically  $300^\circ\text{C}$  but even at room temperature.

### **3.2.2 Dry Etching Techniques**

Etch techniques are required to selectively remove certain areas of an epi-wafer or thin film. Wet etching techniques are common in many semiconductor materials, with different etchants having crystallographically selective etch rates. In the III-nitrides material system, wet etchants are of relatively limited usefulness in device fabrication. Dry etch techniques using reactive gasses and/or ion bombardment are indispensable techniques. Typical techniques used are based around the principles of reactive ion etching (RIE). In RIE processing, etchant gasses are used with an RF electric field to generate a plasma (in this work  $\text{SF}_6$  and  $\text{CHF}_3$  to etch silicon dioxide). The plasma consists of reactive ions. These ions can react with the sample and remove material from the surface by reaction or by bombardment (sputtering). A variation of the RIE process, inductively coupled plasma reactive ion etching (ICP etching). An inductively coupled plasma is used in addition to the standard RIE process to generate a high plasma density with a magnetic field. The high plasma density allows fast etching rates, in this work ICP etching has been used to etch III-nitrides with a  $\text{Cl}_2$ , Ar gas mixture.

### **3.2.3 Organic Materials Deposition Techniques**

A wide range of organic materials are solution processable. This allows for a variety of easy and flexible deposition techniques to be used. The most common is spin coating, where an organic material is dissolved in a solvent and dropped onto a substrate which is rotated to discard excess solution and dry the solvent. Spin coating is widely used throughout the semiconductor industry as the ability to deposit flat films of materials. Many organic semiconductors are susceptible to oxygen related degradation, this will be covered in more details in Chapter 5. In order to avoid oxygen related degradation issues when spin coating light emitting polymer films, a glovebox has been used. The glove box environment was maintained in an anaerobic state with a forming gas atmosphere (95%  $\text{N}_2$ , 5%  $\text{H}_2$ ) using a palladium catalyst to reduce oxygen from the atmosphere, resulting in  $\text{O}_2$  levels of  $< 0.5\text{ppm}$ , the lower limit of the detector available. The glovebox used in this work is shown in Figure 3.6.

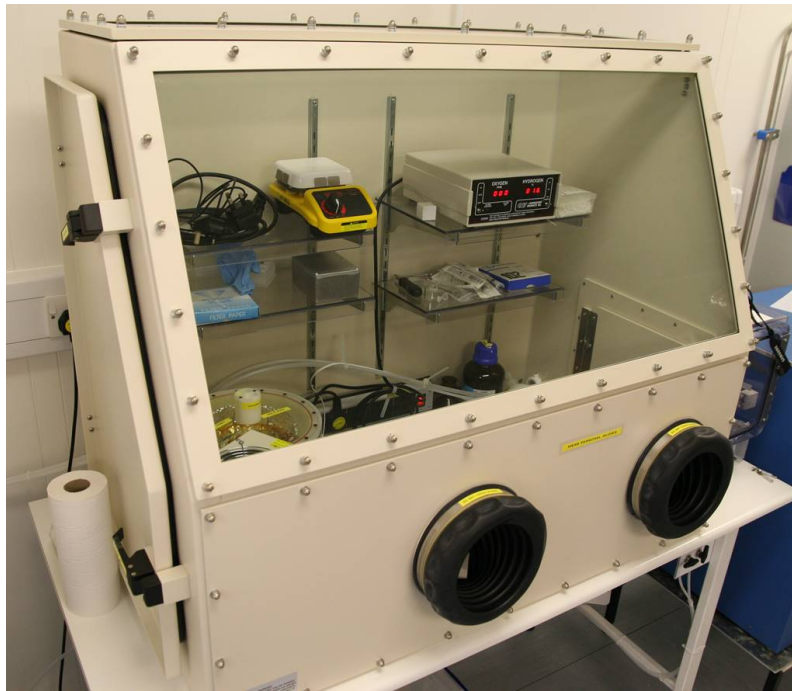


Figure 3.6: The glovebox used to spin coat light emitting polymer materials in an oxygen free atmosphere.

## References

- <sup>1</sup>S. Perkowitz, *Optical Characterization of Semiconductors: Infrared, Raman, and Photoluminescence Spectroscopy* (Academic Press, 1993), pages 1–6, 50–54, 61–92.
- <sup>2</sup>E. Berkowicz, D. Gershoni, G. Bahir, A. Abare, S. DenBaars, and L. Coldren, “Optical Spectroscopy of InGaN/GaN Quantum Wells”, *Physica status solidi (b)* **216**, 291–300 (1999).
- <sup>3</sup>T. J. Badcock, P. Dawson, M. J. Kappers, C. McAleese, J. L. Hollander, C. F. Johnston, D. V. Sridhara Rao, a. M. Sanchez, and C. J. Humphreys, “Optical polarization anisotropy of a-plane GaN/AlGaN multiple quantum well structures grown on r-plane sapphire substrates”, *Journal of applied physics* **105**, 123112 (2009).
- <sup>4</sup>J. A. Davidson, P. Dawson, T. Wang, T. Sugahara, J. W. Orton, and S. Sakai, “Photoluminescence studies of InGaN/GaN multi-quantum wells”, *Semiconductor science and technology* **15**, 497–505 (2000).
- <sup>5</sup>J. H. Na, R. a. Taylor, K. H. Lee, T. Wang, A. Tahraoui, P. Parbrook, a. M. Fox, S. N. Yi, Y. S. Park, J. W. Choi, and J. S. Lee, “Dependence of carrier localization in InGaN/GaN multiple-quantum wells on well thickness”, *Applied physics letters* **89**, 253120 (2006).
- <sup>6</sup>X. Chen, B. Henderson, and K. P. O Donnell, “Luminescence decay in disordered low-dimensional semiconductors”, *Applied physics letters* **60**, 2672 (1992).
- <sup>7</sup>Y. Sun, O. Brandt, S. Cronenberg, S. Dhar, H. Grahn, K. Ploog, P. Waltereit, and J. Speck, “Nonpolar In<sub>x</sub>Ga<sub>1-x</sub>N/GaN(11-00) multiple quantum wells grown on  $\gamma$ -LiAlO<sub>2</sub>(100) by plasma-assisted molecular-beam epitaxy”, *Physical review b* **67**, 041306 (2003).



- <sup>8</sup>T. S. Ko, T. C. Lu, T. C. Wang, J. R. Chen, R. C. Gao, M. H. Lo, H. C. Kuo, S. C. Wang, and J. L. Shen, “Optical study of a-plane InGaN/GaN multiple quantum wells with different well widths grown by metal-organic chemical vapor deposition”, *Journal of applied physics* **104**, 093106 (2008).
- <sup>9</sup>W. Becker, *The bh TCSPC handbook*, 4th (2008).
- <sup>10</sup>S. Wilhelm, B. Gröbler, M. Gluch, and H. Heinz, *Confocal laser scanning microscopy principles*, technical report (ZEISS Jena).
- <sup>11</sup>M. A. Moram and M. E. Vickers, “X-ray diffraction of III-nitrides”, *Reports on progress in physics* **72**, 036502 (2009).



---

### Self Assembled InGaN/GaN MQW Nanorod Arrays

---

Nano structured InGaN MQWs are currently a significant focus of research due to the benefits that they can offer over conventional planar structures. These reasons can pertain to the recombination dynamics of carriers in the MQW structures ranging from strain relaxation to confinement of excitons or be related to optical effects such as waveguides or phonic crystals. An area of significant interest is the use of post growth, top-down etching processes. The area of III-nitride semiconductor research has long been driven by the potential commercialization of the technologies and the use of simple post growth techniques allows for potentially commercializable technologies to be developed.

There are many different motivations for the study on InGaN/GaN MQW nanorods. Most centre on the enhancement of the optical performance optoelectronic devices. The reasons for reported mechanisms of enhancement vary over a wide range. One of the most significant benefits of the fabrication of nanorod arrays using c-plane InGaN/GaN MQW structures is the potential to relax the lattice mismatch induced strain in the InGaN quantum wells, reducing the associated piezoelectric fields and therefore increasing the internal quantum efficiency. As such, strain relaxation has been a focus of numerous studies using simulation and experimental techniques to calculate and characterize the relaxation of strain in InGaN/GaN MQW nanorod arrays. Single quantum well structures were used by Kawakami et al to examine strain relaxation in InGaN micropillars using micropillars of different diameters fabricated by a post growth etching technique using an electron beam lithography generated etch mask[1]. Micropillars containing an InGaN single quantum well were fabricated with diameters of 2, 1 and  $0.5\mu\text{m}$ , a blue-shift in peak photoluminescence was observed, which increased with decreasing micropillar diameter. This blueshift was found to be caused by relaxation of the strain in the InGaN quantum well, leading to reduced piezoelectric field and therefore a reduction in QCSE. The phenomenon of strain relaxation has been observed by using either nanorods[2–4] or other

nanostructures including nanoholes[5] and nanoporous[6] structures. Other properties of nanorod structures have been attributed to features such as surface states. Chan et al. observed the recombination dynamics of a single microrod at 4.2K and found long decay components at low temperature which were assigned to being related to surface traps[7]. Jiang et al. used a self assembly technique to fabricate InGaN GaN MQW nanorod arrays and examined the excitonic dynamics by time resolved PL at different power densities[8]. It was reported that the recombination rate was increased in the nanorod etched samples, with, unlike other self assembly nanorod reports[2, 3, 9–12], a decrease in time integrated PL intensity. This was attributed to a change in exciton diffusion caused by nanorod fabrication and the effects of surface states and strain relaxation.

Although InGaN/GaN MQW nanorod structures have been a focus of research for several years, the understanding on the dominant changes to recombination and optical properties of these structures is not fully developed. Results from various groups appear to show different effects in InGaN/GaN QW nanorods with PL intensities increasing [2] and decreasing [8], with causes ranging from strain relaxation [2] or surface states [7]. Due to the importance of III-nanorod structures, this lack of current understanding of the nature of QWs in nanorods requires further research and investigation. In this chapter work is presented that has been carried out to better understand InGaN/GaN MQW nanorods, and the benefits of using these structures.

## 4.1 InGaN/GaN Multiple Quantum Well Structures

In order to examine the effects of post growth fabrication of planar InGaN/GaN MQW structures into nanorod arrays on the optical properties of the InGaN MQWs, a series of visible emitting InGaN/GaN MQWs were used. All samples used here were grown on (0001) sapphire substrates grown by our high temperature AlN buffer developed by our group using a low pressure MOCVD system, which has demonstrated superior crystal quality to that grown by using the conventional two-step growth method. For our sample growth, after the substrate is subjected to thermal cleaning in flowing H<sub>2</sub> as usual, an atomically flat AlN layer with a thickness of 500 nm was directly grown on a sapphire substrate at 1200°C under a V/III ratio of 40. A GaN layer is then grown using high pressure then low pressure growth conditions. The direct growth of high temperature AlN buffer layer results in an atomically flat surface with parallel atomic lattice steps, unlike the standard two-step growth discussed in Chapter 1. This is evidence of step flow growth mode, with two dimensional growth of the AlN film dominating, unlike the three dimension growth of the typical two-step process [13, 14]. This technique results in significant reductions in the defect density in the GaN layer grown on top of the AlN buffer due to termination of threading dislocations at V shaped pits at the AlN - GaN interface[15]. Figure 4.1 shows the typical surface morphology of the GaN layer grown by use of the AlN buffer growth technique, with typically low surface roughness rms

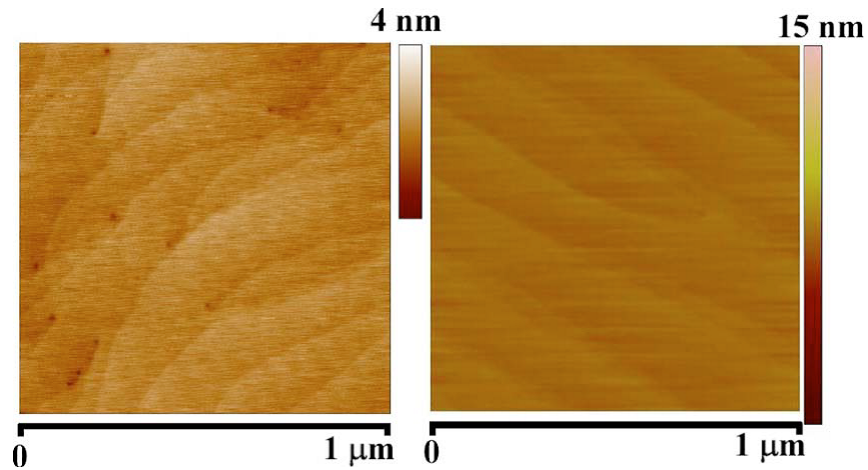


Figure 4.1: AFM images of the GaN surface for a conventional two-step growth (left) and the high temperature AlN buffer technique used in Sheffield (right).

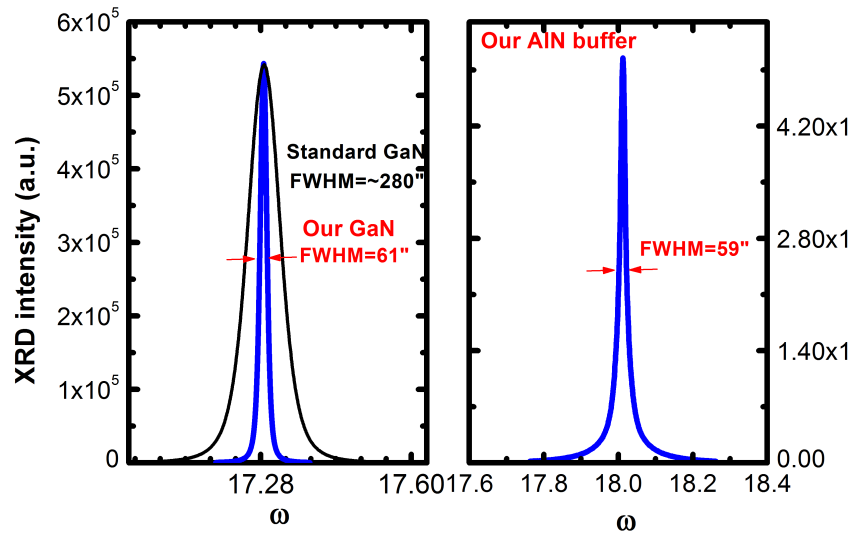


Figure 4.2: XRD rocking curves showing the increase in crystal quality of GaN films grown on the high temperature AlN buffer compared to GaN films grown using the standard two-step growth technique. The rocking curve of the high temperature AlN buffer layer is shown on the right.

values of 0.2nm. Further examining the AFM image indicates that the GaN on our HT AlN buffer does not show any dark points, typically observed on the AFM image of GaN grown using the classic two-step growth approach, which are due to the termination of screw dislocation on the surface. This means that the screw dislocation density of our sample is extremely low. In addition, the AFM image of our GaN also shows features with parallel and straight terraces, suggesting a typical step-flow growth mode, i.e., two dimensional layer-by-layer growth mode, which is different from the island growth mode of the conventional GaN [16]. For comparison, Figure 4.1 shows the typical AFM image of standard GaN grown using the classic two-step approach, where a number of dark points due to the termination of screw dislocation have been observed. Those results are consistent with the data of the (0002) XRD rocking curves, which are shown in Figure 4.2. The (0002) full width at half maximum FWHM of AlN is only 59 arc sec, which

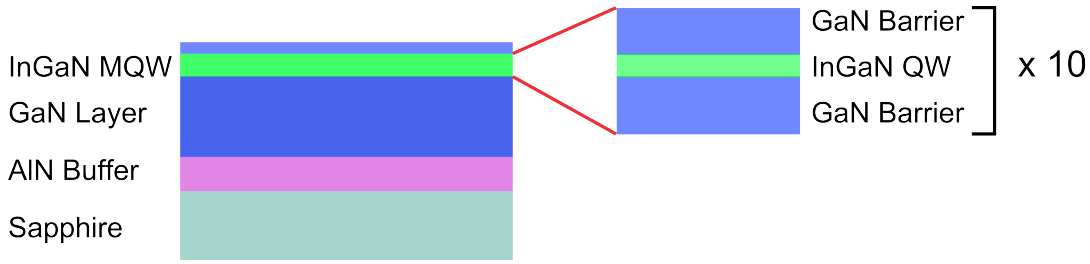


Figure 4.3: A schematic of the structure of the typical InGaN/GaN 10 quantum well sample grown in Sheffield used in this work (not to scale).

Material	Number of Repeats	InN mole fraction	Thickness
InGaN Quantum Well	10	16%	2nm
GaN Quantum Barrier	10	0%	9nm

Table 4.1: The parameters fit from Figure 4.4 showing quantum well and barrier width and composition

is much narrower than that of any AlN grown on sapphire so far [17]. The GaN on our HT AlN buffer also exhibits a narrow full width half maximum (FWHM) of (0002) XRD rocking curve, 61 arc sec, while the typical FWHM of the conventional GaN is around 280 arcsec. The much narrower (0002) FWHM of the former indicates a very low screw dislocation density in our GaN layer.

InGaN/GaN MQWs were grown on-top of the GaN buffer layers at single growth temperatures for the barrier and quantum well regions. The growth temperature was varied to control the indium mole fraction of the InGaN quantum wells, and therefore their emission wavelength.

### Structural Characterization

X-ray diffraction measurements have been made to characterize the InGaN/GaN MQW structures. As described in Chapter 3,  $\omega - 2\theta$  scans can be used to measure the composition and thickness of multi-layered epitaxial materials such as quantum wells. Figure 4.4 shows measured  $\omega - 2\theta$  scan for a blue emitting 10 quantum well InGaN/GaN wafer grown in Sheffield using the AlN buffer growth technique. A schematic of the MQW structure is shown in Figure 4.3. The  $\omega - 2\theta$  scan shows the zero order peaks of GaN, InGaN and the AlN buffer, higher order satellite peaks are also visible. Using the fitting described in Chapter 3, the thicknesses and compositions of the barriers and quantum wells have been calculated and are shown in Table 4.1. This blue emitting sample has an indium mole fraction of 16% with quantum well thickness of 2nm.

### Optical Characterization

The optical properties of the InGaN/GaN 10 period quantum well sample presented here have been investigated by photoluminescence using the system described in Chapter 3. The PL spectra of the 10 period quantum well sample with emission peak in the blue

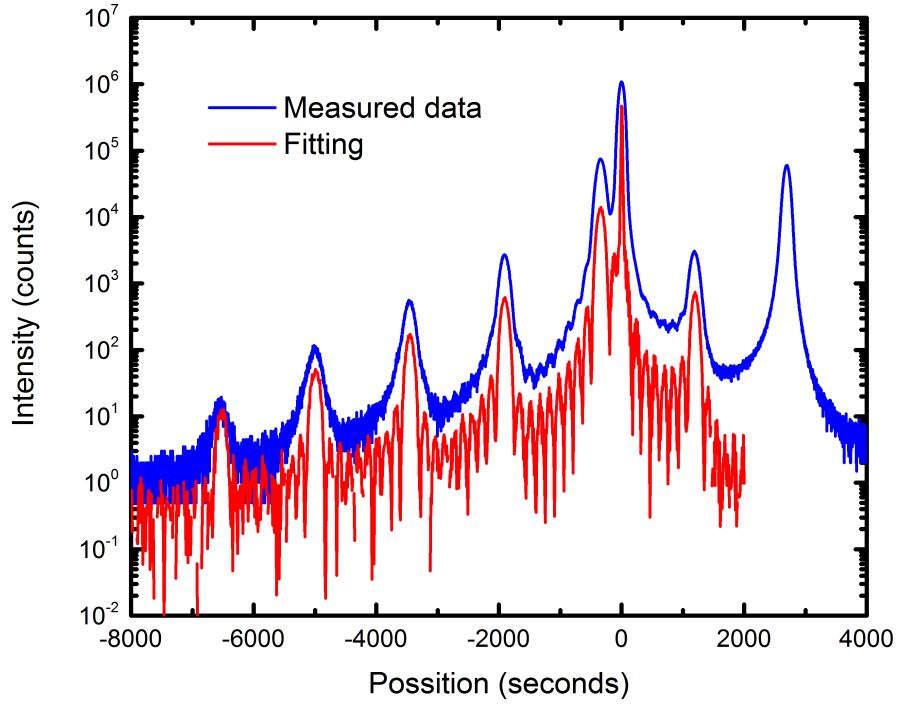


Figure 4.4: XRD  $\omega-2\theta$  scan data showing an as grown epi-wafer with 10 InGaN quantum wells with GaN barrier layers. The GaN, InGaN and AlN peaks as visible along with satellite peaks. The results of fitting are shown in Table 4.1

spectral region are presented in Figure 4.5. The excitation laser used was a  $375\text{nm}$  laser diode selectively exciting InGaN quantum wells. The sample temperature was varied from 12K to room temperature (300K). A clear difference in the shape of the PL peak is visible between low temperature and room temperature along with a peak emission wavelength shift of 8.6nm. At low temperatures, the thermal energy of excited carriers in the sample becomes insufficient to thermally excite carriers out of even shallow local potential minima. At such low temperatures (on the order of 10K) it is common to assume that the radiative recombination rate tends to zero, meaning recombination is entirely radiative (i.e. IQE= 100%) [18, 19]. With this assumption an estimate of IQE at a given temperature can be made using time integrated PL measurements referencing a sufficiently low sample temperature (in this case 12K).

$$\eta_{IQE}(T) = I(T)/I(12K) \quad (4.1)$$

Where  $I(T)$  is the integrated PL intensity at temperature  $T$ . Using this relationship, the IQE of this sample can be estimated to be 0.5% at room temperature. The reason for this low value is the low optical power density used to carry out the PL measurements. The excitation source was a 375nm laser diode operating in CW mode with a low output power. Under low excitation power densities, low densities of excited carriers are generated in the

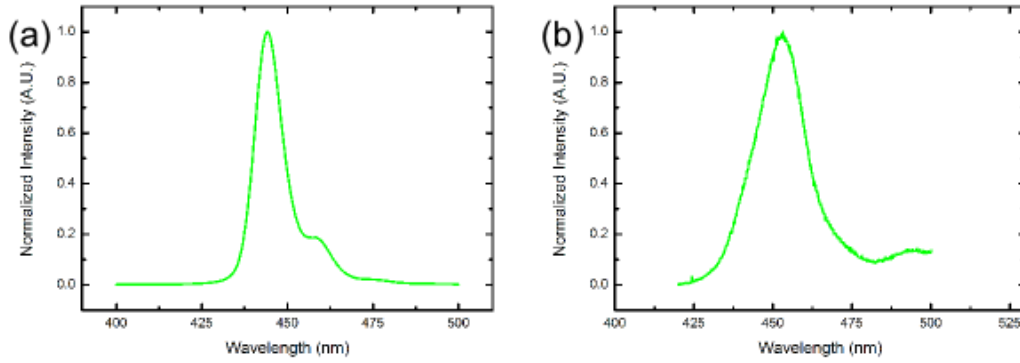


Figure 4.5: Photoluminescence measurements of the InGaN/GaN 10 quantum well as grown wafer (a) at a sample temperature of 12K with an peak emission wavelength of 452.8nm and (b) at room temperature with a peak emission wavelength of 444.2nm

MQW which does not screen QCSE, leading to low efficiency radiative recombination. Using the temperature dependence of the integrated PL intensity it is possible to extract information relating to the localization depth and thermal activation of the non-radiative processes in the MQW structure. Fitting a standard single term Arrhenius equation is not generally appropriate due to inhomogeneities of the material and the varied nature of the localization and non-radiative, PL quenching effects in InGaN [20, 21]. A reasonable fit can be obtained using a two term equation:

$$I(T) = \frac{I_{(T=10K)}}{(1 + C_1 \exp(-\frac{E_{a1}}{k_B T}) + C_2 \exp(-\frac{E_{a2}}{k_B T}))} \quad (4.2)$$

Where  $C_1$  and  $C_2$  are constants and  $E_{a1}$  and  $E_{a2}$  represent activation energies of quenching or non-radiative processes. Fitting the Arrhenius plot for this sample yeilds an  $E_{a1} = 15\text{meV}$  and  $E_{a2} = 57\text{meV}$ . The first activation energy corresponds to a temperature of 174K and related to the de-localization of excitons from localization centres in the InGaN, the physical nature of the second term is a matter of debate and likely to be a combination of features [21].

The temperature dependence of the PL spectrum also displays a clear shift in PL peak position with temperature. This can be seen more clearly in by plotting the peak PL emission energy as a function of temperature as in Figure4.7. The bandgap energy of a semiconductor material typically follows a temperature dependence described by the Varshini empirical equation [22].

$$E(T) = E_0 - \frac{\alpha T^2}{T + \beta} \quad (4.3)$$

Where  $E_0$  is the bandgap energy at  $T = 0\text{K}$ , and  $\alpha$  and  $\beta$  are Varshini fitting parameters. This behaviour describes a reduction in bandgap energy with temperature due to thermal expansion of the lattice, leading to an increase in lattice spacing. The temperature dependence of the PL peak emission of this InGaN/GaN sample deviates significantly



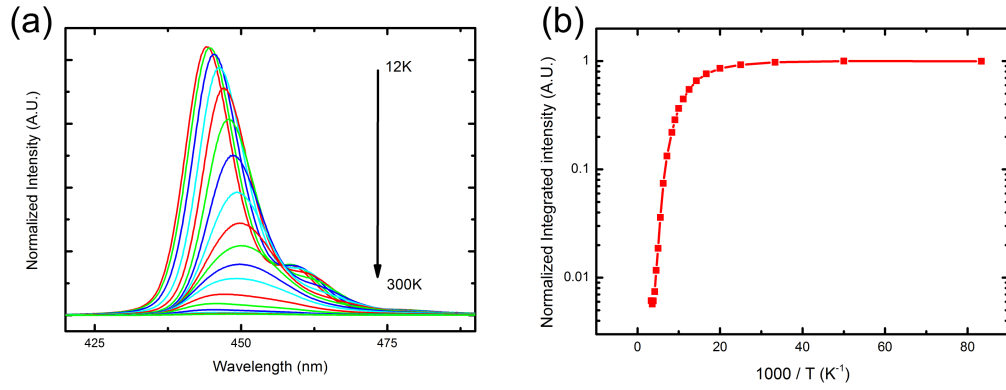


Figure 4.6: (a) Temperature dependent time integrated PL spectra with PL intensity decreasing with increasing temperature. (b) An Arrhenius plot of Integrated PL intensity against  $1000/T$  showing the reduction in PL intensity with increasing temperature

from this behaviour. This characteristic "S-shaped" temperature dependence has been attributed to competition between the standard temperature induced bandgap shrinkage and a thermally activated de-localization of carriers and redistribution between localized states [23, 24]. Due to inhomogeneity in the InGaN layer, at low temperature, excitons are quickly localized in local potential fluctuations within the material. With increasing thermal energy the localized excitons can escape their initial localization centres and move through the material before being captured by localization centres with larger potential depths leading to a red-shift in emission wavelength. As the thermal energy is increased further, de-localized excitons are able to migrate through the material and interact with non-radiative recombination centres. As non-radiative recombination increases and the recombination lifetime decreases, the possibility of excitons migrating to deeper localization centres decreases causing a blue-shift in emission energy. At higher thermal energy (in this case above  $T = 180\text{K}$ ), with de-localized excitons dominating, further thermal energy does not significantly reduce carrier lifetimes and the blue-shift behaviour is reduced. At temperatures higher than  $T = 180\text{K}$  the peak emission energy redshifts due to temperature induced band-gap shrinkage.

The carrier recombination dynamics were investigated by TRPL using the TCSPC technique described in Chapter 3 with a 375nm pulsed laser diode as excitation source to selectively excite carriers in the InGaN quantum wells. The PL decay traces measured at peak emission wavelength are presented at different sample temperatures in Figure 4.8. A clear trend is visible with the decay significantly longer at the lower sample temperatures and the trace becoming significantly shorter at higher sample temperatures. As this InGaN/GaN MQW sample is grown on c-plane sapphire and is therefore polar, QCSE is expected to cause the radiative recombination of carriers in the quantum well to be inhibited due to reduced electron-hole wavefunction overlap, leading to long carrier lifetimes. From Figure 4.8 it is clear that at 300K and 240K the carrier lifetime is considerably shorter than that at lower temperatures. Using that the measured photoluminescence life-

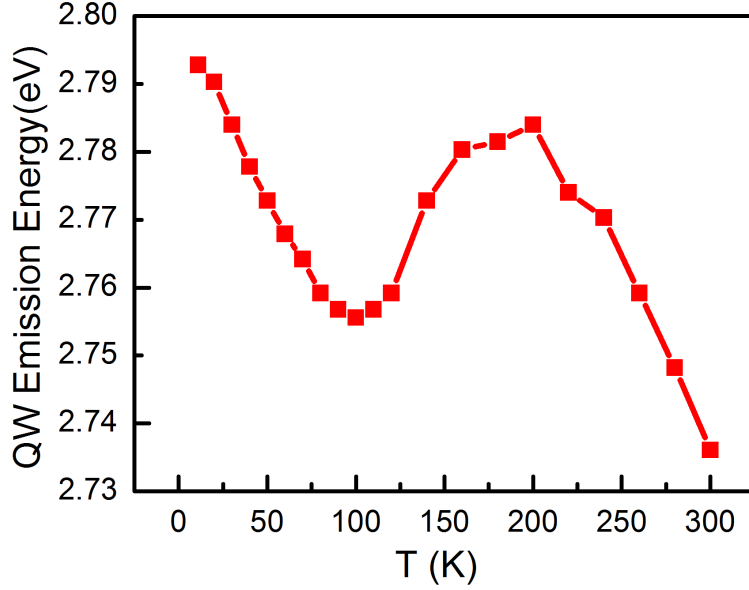


Figure 4.7: Temperature dependent peak emission energy for the 10 quantum well InGaN/GaN sample. A characteristic s-shift can be seen, with an initial red-shift from  $T = 12\text{K}$  to  $T = 90\text{K}$  followed by a blue-shift until  $T = 200\text{K}$  where emission red-shifts again until room temperature.

time is related to the radiative and non-radiative lifetimes by Equation 4.4 it is possible to understand this behaviour. By examining the low temperature PL decay trace and using the assumption that at 12K non-radiative recombination is effectively frozen out by carrier localization, the measured lifetime can be assumed to be equivalent to the radiative recombination lifetime. As the sample temperature is increased and excitons start to thermally de-localize, the non-radiative recombination centres are now accessible by these de-localized excitons and the non-radiative recombination lifetime begins to decrease. This leads to the PL decay becoming faster and the IQE becoming lower.

$$\frac{1}{\tau_{pl}} = \frac{1}{\tau_r} + \frac{1}{\tau_{nr}} \quad (4.4)$$

The TRPL traces presented in Figure 4.8 also highlight an interesting feature of recombination in InGaN/GaN MQWs. Although the traces are presented on a linear - log scale, the decays are clearly not pure exponential in profile. In ternary III-nitride alloys such as InGaN the non-exponential decay profile has been widely reported [25, 26]. This non-monoexponential decay is common in disordered material systems where multiple decay channels exist such as amorphous semiconductors [27]. The decay of InGaN quantum wells can be described by a bi-exponential decay, with a fast and slow decay component, where the component describes free exciton recombination and the slower decay components are caused by recombination from a range of localization centres and redistribution between localized states [25, 26, 28].

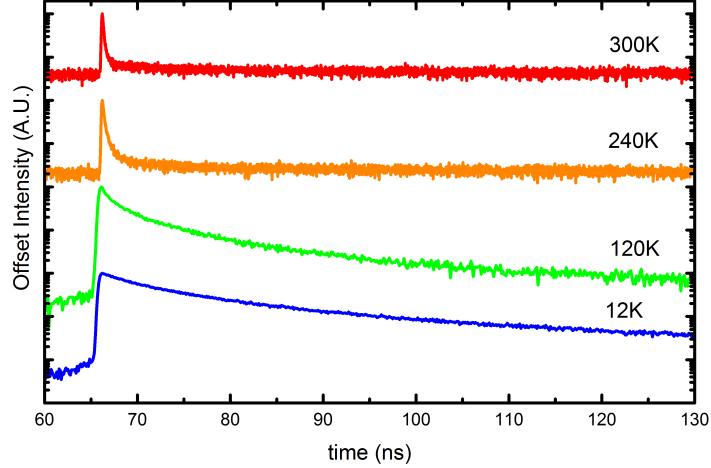


Figure 4.8: Time resolved photoluminescence data measured for the blue emitting InGaN 10 quantum well described previously. TRPL decay traces are plotted at different sample temperatures with a clear difference in behaviour from long, slow decay at low temperature (12K) to very fast decay at room temperature (300K).

$$I(t) = A_1 e^{-\frac{t}{\tau_1}} + A_2 e^{-\frac{t}{\tau_2}} \quad (4.5)$$

The TRPL data for the 10 period quantum well sample here was fitted with a bi-exponential decay described in Equation 4.5, where  $A_1$  and  $A_2$  are the decay coefficients of the two exponential decays with lifetimes  $\tau_1$  and  $\tau_2$ . The decay is not a single component monoexponential decay. The representative decay lifetime  $\tau_{pl}$  is not a single component, however, since the fast exponential component  $\tau_1$  tends to dominate over the slower decay component  $\tau_2$ , here,  $\tau_1$  is taken as  $\tau_{pl} = \tau_1$  for the sake of comparative analysis. Using the relationship shown in Equation 4.6, it is possible to extract the radiative and non-radiative lifetimes  $\tau_r$  and  $\tau_{nr}$  [29].

$$\eta_{IQE} = \frac{1}{1 + \frac{\tau_r}{\tau_{nr}}} \quad (4.6)$$

By substituting the temperature dependent time integrated PL from Equation 5.6 into Equation 4.6 and using Equations 4.7 the radiative and non-radiative lifetimes can be calculated from temperature dependent time resolved and time integrated PL. It should be noted that due to the assumptions made for Equation 5.6 and the assumption that  $\tau_1 = \tau_{pl}$ , these radiative and non-radiative values should not be taken as physically absolute, but can be useful for relative comparison in analysing the temperature dependent carrier recombination dynamics in InGaN QWs.

$$\tau_r = \frac{\tau_{pl}}{\eta_{IQE}} \quad \text{and} \quad \frac{1}{\tau_{nr}} = \frac{1}{\tau_{pl}} - \frac{1}{\tau_r} \quad (4.7)$$

Plotting the processed TRPL data for the blue emitting InGaN quantum well sample in

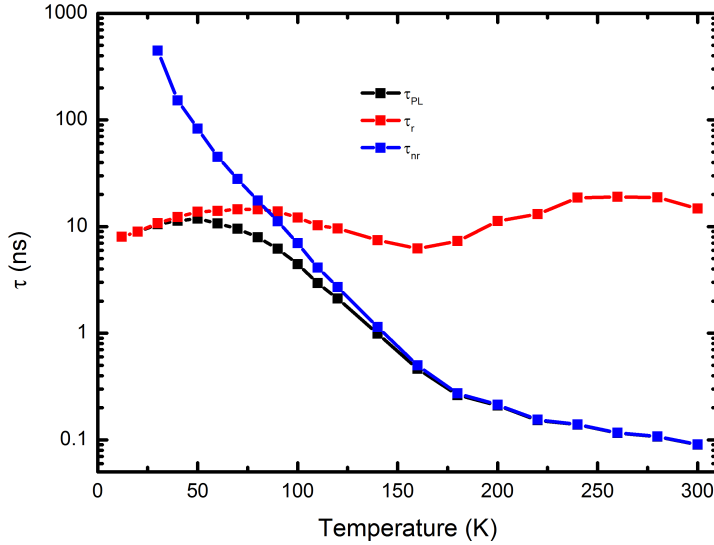


Figure 4.9: The PL decay, radiative and non-radiative lifetimes of the InGaN/GaN 10 quantum well sample are presented as a function of temperature.

Figure 4.9 shows the measured PL lifetime ( $\tau_{pl}$ ) initially increases from low temperature, at a maximum at  $T = 50\text{K}$  due to a combination of the thermalization of excitons in the quantum wells leading to longer radiative lifetimes [18, 30] and the redistribution to deeper localized states with longer emission wavelengths and therefore longer radiative lifetimes due to the polar nature of c-plane nitrides [24]. At a temperature of 85K, the radiative and non-radiative lifetimes become equivalent. With increasing temperature the dominant recombination pathways are now non-radiative due to the thermal activation of the non-radiative recombination centres. As non-radiative recombination dominates, thermalized increase in radiative lifetime is no-longer visible with increasing temperature. As the thermal energy increases and the majority of non-radiative recombination centres become activated, the decrease in the PL decay lifetime begins to slow towards room temperature.

## 4.2 Nanorod Fabrication

The approach taken to the fabrication of InGaN/GaN MQW nanorods in this work is a top-down, post growth dry etching based process relying on self assembled masks. Many techniques are used to fabricate nanostructures using III-nitride materials. The benefit of top-down, self assembly techniques is the relatively simple, scalable methods required make for technology that has practical applications for industry. There are many variations on top-down nanorod fabrication techniques reported using self assembled metal etch masks [4], nano-imprint lithography [7], electron beam lithography [1], and silica nanospheres [31]. The method used in this work is as follows: The InGaN/GaN MQW epiwafer on sapphire is taken and first cleaned with solvent baths to remove any potential

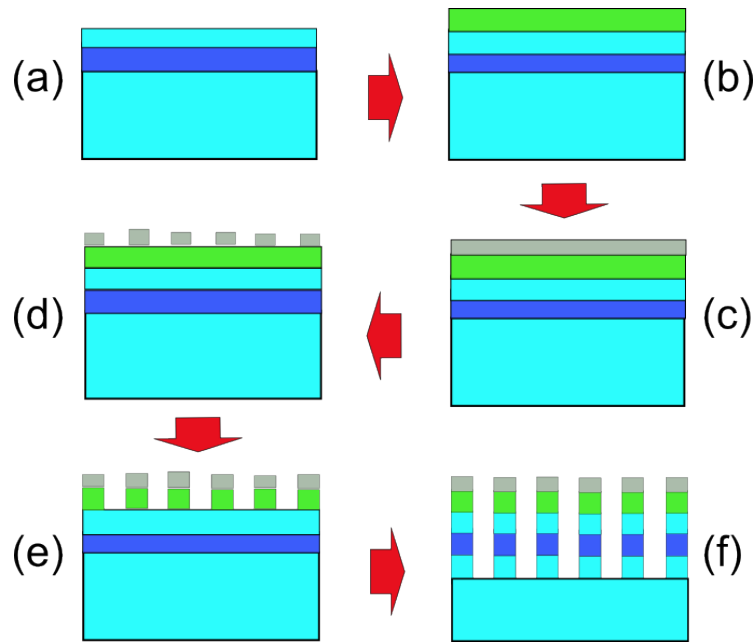


Figure 4.10: A schematic showing the nanorod fabrication procedure used

contaminants from the surface. The fabrication procedure is shown schematically in Figure 4.10. First, a layer of SiO<sub>2</sub> is then deposited on the epitaxial GaN surface by PECVD with a thickness of 200nm as shown in Figure 4.10 (b). The sample is then removed from the PECVD chamber and placed in an Edwards 306 thermal evaporator. A nickel film with a thickness of 10nm is then thermally evaporated on top of the SiO<sub>2</sub> at a pressure of ( $< 10^{-5}$ mbar) Figure 4.10 (c). A Rapid Thermal Annealer (RTA) is then used to anneal the sample at a temperature of 820°C in a flowing nitrogen atmosphere at atmospheric pressure for 60s. This annealing step causes the Ni film to coalesce and form self assembled nanoislands as shown in Figure 4.10 (d). These Ni nanoislands are used as an etch mask to form the nanorods. The sample is loaded into the chamber of a RIE system, to etch through the SiO<sub>2</sub> forming Ni capped SiO<sub>2</sub> nanorods on the surface of the GaN Figure 4.10 (e). The plasma etch conditions used for the RIE process are a gas mixture of CHF<sub>3</sub>:SF<sub>6</sub> with a flow rates of 30 : 10sccm respectively. The chamber pressure is set at 35mbar and an RF power of 75W is used to etch the SiO<sub>2</sub>. Finally an ICP RIE with Cl<sub>2</sub>Ar etch gasses is used to etch through the GaN layer (including InGaN MQWs) using the SiO<sub>2</sub> as an etch mask Figure 4.10 (f).

SEM images of the nanorod fabrication process can be seen in Figures 4.11 and 4.12. The SiO<sub>2</sub> mask is removed after dry etching by HF solution. The typical nanorod diameter is on average 220nm with a density of  $10^9/\text{cm}^2$ . It should also be noted that unlike some previous reports of self assembled nanorods, these nanorods have vertical sidewalls[7, 8] which will help reduce the effects of dry etch damage on the InGaN quantum wells. Before optical measurements are carried out, the nanorod arrays have potential etch damage removed by a surface treatment process.

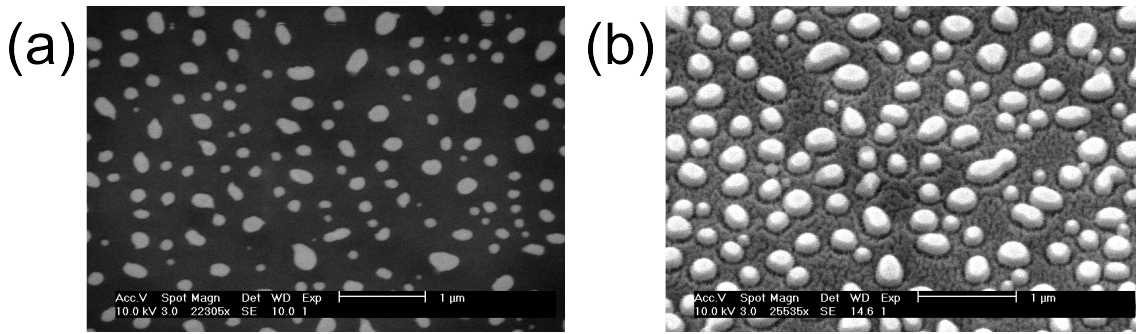


Figure 4.11: (a) SEM image of a self assembled array of Ni nanoislands after thermal annealing, for use as a dry etch mask. (b) SEM image of SiO<sub>2</sub> nanorods, after RIE etch

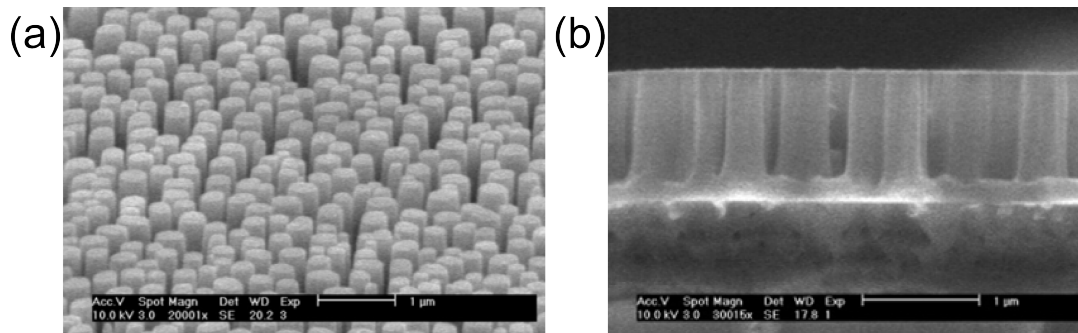


Figure 4.12: SEM images of the etched nanorods, with typical diameters of 220nm

### 4.3 Characterization of InGaN/GaN MQW Nanorods

In Figure 4.13 photoluminescence data are presented for a blue emitting InGaN/GaN 10 quantum well as-grown epiwafer and a sample from the same wafer after nanorod fabrication. This measurement was carried out at room temperature with excitation by a 375nm wavelength diode laser operating in continuous wave mode. The use of a 375nm laser diode with a corresponding photon energy of 3.31eV selectively generates carriers in the InGaN quantum wells only as 3.31eV is below the band edge of the GaN quantum barriers. A significant enhancement of the photoluminescence intensity of around six times is seen in the InGaN/GaN MQW nanorod sample compared to the planar wafer. A blue-shift in peak emission wavelength of 4nm is also visible for the nanorod structure. Strain relaxation has previously been reported as a potential cause for the enhancement in PL emission intensity and the blue shift in PL emission peak wavelength and as such has been investigated further.

#### Strain Relaxation

During the growth of InGaN/GaN quantum wells on c-plane substrates, the growth direction is along the polarization direction of the lattice (0001), the c-direction. For InGaN quantum wells, as the lattice constant of InN is larger than that of GaN, and in a typical quantum well with a thickness of 2 – 3nm (well below the critical thickness to allow strain relaxation) the quantum well is fully strained to the GaN barrier. The process

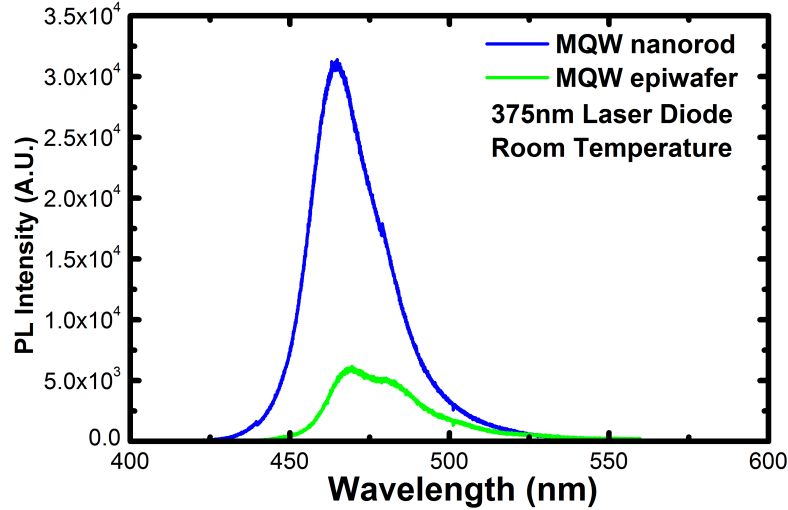


Figure 4.13: Photoluminescence of an InGaN MQW as-grown epiwafer compared with the sample after the fabrication of a nanorod array

of breaking the crystal lattice in the plane on the length scale of nanorod diameters (of the order 220nm) leaves the nanorod sidewalls free standing, unbound by crystal lattice to neighbouring nanorods. Due to this breaking of the lattice, the local lattice of the nanorod is free to move to a lower energy state, relaxing the strain in the nanorod. One of the critical signatures of this relaxation in strain in InGaN/GaN MQW nanorods is the blue shift in peak PL emission in nanorod compared to as planar epi-wafer. The blue shift is a result of the strain relaxation induced reduction in piezoelectric field across the quantum well. This reduction in electric field reduces the band tilting and emission wavelength is therefore decreased as the effective bandgap energy increases.

To systematically study the reasons for the PL emission intensity enhancement a set of InGaN/GaN MQW nanorods were studied with a range of emission wavelengths (violet, blue and green) with increasing indium mole fraction and therefore increasing strain induced piezoelectric fields. The samples were grown using the same process described earlier, with an AlN buffer layer on c-plane sapphire. The MQW structures consisted of 5 repeats of 2nm InGaN quantum well and 9nm GaN barrier. The indium mole fraction was varied by changing the quantum well growth temperature and XRD  $\omega - 2\theta$  data was fit to obtain the quantum well and barrier thickness and InN mole fraction. The composition of the quantum wells was found to be 10%, 20% and 30% for the violet, blue and green emitting samples respectively. Nanorods arrays were fabricated in following the procedure described in Section 4.2. The PL spectra for the set of samples is presented in Figure 4.14 and shows that all of the InGaN/GaN MQW nanorod samples show a PL emission intensity increase over the corresponding as-grown sample, with the size of the enhancement increasing with emission wavelength. The samples also show a blue-shift in emission wavelength compared to their corresponding as-grown samples, again,

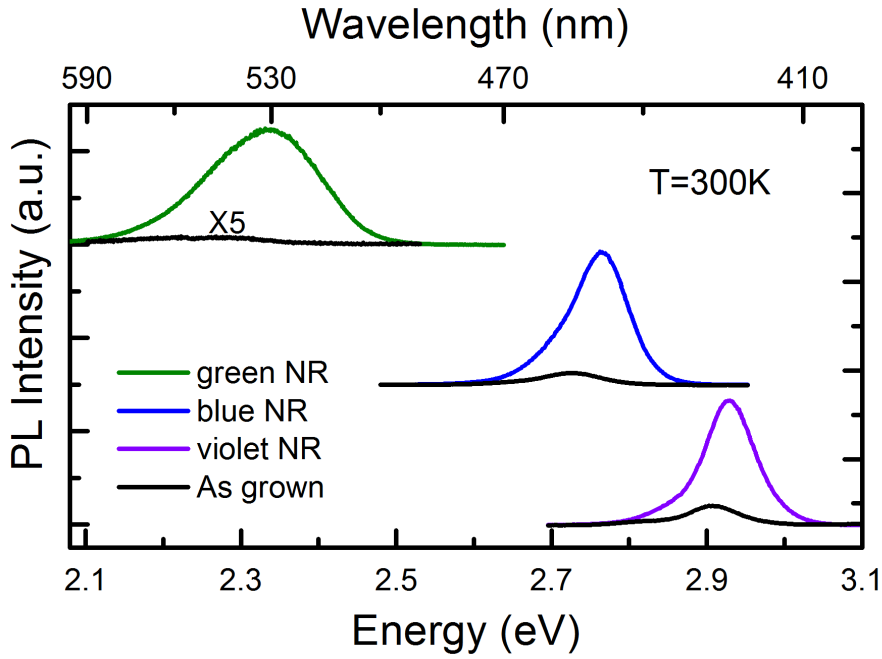


Figure 4.14: Time integrated PL spectra of the three InGaN/GaN MQW nanorod samples with emission wavelengths in the violet, blue and green spectral regions. The corresponding as-grown epiwafer samples are shown in black. All nanorod samples show an increase in PL intensity and a blueshift in emission wavelength.

the magnitude of this blue-shift increases with increasing emission wavelength. The PL enhancements are by factors of 7.2, 11 and 52 for the violet, blue and green emitting samples respectively. The blue-shifts in emission peak are by 2.0nm, 6.7nm and 28.4nm for violet, blue and green emitting samples. It is clear that the PL intensity enhancement and emission peak blue-shift are increased significantly with increasing indium mole fraction in the MQWs. These results are consistent with the effect of strain relaxation as the indium fraction increases, the lattice constant of InGaN increases and with it the strain and therefore the piezoelectric field. Samples with higher indium content therefore are expected to display more significant effects of strain relaxation.

In order to confirm the strain relaxation in the InGaN quantum wells XRD measurements were used to directly measure strain relaxation in the crystal lattice. XRD techniques can be used to probe the strain state of quantum wells in MQW structures by using a technique called reciprocal space mapping (RSM). This involves taking standard  $\omega - 2\theta$  scans as a function of  $\omega$  and allows the strain of the InGaN quantum wells to be measured relative to the GaN layer[32]. The RSMs for the as-grown green emitting MQW wafer and the nanorod green emitting MQW samples are shown in Figure 4.15. The RSM of the as-grown MQW sample shows the InGaN satellite peak positions are along the fully strained line of the GaN buffer peak, indicating that the InGaN quantum wells are fully strained to the GaN. For the nanorod sample however, the InGaN satellite peak positions are between the fully strained (GaN) line and the fully relaxed line, indicating that the InGaN quantum wells are partially relaxed due to the fabrication of the nanorod array.



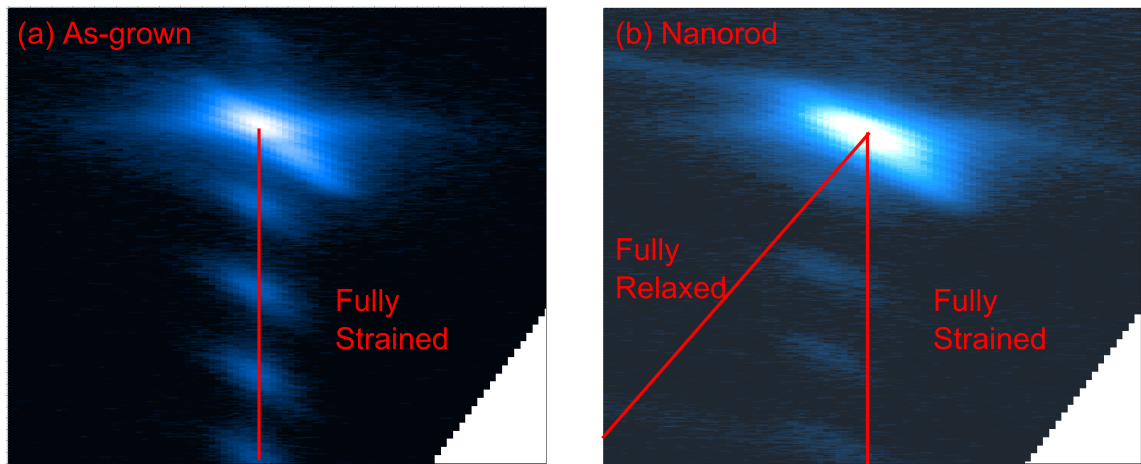


Figure 4.15: X-ray diffraction reciprocal space map (RSM) of the (a) as-grown green emitting MQW wafer and the (b) corresponding nanorod sample. The as grown wafer shows the InGaN satellite peak positions in allong the fully strained line, showing the InGaN MQWs are fully strained to the GaN barrier lattice constant. The nanorod sample shows the InGaN satellite peak positions between the fully strained and fully relaxed lines indicating partial strain relaxation in the InGaN MQWs.

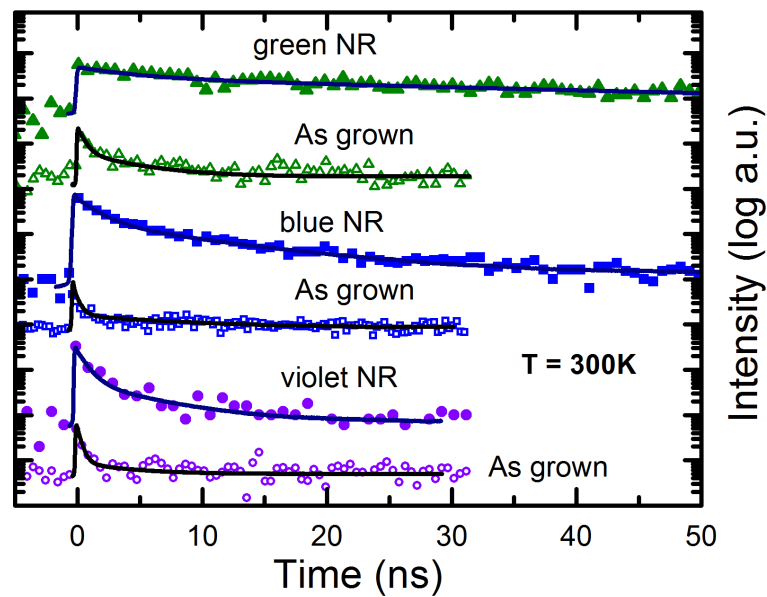


Figure 4.16: Room temperature TRPL traces for the set of MQW nanorods with violet, blue and green emission wavelengths. It is clear that the nanorod samples all show longer decay profiles than their corresponding as grown samples.

### 4.3.1 InGaN/GaN MQW Nanorod Carrier Recombination Dynamics

Time resolved photoluminescence measurements have been carried out at room temperature on this series of samples to examine the exciton dynamics in order to better understand the reasons for the enhancement in PL intensity seen in the nanorod MQW samples. From Figure 4.9 in the previous section it is clear that the for the standard blue emitting MQW, non-radiative decay processes strongly dominate the exciton recombination dy-

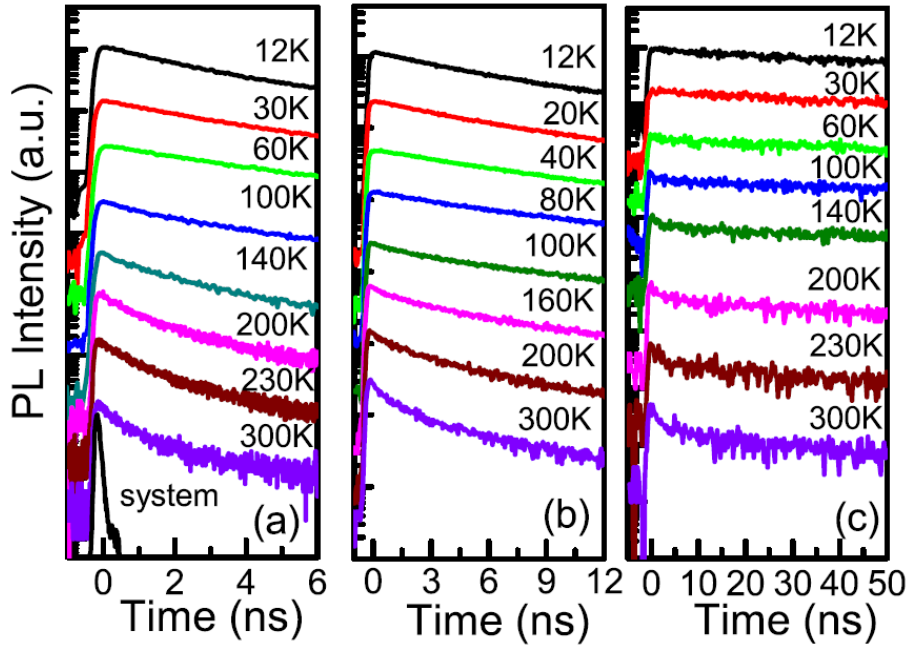


Figure 4.17: Time resolved photoluminescence of InGaN/GaN MQW nanorods at different temperatures. a), b) and c) are violet, blue and green emission wavelengths respectively

nanorods at temperatures higher than  $T = 80\text{K}$ , therefore the room temperature decay traces are most significantly influenced by non-radiative decay. By examining Figure 4.16 it is clear that the nanorod samples all show significantly longer decay profiles than their corresponding as-grown samples. All of the samples used have a quantum well thickness of 2nm and vary only in indium mole fraction, the increasing indium content should lead to increasing strain induced piezoelectric field and therefore increased recombination lifetimes. By examining the decay curves for the as grown set of samples it is clear that the decay is relatively unchanged by the change in indium composition, evidence that non-radiative recombination is dominant at room temperature. The nanorod decay profiles however show longer decay lifetimes than the as grown samples by increasing factors of 3.2, 4.8 and 11.5 times for the violet, blue and green emitting samples respectively. If the reason for PL enhancement was due to strain relaxation alone, it would be expected that the radiative lifetime would increase, leading to longer PL lifetimes. The observed behaviour implies that other processes are also occurring upon nanorod fabrication. Comparing the decay of the three nanorod samples in Figure 4.16, it becomes clear that the lifetime is increasing with increasing indium mole fraction as is expected due to the larger piezo-electric fields. This implies that the nanorod samples are less significantly effected by non-radiative recombination than the as-grown samples as the radiative lifetime is more clear in the measured PL lifetime. In order to investigate this further temperature dependent TRPL measurements were taken. The temperature dependent TRPL data for the set of three InGaN/GaN MQW nanorods is presented in Figure 4.17, (a), (b) and (c) are the violet, blue and green emitting samples respectively. It is immediately clear that the decays of all three samples are more temperature stable with temperature

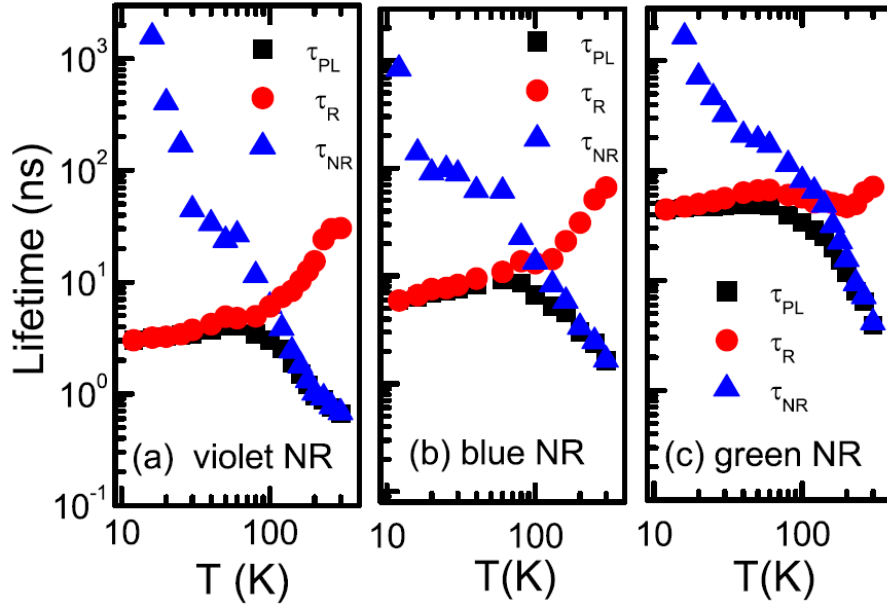


Figure 4.18: The TRPL of the series of InGaN/GaN MQW nanorods as a function of temperature after processing to extract the PL, radiative and non-radiative lifetimes.

than the as grown MQW sample in Figure 4.8. All samples show a slight decrease in lifetime as the temperature is increased, the change is significantly smaller than that seen in the as grown samples. This is a further indication that non-radiative recombination has been significantly reduced. To confirm this, the temperature dependent TRPL data was fit with a bi-exponential function and the fast decay component that dominates the PL decay was taken as the representative PL lifetime. The lifetime data was processed with the temperature dependent time integrated PL derived IQE values to calculate the radiative and non-radiative lifetimes. This data is presented in Figure 4.18. It is clear from Figure 4.18 that the lifetimes in general increase with increasing indium mole fraction at all temperatures (indicated by the gradual offset in the decay curves from violet to green). This increase in lifetime is expected due to the increased strain induced piezo-electric fields. For all samples, non-radiative decay dominates over radiative decay at room temperature, by examining the temperature dependence it becomes apparent that the switching temperature between radiative and non-radiative decay dominating is different for the three samples studied, apparently increasing with increasing indium mole fraction. In order to understand the effect of the fabrication of nanorods has on the temperature dependence of the exciton dynamics, the ratio of radiative to non-radiative lifetimes has been plotted for the set of samples in Figure 4.19. The ratio of radiative to non-radiative recombination lifetime is inversely proportional to the IQE, from Equation 4.6

$$\eta_{IQE} \propto \frac{1}{\left(\frac{\tau_r}{\tau_{nr}}\right)} \quad (4.8)$$

This allows the evaluation of the transition of recombination from radiative to non-radiative, the ratio increases as non-radiative recombination processes become thermally activated,

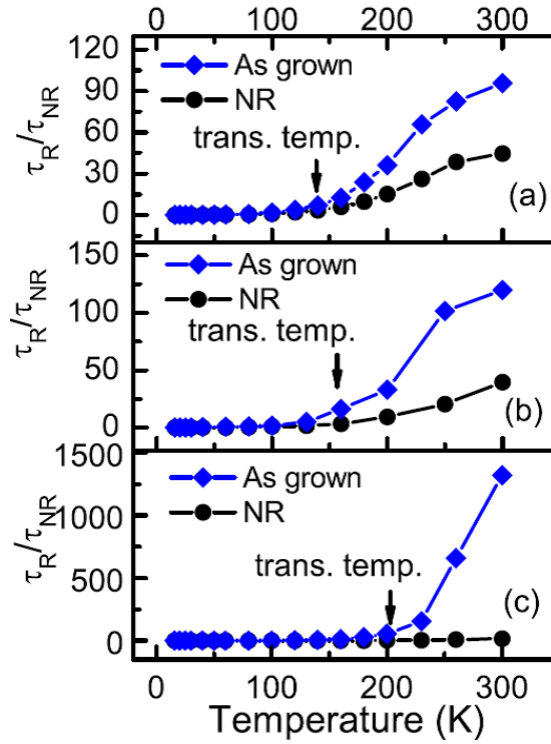


Figure 4.19: The ratio of the radiative and non-radiative lifetimes for the set of violet (a), blue (b) and green (c) emitting InGaN/GaN MQWs. The ratios for the as-grown wafer are compared to the ratios after nanorod fabrication.

leading to a lowering of the IQE of the sample. It is clear that the behaviour of this ratio for nanorod and as-grown sample is very similar for all three InGaN/GaN MQWs for low temperatures. Below  $T = 120\text{K}$ , all samples show that the ratio is small, and there is no significant difference between nanorod and as-grown as radiative recombination is dominant over non-radiative recombination. As the non-radiative recombination centres become thermally activated, the non-radiative recombination rate becomes more significant and all samples show an increase in the ratio at a characteristic temperature referred to here as the transition temperature. All as-grown samples show a significant increase in the radiative/non-radiative ratio above their respective transition temperatures where non-radiative recombination becomes strongly dominant. The nanorod samples however, show a reduced temperature sensitivity, with this increase with temperature less pronounced due to the lower non-radiative recombination rate. Comparing the behaviour of the violet, blue and green emitting MQW samples, it is clear that the reduction in this sensitivity is increased with increasing indium mole fraction. This compliments an increase in the transition temperature for the green emitting sample.

To understand this reduced sensitivity displayed by the green emitting sample, it is worth considering the differences between samples with different indium mole fraction. It is well understood that with increasing indium mole fraction, inhomogeneities such as indium clustering in the InGaN well will increase. This increase in local inhomogeneity leads to increased localization effects. To understand this, TRPL can be used at low temperature to examine the localization depth by measuring the lifetime as a function of

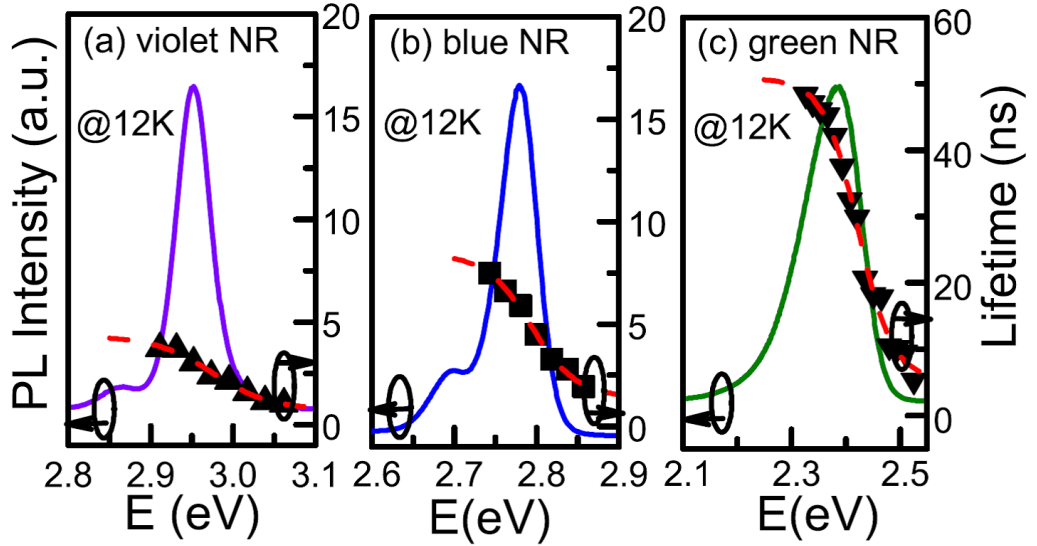


Figure 4.20: The measured TRPL lifetimes as a function of wavelength for the set of InGaN/GaN MQW nanorod samples with emission wavelengths from violet (a) and blue (b) to green (c).

emission wavelength. Figure 4.20 shows the PL lifetimes measured at  $T = 12\text{K}$  at various emission wavelengths across the emission peak for each of the three nanorod samples. It is clear that the lifetime increases significantly with increasing emission wavelength for all three samples. Increasing emission wavelength shows a larger spread of lifetimes with emission wavelengths. This behaviour can be understood as evidence of increasing localization of excitons with increasing indium mole fraction. The increase in lifetime with emission wavelength is a feature caused by the existence of localized excitons in a tail states distribution[25, 29, 33]. The behaviour can be described by Equation 4.9.

$$\tau(E) = \frac{\tau_r}{1 + \exp[(E - E_{me})/E_0]} \quad (4.9)$$

Where  $\tau(T)$  is the lifetime at temperature  $T$ ,  $E$  is the emission energy,  $E_{me}$  is a mobility edge like energy and  $E_0$  is the localization depth. Fitting the data in Figure 4.20 leads to localization depths for the three samples with violet, blue and green emission wavelengths are , 22.5meV, 27.3meV and 31.7meV respectively. The localization depth can therefore be seen to be increasing with indium mole fraction. This can help explain why the transition temperature highlighted in Figure 4.19 increases with increasing indium mole fraction, as the localization depth increases, the thermal energy required to activate the non-radiative recombination centres increases, leading to an increased transition temperature. The significant reduction in non-radiative recombination rate seen in all of the nanorod samples compared to the as-grown samples, cannot be explained by a reduction in strain however, a separate mechanism is proposed to explain this effect.

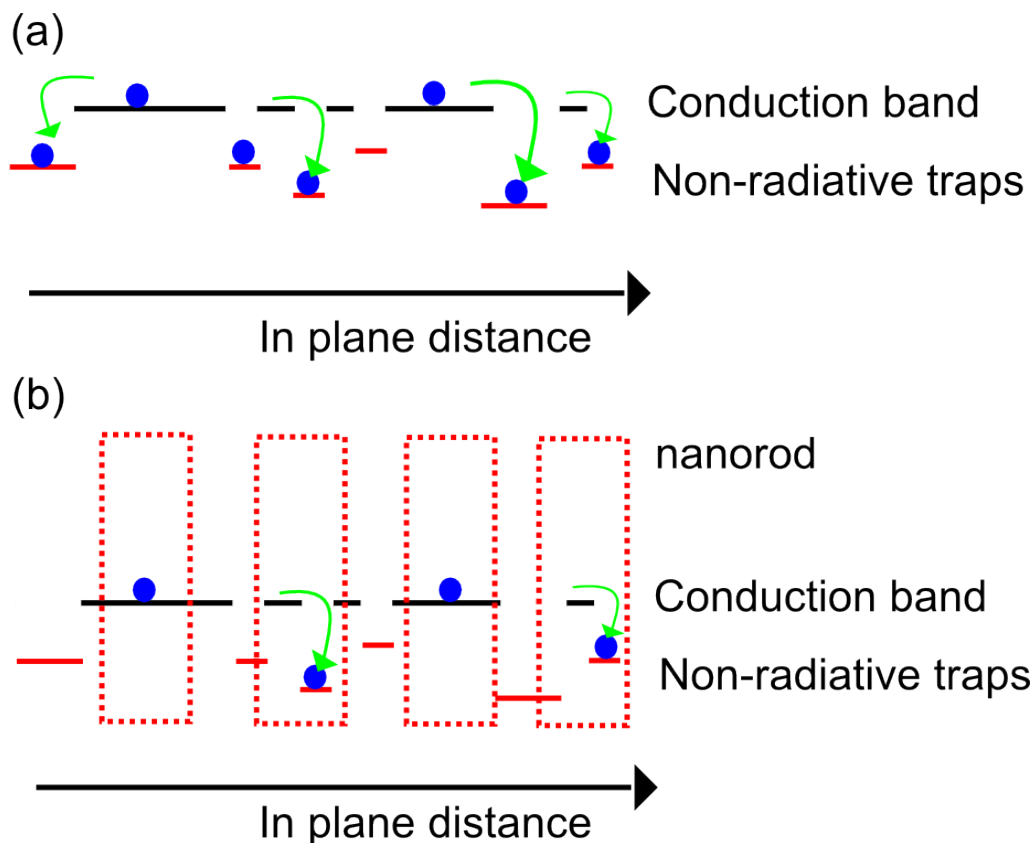


Figure 4.21: A schematic of the effect of lateral confinement on non-radiative recombination. Non-radiative recombination centres are shown in red, it is possible for carriers to migrate to these centres and recombine in the planar structure (a), nanorods however (b), spatially confine carriers, potentially reducing non-radiative recombination

### Lateral Exciton Confinement

Along with strain relaxation, an additional benefit of fabrication of nanorods is potential of extra in-plane lateral confinement of carriers due to the size of the limited dimensions of the nanorods in the plane[8]. The efficacy of lateral confinement depends on the mobility of excitons in the InGaN quantum wells, where lateral confinement will start to effect recombination properties when the diameter of the nanorods approaches the exciton diffusion length. InGaN based LEDs already enjoy significant commercial success and although device efficiencies are still a long way from their theoretical potential the efficiencies of these devices are significantly higher than the defect density of the heteroepitaxial III-nitrides should support. It has been widely reported that the reason for this high performance is due to localization of excitons at the local potential minima due to sub-micron scale inhomogeneities[19, 34–36]. If the length scale of the nanorod induced additional lateral confinement is similar to the non-radiative recombination centre separation then it is possible for the additional lateral confinement to localize excitons away from non-radiative recombination centres and reduce the probability of non-radiative recombination in the InGaN quantum wells. A schematic of this lateral confinement is shown in Figure 4.21.

The sub-micron local inhomogeneities in InGaN have been probed by scanning near

field optical microscopy (SNOM)[22] and by cathodoluminescence[19]. Revealing fluctuations of emission intensity and emission wavelength on length scales are on the order of, or larger than the typical nanorod diameter of 220nm it is reasonable to assume that if localization on the length scale of hundreds of nanometers at low temperature can reduce exciton diffusion to non-radiative recombination centres then the nanorod enabled lateral confinement on a length scale or approximately 220nm will be significant in reducing diffusion to non-radiative recombination centres, even at room temperature.

Published values of exciton diffusion length in InGaN vary significantly from sub 100nm [25] to hundreds of nanometers[37, 38]. The diffusion of excitons in the quantum well is described by the exciton diffusion length ( $L_{diff}$ ) given by[38, 39]:

$$L_{diff} = \sqrt{D\tau_t} \quad (4.10)$$

Where the exciton diffusion coefficient is  $D = \mu k_B T / q$ . As the effective masses in InN are lower than those in GaN[40], with increasing indium mole fraction the effective mass is reduced. This leads to an increased exciton mobility  $\mu$  and also increased diffusion length. This increase in excitonic diffusion length can explain the increased benefit of nanorod lateral confinement for higher indium composition samples shown in Figure 4.19. Where the longer wavelength emitting samples show lower temperature sensitivity of the radiative/non-radiative lifetime ratio, as the nanorod lateral confinement is more likely to have an influence on exciton diffusion when exciton diffusion length is increased.

## 4.4 Summary

InGaN/GaN MQW nanorod arrays have been fabricated by a post growth, top-down fabrication process. The performance of the MQWs increases significantly in the nanorod array structures compared to the as grown planar MQW wafer. The fabrication process results in a blue-shift in emission peak wavelength, a signature of strain relaxation in the quantum wells and an increase in PL intensity. An investigation of the exciton recombination dynamics in the InGaN/GaN MQWs reveals that the room temperature PL lifetime is significantly longer for the MQWs after nanorod fabrication. It has been shown that this increase in room temperature PL lifetime is as a result the reduction of the non-radiative recombination rate in the MQWs in the nanorod arrays. A model has been developed based on the increased lateral confinement of MQW excitons leading to a reduced rate of diffusion of excitons to non-radiative recombination centres to explain these results.

## References

- <sup>1</sup>Y. Kawakami, a. Kaneta, L. Su, Y. Zhu, K. Okamoto, M. Funato, a. Kikuchi, and K. Kishino, “Optical properties of InGaN/GaN nanopillars fabricated by postgrowth chemically assisted ion beam etching”, *Journal of applied physics* **107**, 023522 (2010).
- <sup>2</sup>Q. Wang, J. Bai, Y. P. Gong, and T. Wang, “Influence of strain relaxation on the optical properties of InGaN/GaN multiple quantum well nanorods”, *Journal of physics d: applied physics* **44**, 395102 (2011).
- <sup>3</sup>J. Bai, Q. Wang, and T. Wang, “Greatly enhanced performance of InGaN/GaN nanorod light emitting diodes”, *Physica status solidi (a)* **209**, 477–480 (2012).
- <sup>4</sup>T.-H. Hsueh, H.-W. Huang, C.-C. Kao, Y.-H. Chang, M.-C. Ou-Yang, H.-C. Kuo, and S.-C. Wang, “Characterization of InGaN/GaN Multiple Quantum Well Nanorods Fabricated by Plasma Etching with Self-Assembled Nickel Metal Nanomasks”, *Japanese journal of applied physics* **44**, 2661–2663 (2005).
- <sup>5</sup>C.-Y. Chang and Y.-R. Wu, “Study of Light Emission Enhancement in Nanostructured InGaN/GaN Quantum Wells”, *Ieee journal of quantum electronics* **46**, 884–889 (2010).
- <sup>6</sup>C.-F. Lin, J.-H. Zheng, Z.-J. Yang, J.-J. Dai, D.-Y. Lin, C.-Y. Chang, Z.-X. Lai, and C. S. Hong, “High-efficiency InGaN-based light-emitting diodes with nanoporous GaN:Mg structure”, *Applied physics letters* **88**, 083121 (2006).
- <sup>7</sup>C. C. S. Chan, B. P. L. Reid, R. a. Taylor, Y. Zhuang, P. a. Shields, D. W. E. Allsopp, and W. Jia, “Optical studies of the surface effects from the luminescence of single GaN/InGaN nanorod light emitting diodes fabricated on a wafer scale”, *Applied physics letters* **102**, 111906 (2013).
- <sup>8</sup>B. Jiang, C. Zhang, X. Wang, F. Xue, M. J. Park, J. S. Kwak, and M. Xiao, “Effects of reduced exciton diffusion in InGaN/GaN multiple quantum well nanorods.”, *Optics express* **20**, 13478–87 (2012).
- <sup>9</sup>D. S. Y. Hsu, C. S. Kim, C. R. Eddy, R. T. Holm, R. L. Henry, J. a. Casey, V. a. Shamamian, and A. Rosenberg, “Using Ni masks in inductively coupled plasma etching of high density hole patterns in GaN”, *Journal of vacuum science & technology b: microelectronics and nanometer structures* **23**, 1611 (2005).
- <sup>10</sup>J. Bai, Q. Wang, and T. Wang, “Characterization of InGaN-based nanorod light emitting diodes with different indium compositions”, *Journal of applied physics* **111**, 113103 (2012).
- <sup>11</sup>B. Liu, R. Smith, J. Bai, Y. Gong, and T. Wang, “Great emission enhancement and excitonic recombination dynamics of InGaN/GaN nanorod structures”, *Applied physics letters* **103**, 101108 (2013).



- <sup>12</sup>H. Huang, C. Kao, T. Hsueh, C. Yu, C. Lin, J. Chu, H. Kuo, and S. Wang, “Fabrication of GaN-based nanorod light emitting diodes using self-assemble nickel nano-mask and inductively coupled plasma reactive ion etching”, *Materials science and engineering b* **113**, 125–129 (2004).
- <sup>13</sup>J. Bai, T. Wang, P. Parbrook, K. Lee, and a.G. Cullis, “A study of dislocations in AlN and GaN films grown on sapphire substrates”, *Journal of crystal growth* **282**, 290–296 (2005).
- <sup>14</sup>J. Bai, T. Wang, P. Comming, P. J. Parbrook, J. P. R. David, and A. G. Cullis, “Optical properties of AlGaN/GaN multiple quantum well structure by using a high-temperature AlN buffer on sapphire substrate”, *Journal of applied physics* **99**, 023513 (2006).
- <sup>15</sup>J. Bai, T. Wang, P. Parbrook, I. Ross, and A. Cullis, “V-shaped pits formed at the GaN/AlN interface”, *Journal of crystal growth* **289**, 63–67 (2006).
- <sup>16</sup>S. C. Davies, D. J. Mowbray, Q. Wang, F. Ranalli, and T. Wang, “Influence of crystal quality of underlying GaN buffer on the formation and optical properties of InGaN/GaN quantum dots”, *Applied physics letters* **95**, 101909 (2009).
- <sup>17</sup>Q. Wang, T. Wang, J. Bai, a. G. Cullis, P. J. Parbrook, and F. Ranalli, “Growth and optical investigation of self-assembled InGaN quantum dots on a GaN surface using a high temperature AlN buffer”, *Journal of applied physics* **103**, 123522 (2008).
- <sup>18</sup>S. F. Chichibu, Y. Kawakami, and T. Sota, “Emission Mechanisms and Excitons in GaN and InGaN Bulk and QWs”, in *Introduction to nitride semiconductor blue lasers and light emitting diodes*, edited by S. Nakamura and S. F. Chichibu (CRC PRESS, 2000), pages 153–270.
- <sup>19</sup>K. Okamoto and Y. Kawakami, “High-Efficiency InGaN/GaN Light Emitters Based on Nanophotonics and Plasmonics”, *Ieee journal of selected topics in quantum electronics* **15**, 1199–1209 (2009).
- <sup>20</sup>J. Chen, Z. Feng, J. Wang, H. Tsai, J. Yang, a. Parekh, E. Armour, and P. Faniano, “Study of carrier localization in InGaN/GaN quantum well blue-light-emitting diode structures”, *Journal of crystal growth* **287**, 354–358 (2006).
- <sup>21</sup>C. Netzel, C. Mauder, T. Wernicke, B. Reuters, H. Kalisch, M. Heuken, A. Vescan, M. Weyers, and M. Kneissl, “Strong charge carrier localization interacting with extensive nonradiative recombination in heteroepitaxially grown m-plane GaInN quantum wells”, *Semiconductor science and technology* **26**, 105017 (2011).
- <sup>22</sup>Y. Kawakami, K. Omae, A. Kaneta, K. Okamoto, Y. Narukawa, T. Mukai, and S. Fujita, “In inhomogeneity and emission characteristics of InGaN”, *Journal of physics: condensed matter* **13**, 6993–7010 (2001).
- <sup>23</sup>P. G. Eliseev, P. Perlin, J. Lee, and M. Osinnski, “Blue temperature-induced shift and band-tail emission in InGaN-based light sources”, *Applied physics letters* **71**, 569 (1997).

- <sup>24</sup>Y.-H. Cho, G. H. Gainer, a. J. Fischer, J. J. Song, S. Keller, U. K. Mishra, and S. P. DenBaars, “S-shaped temperature-dependent emission shift and carrier dynamics in InGaN/GaN multiple quantum wells”, *Applied physics letters* **73**, 1370 (1998).
- <sup>25</sup>S. Chichibu, H. Marchand, and M. Minsky, “Emission mechanisms of bulk GaN and InGaN quantum wells prepared by lateral epitaxial overgrowth”, *Applied physics* **74**, 1460–1462 (1999).
- <sup>26</sup>J. H. Na, R. a. Taylor, K. H. Lee, T. Wang, A. Tahraoui, P. Parbrook, a. M. Fox, S. N. Yi, Y. S. Park, J. W. Choi, and J. S. Lee, “Dependence of carrier localization in InGaN/GaN multiple-quantum wells on well thickness”, *Applied physics letters* **89**, 253120 (2006).
- <sup>27</sup>X. Chen, B. Henderson, and K. P. O Donnell, “Luminescence decay in disordered low-dimensional semiconductors”, *Applied physics letters* **60**, 2672 (1992).
- <sup>28</sup>S.-W. Feng, Y.-C. Cheng, C.-C. Liao, Y.-Y. Chung, C.-W. Liu, C.-C. Yang, Y.-S. Lin, K.-J. Ma, and J.-I. Chyi, “Two-Component Photoluminescence Decay in InGaN/GaN Multiple Quantum Well Structures”, *Physica status solidi (b)* **228**, 121–124 (2001).
- <sup>29</sup>S. F. Chichibu, T. Onuma, T. Aoyama, K. Nakajima, P. Ahmet, T. Chikyow, T. Sota, S. P. DenBaars, S. Nakamura, T. Kitamura, Y. Ishida, and H. Okumura, “Recombination dynamics of localized excitons in cubic  $\text{In}_x\text{Ga}_{1-x}\text{N}/\text{GaN}$  multiple quantum wells grown by radio frequency molecular beam epitaxy on 3C-SiC substrate”, *Journal of vacuum science & technology b: microelectronics and nanometer structures* **21**, 1856 (2003).
- <sup>30</sup>J. Feldmann, G. Peter, E. Göbel, P. Dawson, K. Moore, C. Foxon, and R. Elliott, “Linewidth dependence of radiative exciton lifetimes in quantum wells”, *Physical review letters* **59**, 2337–2340 (1987).
- <sup>31</sup>M. Athanasiou, T. K. Kim, B. Liu, R. Smith, and T. Wang, “Fabrication of two-dimensional InGaN/GaN photonic crystal structure using a modified nanosphere lithography technique”, *Applied physics letters* **102**, 191108 (2013).
- <sup>32</sup>M. A. Moram and M. E. Vickers, “X-ray diffraction of III-nitrides”, *Reports on progress in physics* **72**, 036502 (2009).
- <sup>33</sup>Y.-A. Liao, W.-T. Hsu, P.-C. Chiu, J.-I. Chyi, and W.-H. Chang, “Effects of thermal annealing on the emission properties of type-II InAs/GaAsSb quantum dots”, *Applied physics letters* **94**, 053101 (2009).
- <sup>34</sup>D. Gerthsen, E. Hahn, B. Neubauer, A. Rosenauer, O. Schon, M. Heuken, and A. Rizzi, “Composition Fluctuations in InGaN Analyzed by Transmission Electron Microscopy”, *Physica status solidi (a)* **177**, 145–155 (2000).
- <sup>35</sup>P. Ruterana, S. Kret, A. Vivet, G. Maciejewski, and P. Dluzewski, “Composition fluctuation in InGaN quantum wells made from molecular beam or metalorganic vapor phase epitaxial layers”, *Journal of applied physics* **91**, 8979 (2002).

- <sup>36</sup>M. J. Galtrey, R. a. Oliver, M. J. Kappers, C. J. Humphreys, D. J. Stokes, P. H. Clifton, and A. Cerezo, “Three-dimensional atom probe studies of an In<sub>x</sub>Ga<sub>1-x</sub>N/GaN multiple quantum well structure: Assessment of possible indium clustering”, *Applied physics letters* **90**, 061903 (2007).
- <sup>37</sup>S. J. Rosner, G. Girolami, H. Marchand, P. T. Fini, J. P. Ibbetson, L. Zhao, S. Keller, U. K. Mishra, S. P. DenBaars, and J. S. Speck, “Cathodoluminescence mapping of epitaxial lateral overgrowth in gallium nitride”, *Applied physics letters* **74**, 2035 (1999).
- <sup>38</sup>V. Liuolia, S. Marcinkevicius, Y.-D. Lin, H. Ohta, S. P. DenBaars, and S. Nakamura, “Dynamics of polarized photoluminescence in m-plane InGaN/GaN quantum wells”, *Journal of applied physics* **108**, 023101 (2010).
- <sup>39</sup>L. Baird, C. P. Ong, R. A. Cole, N. M. Haegel, a. A. Talin, Q. Li, and G. T. Wang, “Transport imaging for contact-free measurements of minority carrier diffusion in GaN, GaN/AlGaN, and GaN/InGaN core-shell nanowires”, *Applied physics letters* **98**, 132104 (2011).
- <sup>40</sup>Y.-K. Kuo, B.-T. Liou, M.-L. Chen, S.-H. Yen, and C.-Y. Lin, “Effect of band-offset ratio on analysis of violet-blue InGaN laser characteristics”, *Optics communications* **231**, 395–402 (2004).



---

## Non-Radiative Energy Transfer from InGaN MQW Nanorod Arrays to a Light Emitting Polymer

---

### **5.1 Hybrid Organic / Inorganic Structures for LEDs using Non-radiative Energy Transfer**

As was covered in Chapter 1, the most commonly used method of generating white light using LEDs is by the down conversion technique, where phosphor materials are used to convert a portion of the blue emission from InGaN/GaN MQWs to longer wavelength emission to generate white light. Although this phosphor conversion technology is widespread, there are still issues facing this technology (as discussed in Chapter 1) where novel solutions offer potential routes to enhancing performance. Some have chosen to focus research on generating white light without use of phosphors or any down-conversion material. Nguyen et al. used MBE grown GaN nanowires containing multiple layers of InGaN quantum dots to produce broad emission spectra to avoid the use of phosphors and their potential drawbacks[1]. Research is also ongoing into MOCVD grown three dimensional structures such as core shell nanorods, where broad spectrum visible light emission is generated at InGaN quantum wells on different crystal facets of GaN nanorods[2]. Such approaches allow the potential for phosphor free white LED operation but are at the early stages of research and the performance of such devices is not comparable with standard LED devices. Typically such three dimensional LED structures face difficulties in the fabrication of good electrical contacts and p-n junctions with shorting and current leakage problems. Combining the benefits of both organic and inorganic semiconductor materials together to create hybrid optoelectronics with improved performance is an area of increasing interest as was covered in Chapter 2. The benefits of using hybrid organic/inorganic structures can range from the more basic direct phosphor replacement [3–5] to novel

structures that make use of near field coupling regimes[6] or hybrid exciton states[7]. As discussed in Chapter 1, the use of organic materials can allow for the problems of phosphor intellectual property to be circumvented as access to the full visible spectrum with a wide variety of organic materials (also beneficial for improving CRI of white LEDs). Full down-conversion LEDs have been demonstrated using a UV emitting LED and a blend of organic materials as down conversion medium[5]. Such devices with direct phosphor replacement take advantage of some of the benefits of hybrid devices such as the potential for high photoluminescence efficiencies of some organic light emitters with low self absorption (due to potentially large Stokes shifts) and high IQE [8]. The ability to blend a variety of different wavelength emitting polymers allows high colour qualities to be achieved with precise control over the emission spectrum, Itskos et al. demonstrated this with a blend of three different polyfluorene based organic materials[9]. Significant further benefits can be found by using the properties of such hybrid structures to take advantage of near field coupling mechanisms not possible with traditional phosphors.

### Non-radiative Energy Transfer (NRET)

Traditional phosphor down-conversion works on the principal of emission of a photon by the higher energy pump system, transfer of the photon to the phosphor material, absorption by the phosphor and finally re-emission of the down-converted photon at a lower energy. This radiative coupling is potentially infinite in range, with real photons as the exchange particle. Over short ranges however (the near field regime) the nature of energy transfer changes. Theodore Förster developed a theory in 1946 to describe the near field coupling between resonant dipoles with separations of the order  $d \approx \frac{\lambda}{2\pi}$  that later became known as Förster energy transfer or Förster Resonant Energy Transfer (FRET)[10]. This theoretical basis was originally developed to describe the energy transfer between an excited molecule and a molecule in an unexcited state, with resonant emission and absorption where the dipoles are Frenkel excitons of the molecules, with small dipole radius compared to exciton separation. Förster showed that FRET requires spectral overlap between the emission of the donor molecule and absorption of the acceptor molecule. In this molecular case, the FRET transfer rate has an inverse sixth power dependence on the separation of donor and acceptor dipoles with the FRET rate  $k_t$  given by[11]:

$$k_t = \left( \frac{1}{\tau_D} \right) \left( \frac{R_0}{r_{DA}} \right)^6 \quad (5.1)$$

Where  $\tau_D$  is the relaxation rate of the excited state of the excited (donor) molecule by all processes apart from FRET.  $R_0$  is the characteristic distance known as the Förster radius, defined as the separation between donor and acceptor molecules where FRET rate drops to 50% of maximum (which depends on material properties and relative dipole alignments).  $r_{DA}$  is the separation between donor and acceptor dipoles. The FRET process important in organic and biological systems as a method of energy transfer between iso-

lated molecules at small separations, with FRET microscopy used as a super-resolution microscopy technique to measure separations between molecules on the order of 10nm [11]. In 1989 and in further detail in 2004 Andrews et al. used quantum electro-dynamics (QED) to examine non-radiative energy transfer[12, 13]. At first a QED description of radiative energy transfer was constructed, before examining the exchange with varying separation. It was shown that at short distances (the near-field), the exchange of energy between excited donor and ground state acceptor is mediated by a virtual photon. This description allows for a unified theory, where at large separation the exchange of energy is by real photon and as separation is reduced the exchanged photon becomes virtual in nature. Leading to the argument that non-radiative energy transfer is the near-field asymptote of radiative energy transfer. Hill et al. used monolayers of molecules fabricated by the Langmuir-Blodgett process to control the separation between donor and acceptor molecules in separated parallel macroscopic two dimensional films[14]. The FRET process between the two films was probed by use of time resolved photoluminescence measurements to examine changes in the exciton dynamics caused by FRET. The FRET rate was found to deviate from the  $r^{-6}$  dependence in Förster's theory that has been widely observed when the dipoles are essentially separated points. A dependence of FRET rate on film separation of  $r^{-2}$  was found to exist in this geometry and was explained by the integration of two point dipoles, each over an infinite two dimensional sheet.

### **Non-radiative Energy Transfer for Down-conversion LEDs**

The potential application of NRET processes in a down-conversion LED were presented in a theoretical investigation into novel hybrid organic/inorganic device structures based on inorganic quantum wells light emitting organic layers out by Basko et al.[15]. Here the benefits of combining inorganic semiconductors with the high electrical injection efficiencies and the optical properties of organic semiconductors was proposed in a configuration that would allow the use of FRET as the dominant energy transfer mechanism. The structure proposed consisted of an inorganic quantum well with a thin top barrier layer to allow the separation between the inorganic quantum well excitons and excitons in the organic overlayer to be reduced to 5nm. Using this structure, Basko et al. calculated that FRET rates of the range 10 – 100ps could be achieved, being faster than typical lifetime of inorganic quantum well excitons, the emission from the inorganic material in this case would be quenched, with energy transferred to the organic overlayer. The major challenge facing the practical implementation of LEDs utilizing FRET is the need to reduce separation between the donor and acceptor excitons.

The first practical demonstration of a hybrid light emitting device structure utilizing NRET came not through the use of a hybrid organic/inorganic structure, but using a III-V InGaN quantum well coupled to II-VI semiconductor colloidal quantum dots as the down-conversion acceptor[16]. A structure similar to that described by Basko et al. was used, with an InGaN/GaN single quantum well structure with a thin top GaN capping

layer. The emission wavelength of the InGaN quantum well used was 400nm with CdSe colloidal quantum dots of emission wavelength 575nm deposited on the top GaN barrier (barrier thickness = 3nm). By measuring time resolved PL of the InGaN quantum well, the lifetime of carriers in the quantum well was seen to decrease in the presence the quantum dot overlayer due to non-radiative decay from the quantum well to the quantum dots. An energy transfer efficiency of 55% was found in this study. Further development of this idea led to an electrically injected device with a similar structure, a single InGaN quantum well and thin n-GaN cap coated with colloidal quantum dots[17]. In order to minimize separation between quantum well and quantum dot excitons, the top capping layer must be extremely thin (based on typical Förster radii less than 5 – 10nm) which leads to poor LED performance due to current spreading issues.

Hybrid organic/inorganic structures were fabricated by Heliotis et al.[6] using a similar structure to that proposed by Basko et al. in 1999. Again a single InGaN quantum well was used, with an emission wavelength of 385nm and three different GaN cap thicknesses 15, 4 and 2.5nm. A blue emitting polyfluorene, F8DP, was deposited on the top GaN cap of the three samples and the InGaN quantum well was optically excited with a laser. The different GaN cap thickness allowed the energy transfer dependence on separation between quantum well and organic excitons to be characterized. Temperature dependent time integrated PL measurements were taken for both the emission peaks of InGaN and F8DP. The F8DP peak on a glass substrate was found to have no temperature dependence over the range 77 – 300K, unlike the InGaN with a strong decrease in PL intensity with increasing temperature. A signature of the InGaN quantum well temperature dependence was found in the emission peak of the F8DP for the hybrid samples with varying temperature. The strength of this temperature dependent signature was found to increase with decreasing cap thickness, as where FRET is strongly sensitive to separation the radiative pumping is not. It was argued that with a 15nm GaN cap (exciton separation) the FRET process was negligible. This re-enforces the importance of reducing exciton separation in any hybrid device employing FRET.

Chanyawadee et al. demonstrated a different approach to fabricating a hybrid device utilizing a higher efficiency InGaN MQW structure with a standard thick top p-GaN cap non-radiatively coupled to colloidal II-VI quantum dots[18]. In order to reduce the separation of InGaN and quantum dot excitons from the  $\approx$  200nm of a standard p-GaN cap layer thickness to the less than 10nm required for FRET by the etching of a holes through the MQW structures followed by the filling of these holes with quantum dots. Nanoimprint lithography was used to create an etch mask of dots and dashes on the InGaN LED wafer followed by dry etching the pattern either through the p-GaN cap of through the MQW region below. The holes were filled and TRPL PL measurements used to measured the change in recombination dynamics due to the presence of the colloidal quantum dots. The sample with etched holes that did not penetrate the quantum well layer (hence separation of InGaN and quantum dot excitons is large) showed no change in MQW dynamics.



The sample with low exciton separation showed a change in recombination dynamics in the MQW as a result of FRET to the colloidal quantum dots.

### **InGaN/GaN MQW Nanorods for Non-radiative Energy Transfer**

The use of FRET as the coupling mechanism of the electrically injected quantum wells of a white LED to the down-conversion medium has great potential to increase efficiencies of white LEDs. FRET does not require radiative recombination in the donor material, extraction of the emitted photon from the donor material and finally absorption of the photon by the down conversion medium, as such the process can be more efficient than radiative energy transfer. As the energy transfer rates achievable with FRET between an inorganic MQW donor and an organic acceptor layer are potentially extremely fast [15], the FRET energy transfer mechanism has the potential to compete with non-radiative decay processes in the inorganic quantum wells, leading to increases in device efficiency. The most significant barrier to the use of FRET in hybrid structures is the need to reduce the separation between MQW excitons and excitons in the down conversion medium to distances of less than 10nm. This is not possible with traditional LED structures that require p-GaN capping layer thicknesses of at least 150 to 200nm or with phosphor materials that have typical grain sizes on the order of microns [19–21]. As such, novel device structures are required to enable the utilization of FRET in commercially applicable white LED technologies.

In the previous chapter, the benefits of InGaN/GaN MQW nanorods fabricated by a post growth top-down etch process were presented. With a significant increase in the PL intensity of InGaN/GaN MQW nanorods due to strongly reduced non-radiative recombination, this process is promising for improving the performance of InGaN LEDs. This self assembled nanorod array structure has further benefits, by exposing the sidewalls of the multiple quantum wells, it is possible to create novel hybrid structures that minimize separation between excitons in the MQWs and a material placed on the nanorod sidewalls. A hybrid III-V/II-VI structure was demonstrated by Nizamoglu et al. based on InGaN/GaN MQW nanorods fabricated by post growth top-down etching process and colloidal II-VI quantum dots deposited on-top of the MQW nanorod arrays [22]. A similar method was used to investigate the energy transfer between blue emitting InGaN/GaN MQWs and the red emitting II-VI quantum dots, with TRPL used to examine the reduction in MQW exciton lifetime due to the additional non-radiative recombination pathway of FRET. The lifetime of the MQW excitons was found to reduce significantly along with a large quenching of MQW emission intensity.

Before this work there were no reports of hybrid organic/inorganic devices utilizing nanostructuring approaches to enable high efficiency FRET. Through the use of the self assembled top down nanorods described in the previous chapter, it is possible to not only increase the performance of blue emitting InGaN/GaN MQWs but also to give the possibility of using the high efficiency (high speed) Non-radiative energy transfer coupling to

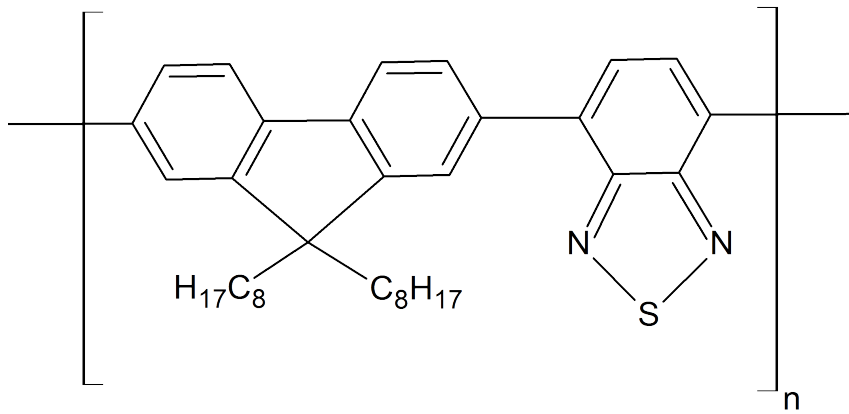


Figure 5.1: The structure of the polyfluorene co-polymer used in this work F8BT. The F8 unit is on the left with the BT unit on the right.

a high efficiency organic light emitting material as a down conversion medium. With exposed vertical sidewalls, the InGaN MQWs of MQW nanorods can potentially be directly coated with a light emitting polymer, giving rise to an extremely small separation between MQW and organic excitons, leading to the potential of extremely fast non-radiative energy transfer of energy from InGaN/GaN MQWs to the light emitting organic coating.

In this chapter the fabrication and characterization of hybrid light emitting polymer - InGaN/GaN MQW nanorod structures is presented, by first examining the fabrication and characterization of the organic materials.

## 5.2 Light Emitting Polymer Deposition and Characterization

To investigate the potential of hybrid organic/InGaN MQW nanorod structures an organic material was chosen with an absorption peak in the blue and emission in the yellow spectral regions to fit with the idea of a down converted white emitting device structure. The material used was poly(9,9-dioctylfluorenyl-2,7-diyl-co-1,4-benzo-(2,1,3)-thiadiazole)) (F8BT), a yellow emitting polyfluorene co-polymer shown in Figure 5.1. The absorption and emission spectra of F8BT films spin-coated from toluene are shown in Figure 5.2, the main absorption peak of polymer is broad and centred at 460nm closely matching the emission peak of blue emitting nanorods at  $\approx 450\text{nm}$ . A second, higher energy absorption peak at 350nm is also present and although the exact nature of this peak is not yet well understood, it has been observed that pumping F8BT at this higher energy absorption feature requires some intra-molecular energy transfer and results in a lower PL efficiency[23]. The emission band is broad with a peak at 540nm and exhibits a long, low energy tail giving an overall yellow emission appearance. F8BT is soluble in toluene and can also be easily spin-coated. Initially, solutions were prepared and spin-coating was carried out in the photo-lithography yellow room in a cleanroom environment. PL measurements taken using a 375nm laser diode as excitation source measured at room

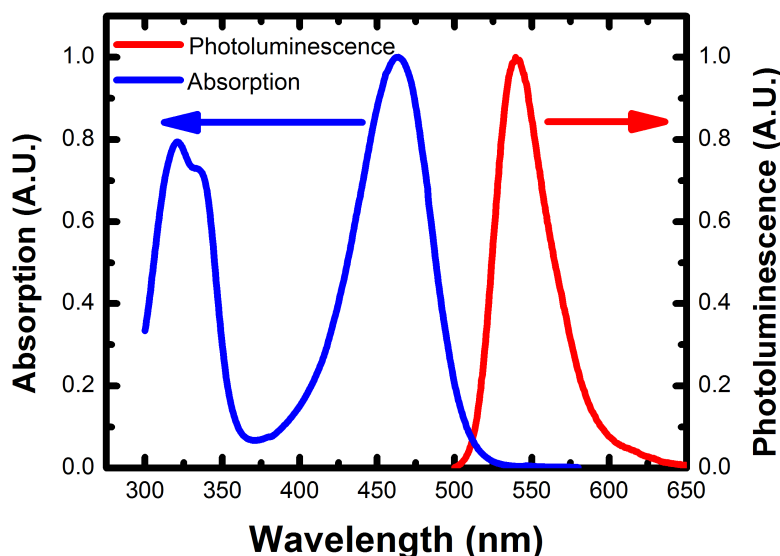


Figure 5.2: The absorption and emission properties of a layer of F8BT deposited on a sapphire substrate from a solution of toluene

temperature in air. Significant degradation in the PL intensity with laser exposure was found, shown in Figure 5.3. Photo-degradation and specifically photo-oxidation are a major challenge for light emitting polymers in general due to the sensitivity of the conjugated bonds present, this problem is also significant for the polyfluorene class of polymers such as F8BT[24]. The formation of bonds to oxygen when electrons are promoted to excited states in the molecules leads to the formation of keto defects[25]. In shorter wavelength emitting polyfluorenes this defect formation is linked to a red-shift in emission peak towards the green spectral region. Due to the longer emission wavelength of F8BT caused by the BT unit in the co-polymer, this is not visible in the degradation of the film in Figure 5.3. In this case only a decrease in PL intensity is visible, without any discernible change in emission spectral profile. Another potential degradation mechanism facing organic light emitting materials is photo-bleaching, which can occur when the intensity of incident light on a material is sufficient to damage the bonds and permanently degrade the structure of the polymer. Due to the low laser excitation power densities used and after tests showing degradation at even lower laser power densities, the dominant degradation mechanism was expected to be photo-oxidation.

In order to process and characterize F8BT films without significant degradation effects, air sensitive techniques were developed and implemented. Initial tests using partially nitrogen purged environments for processing and carrying out PL measurements in an optical cryostat under vacuum showed a reduction in degradation rate. After this testing and confirming that the nature of degradation was indeed a photo-oxidation process, all organic processing was carried out in a glove box environment with a forming gas atmosphere (95% N<sub>2</sub>, 5% H<sub>2</sub>) using a palladium catalyst to reduce oxygen from the atmosphere, resulting in O<sub>2</sub> levels of < 0.5ppm, the lower limit of the detector available.

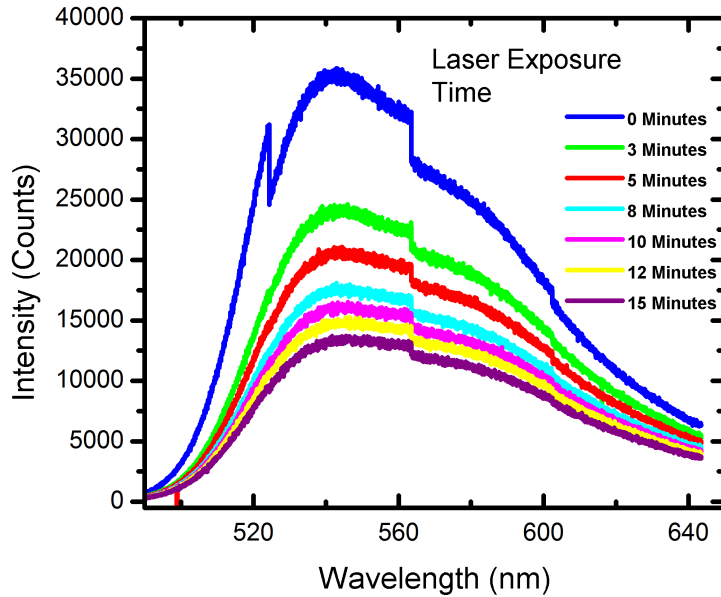


Figure 5.3: Photoluminescence of an F8BT film deposited on a single GaN layer on sapphire measured at intervals of 2 – 3 minutes with constant laser exposure. The F8BT film was deposited and measured in air, excitation is with a 375nm laser diode operating at 4mW power in CW mode. A decrease of 68% in peak intensity is observed. The discontinuities are from degradation that occurs between CCD acquisitions as the monochromator scans to a new centre wavelength

Samples with F8BT films on the surface were transferred to an optical cryostat minimizing exposure to oxygen and ambient light. Once held in the cryostat a turbo-molecular pump was used to evacuate the sample chamber and maintain a vacuum of approximately  $10^{-6}$ Torr. The samples were then held under vacuum in darkness for at least 24 hours to degas any adsorbed oxygen from the samples before exposure to laser illumination and PL measurements were carried out. Figure 5.4 shows PL from an F8BT film processed and measured using the above methods. Under identical laser power no significant degradation is observed over fifteen minutes of laser exposure. This indicates that the F8BT film is stable enough for photoluminescence measurements to be used to characterize hybrid structures.

F8BT was deposited onto planar bulk GaN layers to characterize the thickness of deposited films and optimize deposition conditions. Concentrations of 2, 10 and 20mg/ml of F8BT in toluene were deposited on to GaN layers and spin coated at a rotation speed of 4000rpm for 30s. The films were then mechanically scratched with a scalpel to selectively remove the dried F8BT film and create a step to the GaN for the profile thickness to be measured by AFM. Figure 5.5 shows SEM and AFM measurements of the sample with F8BT deposited from the 20mg/ml toluene solution. The results of the thickness measurements are shown in Table 5.1. Following this work, concentrations of between 10 and 20mg/ml were used. In order to increase thickness, multiple depositions of these concentrations were used.

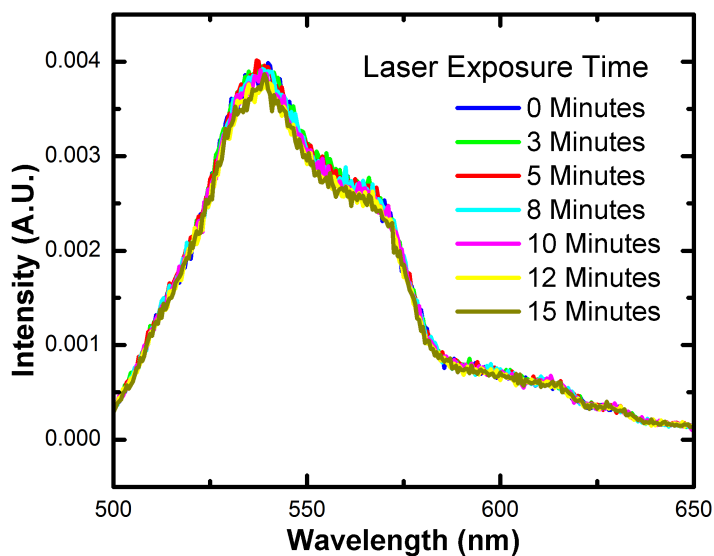


Figure 5.4: Photoluminescence of an F8BT film deposited on a single GaN layer on sapphire measured at intervals of 2 – 3 minutes with constant laser exposure. The F8BT film was deposited in a glovebox environment with  $O_2$  levels  $< 0.5\text{ppm}$ , PL measurement was carried out in a vacuum of ( $10^{-6}\text{Torr}$ ), excitation is with a 375nm laser diode operating at 4mW power in CW mode. No evidence of degradation is observed

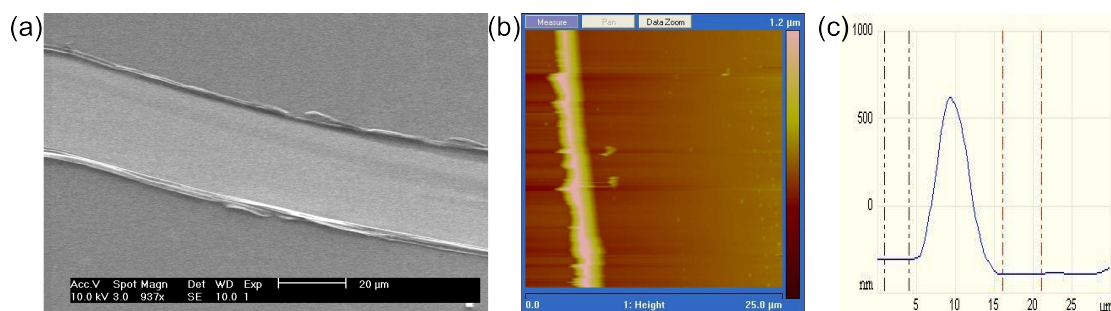


Figure 5.5: (a) SEM image of a scratched F8BT film deposited on GaN from a solution of F8BT in toluene with a concentration of 20mg/ml (b) AFM image of the same sample (c) AFM profile measurement used to determine the film thickness

Concentration	Film Thickness
2mg/ml	13nm
10mg/ml	50nm
20mg/ml	85nm

Table 5.1: The thickness of F8BT films spin coated onto GaN from toluene solutions of various concentrations measured by AFM

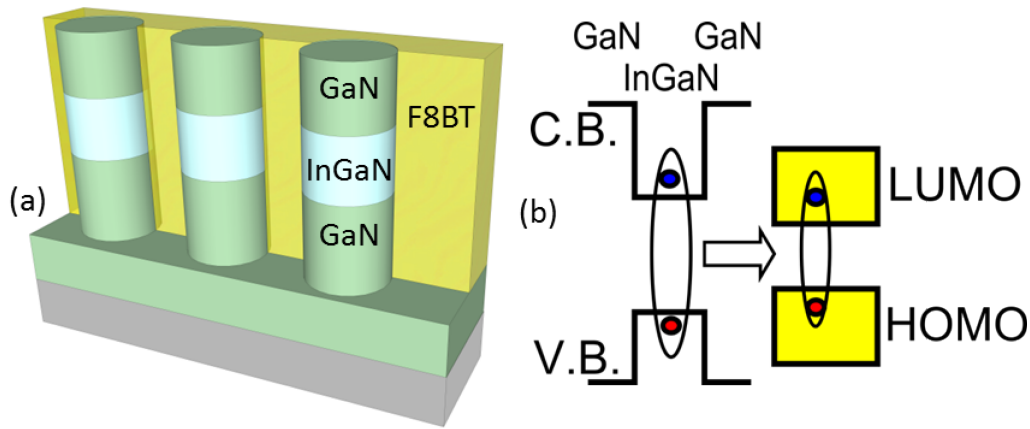


Figure 5.6: (a) a schematic of the hybrid InGaN/GaN MQW nanorod / F8BT structure fabricated, the F8BT is deposited directly onto the nanorod array, minimizing MQW-F8BT separation. (b) This allows for the possibility of FRET between MQW and light emitting polymer.

## 5.3 Hybrid Structures

### 5.3.1 Hybrid Organic/Inorganic Nanorod White Emitting Structures Using FRET

In order to utilize non-radiative energy transfer with InGaN/GaN MQWs and minimize the separation between MQW and organic excitons, the InGaN/GaN nanorod array structures described at the beginning of this chapter have been used as the base for hybrid structures. This novel structure combines the benefits of strain reduced, higher efficiency InGaN/GaN MQW nanorods with the high non-radiative energy transfer rates possible with low exciton separation. A schematic of the hybrid structures fabricated is shown in Figure 5.6. F8BT was spin coated onto III-nitride nanorods with different etch depths before the samples were cleaved to take cross-sectional SEM images to check the ability of the F8BT to coat the nanorod sidewalls. Figure 5.7 shows the cross-sectional SEM images of samples with two different etch depths, 400 and 800nm. It was found that the shallow etched nanorods were prone to the formation of voids beneath the F8BT leading to uncoated sidewalls (which would increase exciton separation, prohibiting FRET). The deeper etched nanorods showed a good, uniform coating of F8BT with the entire nanorod sidewalls coated.

For hybrid structures, InGaN/GaN MQW samples were grown on double side polished c-plane sapphire substrates by MOCVD using the procedure described previously. An aluminium nitride buffer was grown on the sapphire wafer followed by an unintentionally doped  $1\mu\text{m}$  gallium nitride layer. Five periods of InGaN quantum well and GaN barrier (2nm/9nm) were grown with a top 10nm GaN capping layer. Nanorod arrays were fabricated using the InGaN MQW as-grown wafer with the self-assembly, post growth process described earlier. This processing yields a self-assembled nanorod array with typical nanorod diameters of 220nm. Two samples were fabricated, one sample was left

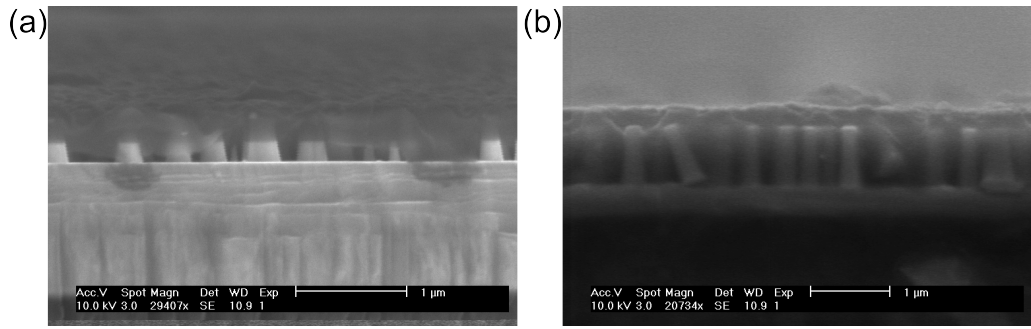


Figure 5.7: (a) SEM cross-sectional image of an F8BT coated nanorod array with nanorod etching depth of 400nm, It is clear that the F8BT is not in contact with the entire nanorod sidewall and that voids are present at the base of the nanorods (b) F8BT coated Nanorods with an etch depth of 800nm showing complete coverage by the F8BT over the entire nanorod sidewalls

as a bare MQW nanorod array while a second sample was used to form a hybrid structure. F8BT processing was carried out in a glovebox with oxygen levels  $< 0.5\text{ppm}$  to avoid possible photo-oxidation. The F8BT was dissolved in toluene to form a solution of 10mg/ml concentration, this was then spin coated onto the surface of the nanorod array structures four times to form a thick layer of F8BT that covers the top of the nanorods while also being in contact with the nanorod sidewalls.

Samples were transferred to an optical cryostat where they were held at a vacuum of  $10^{-6}$  Torr during all optical measurements to reduce the possibility of photo-oxidation. Room temperature PL measurements were carried out using a 375nm laser diode to selectively excite InGaN MQWs as the energy is below the GaN bandgap. The samples were excited from the substrate side, with the laser passing through the polished sapphire base and into the nanorods to avoid the laser having to pass through a thick layer of F8BT before reaching MQWs. The emission was also collected from the underside. The bare MQW nanorod and hybrid samples room temperature PL is shown in Figure 5.8. So far, during this initial stage of research no attempts have been made to optimize the colour matching of the hybrid sample, however it is still clear that the hybrid emission spectrum covers blue from MQW and yellow from the F8BT, closely resembling the output of a commercial phosphor converted LED. The MQW peak centred at 450nm shows significant quenching (64%) from bare MQW NR to hybrid, this is expected to be as a result of the non-radiative energy transfer from MQW to F8BT. In order to investigate the non-radiative energy transfer further, TRPL measurements were used to examine the recombination dynamics of MQW excitons in these two samples. Time correlated single photon counting was used to measure the TRPL of the MQWs. In order to examine the decay dynamics of the MQWs the monochromator was set to the PL peak of the MQWs (450nm). The MQW decay was fitted with a bi-exponential function. At room temperature, both samples showed  $A_1 > A_2$  meaning that  $\tau_1$  can again be taken as the representative decay lifetime  $\tau_{pl}$ . The TRPL measurements were carried out under a low excitation power density regime to ensure MQW decay is dominated by excitonic recombination processes

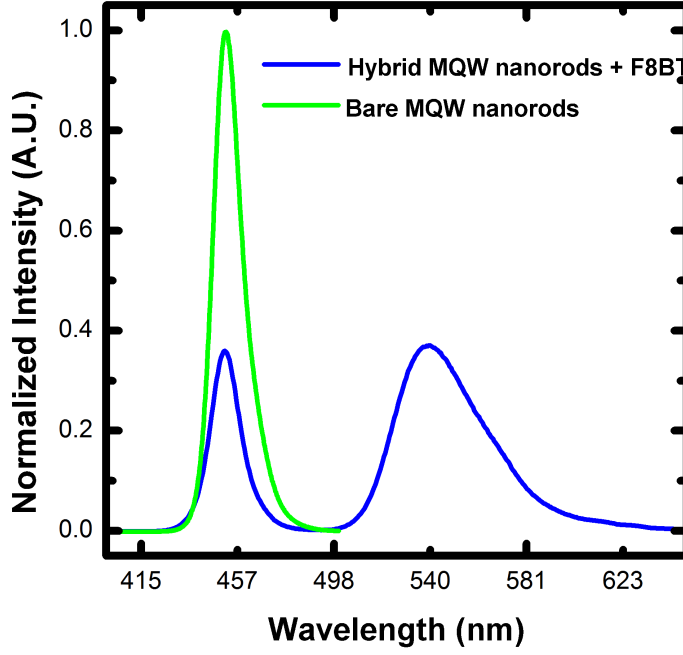


Figure 5.8: Photoluminescence spectra of the MQW emission peak of a bare InGaN/GaN MQW nanorod sample with the corresponding hybrid MQW nanorod sample with an overlayer of F8BT

without carrier screening associated with high power densities.

The decay dynamics of MQW excitons are changed in the hybrid sample with FRET coupling. In the bare MQW nanorod sample, the decay rate ( $k$ ) is determined by Equation 5.2 where the decay rate is the reciprocal of the lifetime as in Equation 5.3.

$$k_{MQW} = k_r + k_{nr} \quad (5.2)$$

$$k = \frac{1}{\tau} \quad (5.3)$$

Where  $k_{MQW}$ ,  $k_r$  and  $k_{nr}$  are total, radiative and non-radiative decay rates of the MQW respectively. In the case of the hybrid MQW nanorod sample, an additional non-radiative decay channel is added for excitons non-radiatively transferring their energy to F8BT excitons. In the hybrid sample the MQW decay rate is modified to Equation 5.4 where  $k_{hyb}$  is the modified MQW decay rate in the hybrid sample and  $k_{ET}$  is the energy transfer rate.

$$k_{hyb} = k_r + k_{nr} + k_{ET} \quad (5.4)$$

The TRPL traces for the MQW emission from both the bare MQW nanorod and the hybrid nanorod samples are shown in figure 3. Taking  $\tau_1$  as the representative decay lifetime, the decay from the hybrid MQW,  $\tau_{hyb} = 2.5\text{ns}$ , is significantly faster than the decay lifetime of the bare MQW nanorods,  $\tau_{MQW} = 3.7\text{ns}$ . These values correspond



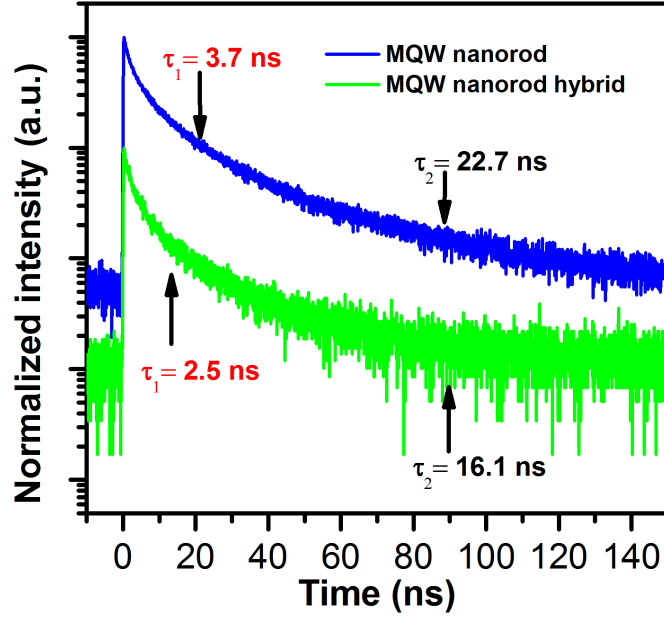


Figure 5.9: The TRPL decay traces of the bare MQW nanorod sample and the MQW nanorod hybrid sample. The detection wavelength is the MQW emission peak

to decay rates of  $k_{hyb} = 0.4\text{ns}^{-1}$  and  $k_{MQW} = 0.27\text{ns}^{-1}$  giving an energy transfer rate of  $k_{ET} = 0.13\text{ns}^{-1}$ . This allows the calculation of the efficiency of the energy transfer process given by Equation 5.5 from[26], leading to an efficiency of  $\eta_{ET} = 33\%$ , this value does not however take into account the fact that the typical nanorod diameter is significantly larger than the short range of the FRET process. With the assumption that the lifetime of the entire MQW region is modified by the presence of the F8BT, where in this case the measured lifetime of the MQW contains both modified and un-modified from different regions of the nanorods (sidewalls, centres).

$$\eta_{ET} = \frac{k_{ET}}{k_{ET} + k_{MQW}} \quad (5.5)$$

The geometry of the dimensionality of structures the donor and acceptor excitons exist in has been shown to have a significant effect on the dependence of FRET with exciton separation. From the localized molecular dipoles of the original work by Förster with an inverse  $6^{th}$  power dependence[10] to the inverse  $4^{th}$  power dependence of a quantum well to quantum dot[16] and the inverse square dependence of two separated two-dimensional films[14]. This dependence was formalized by Hernandez et al. examining the dependence on dimensionality from quantum dots, quantum wires and quantum wells[27]. Many other factors determine the energy transfer range such as dipole orientations and ordering[14], exciton localization[26], the wave vectors of MQW Wannier-Mott excitons and dielectric properties of any barrier materials between MQW and polymer excitons[28]. The exact nature of all of these factors in these novel nanostructures with complex geometries is yet to be determined. The upper limit of FRET range is generally

found to be in the order of 5-10nm [28, 29], based on the reports from literature. Taking an upper limit of the range of FRET as 10nm, it is reasonable to consider the nanorod structures in terms of two regions, an outer region where MQW/F8BT exciton separation is within 10nm where FRET is possible and an inner region where the separation is greater than 10nm leading to negligible possibility of FRET taking place, shown schematically in Figure 5.10. If the relative volume contributions of these regions are corrected for, it is possible to determine the energy transfer rate from this outer region of the nanorods as the only contributor to the change in MQW lifetime. The relative volume leads to a correction factor of 5.76 giving a corrected energy transfer rate of  $k_{ET} = 0.76\text{ns}^{-1}$ . This value then gives a FRET efficiency of 73% where only the outer 10nm of a typical nanorod contributes to FRET. This gives a picture of a structure where the nanorod centres contribute relatively unchanged MQW recombination processes emitting blue light with a high efficiency and outer layers of the nanorods where MQW recombination is dominated by a high speed energy transfer from MQW to F8BT leading to yellow emission.

It is possible to calculate the radiative and non-radiative decay rates ( $k_r$  and  $k_{nr}$ ) in the MQW nanorod structure by using the room temperature internal quantum efficiency (IQE) of the MQW determined by the ratio of the integrated PL intensity of the MQW nanorods at low temperature (12K) and room temperature (300K). Using Equations 3.1 and 5.6.

$$\eta_{IQE} = \frac{1}{1 + \frac{\tau_r}{\tau_{nr}}} \quad (5.6)$$

The values of the radiative and non-radiative rates in the MQW nanorod structure are calculated as  $k_r = 0.01 \text{ ns}^{-1}$  and  $k_{nr} = 0.26 \text{ ns}^{-1}$  respectively. Comparing these values with the non-radiative energy transfer rate in the outer 10nm of the hybrid MQW nanorods of  $k_{ET} = 0.76 \text{ ns}^{-1}$  highlights the dominance of the non-radiative energy transfer mechanism in the strong FRET region of the hybrid samples. As  $k_{ET} > k_{nr}$ , carriers that otherwise would have decayed non-radiatively in the MQW are now more likely to undergo fast non-radiative energy transfer to the light emitting polymer leading to lower overall non-radiative recombination losses in the device and therefore higher device efficiencies.

To confirm the nature of the additional non-radiative mechanism found in the MQW of the hybrid sample, a further set of samples was fabricated using green emitting (530nm) InGaN/GaN MQW nanorod arrays. Again, one sample was left as a bare MQW nanorod structure while another had F8BT deposited on the surface to cover the nanorod array. With these samples the spectral overlap of MQW emission and F8BT absorption is very low, as seen in Figure 5.11, giving only negligible probability of FRET. This allows us to rule out any non-radiative recombination processes that could take place at the surface of the MQW sidewall due to the presence of F8BT. The MQW decay dynamics were measured for this additional set of samples (Figure 5.12) and after fitting showed no significant change in MQW decay lifetime as a result of surface effects at the InGaN/F8BT

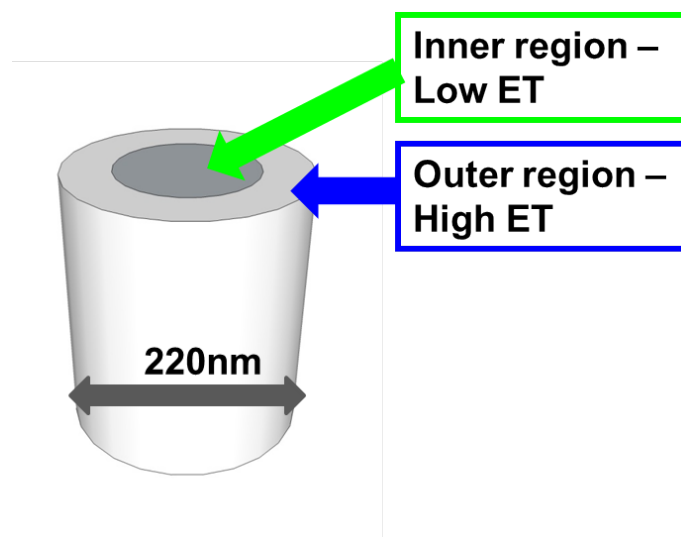


Figure 5.10: A schematic showing a nanorod of typical diameter 220nm with an outer radius where NRET is possible and an inner radius where the separation between MQW excitons and the F8BT surrounding the nanorod is too large to allow NRET

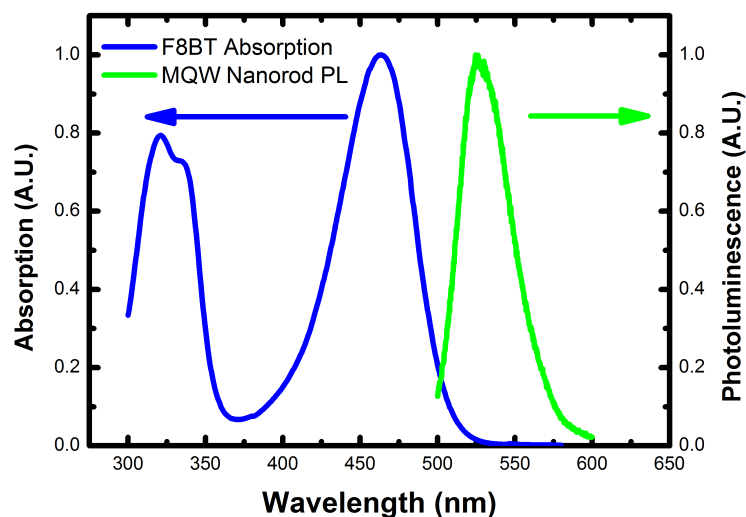


Figure 5.11: The absorption spectrum of an F8BT film and the PL emission of the green emitting MQW nanorods, The overlap of emission and absorption is very low, leading to low resonance and therefore low probability of FRET.

interface. This supports the conclusion that the significant reduction in carrier lifetime seen in the blue emitting MQW nanorod hybrid samples is due to non-radiative energy transfer to the F8BT layer as opposed to any other effect of the F8BT coating.

In-order to produce white luminescence , both the emission from the blue emitting In-GaN quantum wells and the longer wavelength down-converted emission from the polymer material must be present and the relative contributions must be balanced to control the CRI. This has not been the case in some of the demonstrations of device structures employing FRET from literature, where the MQW luminescence is significantly quenched[22]. The benefit of the hybrid MQW/F8BT structures demonstrated here is

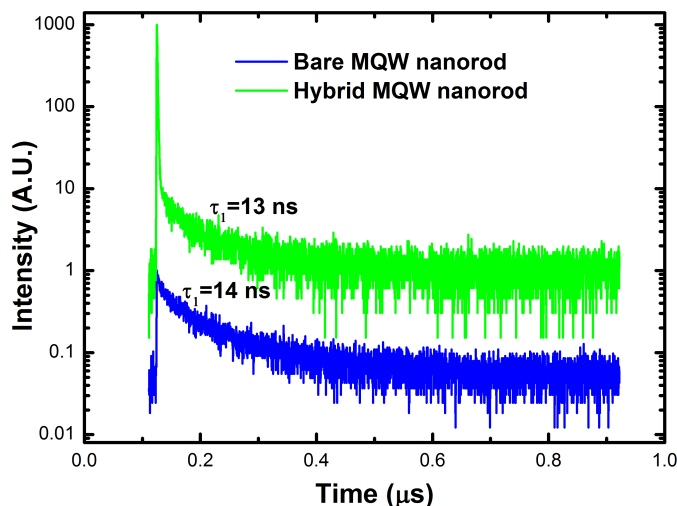


Figure 5.12: The TRPL decay traces of the bare green emitting MQW nanorod sample and the green emitting MQW nanorod hybrid sample. The detection wavelength is the MQW emission peak. The overlapping F8BT decay trace has been removed in the fitting process

that with the FRET process dominating recombination of carriers on the edge of the nanorods and MQW recombination dynamics not significantly changed in the centres of the nanorods, both blue and yellow luminescence are possible in these structures. Confocal PL mapping was carried out on hybrid structures to examine the distribution of blue and yellow luminescence. Figure 5.13 shows integrated PL intensity maps of the emission of the MQW (a) and the F8BT emission (b). Both images are taken from a map of the same area but differ only in the range of the spectral integration. It is clear that the MQW emission in (a) is localized to emission from the InGaN MQW nanorods with typical diameters of 220nm. The F8BT emission is spatially inverse to this, weak at the position of the nanorods and strong in the areas surrounding the nanorods. This distribution of blue and yellow emission demonstrates the potential for such hybrid structures to generate white light.

## 5.4 Summary

In conclusion, novel hybrid InGaN/GaN MQW nanorod structures coated with F8BT have been fabricated to produce white light emission. Combining high efficiency blue emission from the nitride based materials with high efficiency non-radiative energy transfer to an organic light emitter. This approach to utilizing the non-radiative energy transfer mechanism does not sacrifice the performance of the InGaN blue emitter. The ultra-low separation hybrid interface allows for extremely fast non-radiative energy transfer processes to take place and the hybrid structures show clear evidence of non-radiative energy transfer in the reduced MQW exciton recombination lifetimes. The efficiency of

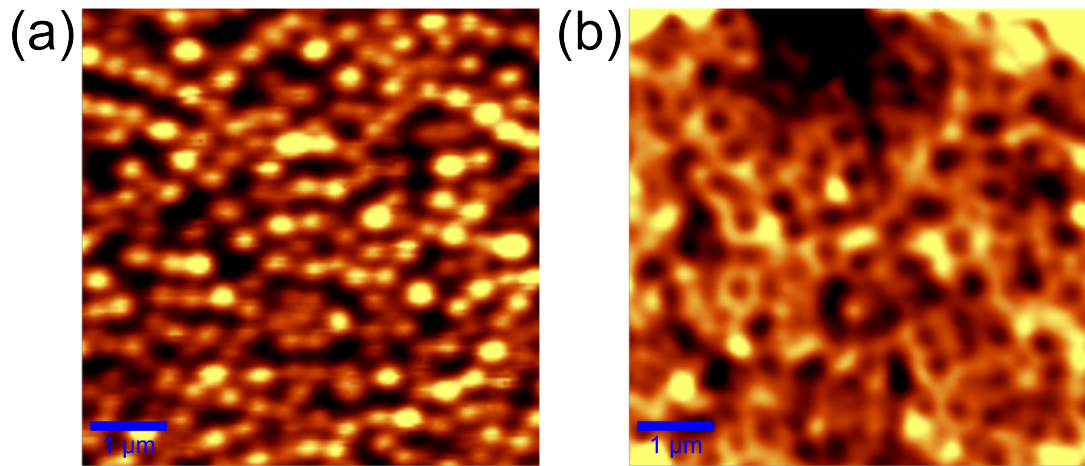


Figure 5.13: Confocal photoluminescence maps showing integrated PL intensity of both the MQW emission (a) and the F8BT emission (b). A clear segregation is visible with the MQW emission localized to the MQE nanorods and F8BT emission the inverse of this.

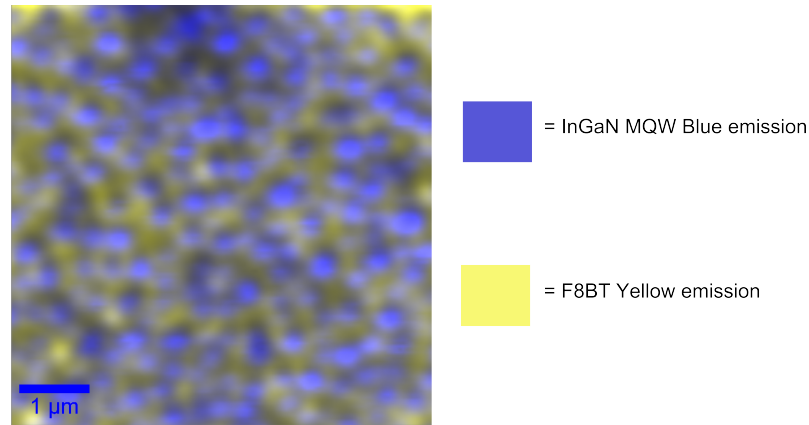


Figure 5.14: An overlay of the confocal PL mapping of the integrated PL intensities of InGaN blue MQW emission (Blue) and F8BT yellow emission (Yellow). Showing the mixture of blue and yellow luminescence

the FRET process was found to be 73% in the outer 10nm of the InGaN MQW nanorods after considering a simple static two region model. The non-radiative energy transfer rate in the coupled region of the MQW nanorods calculated as  $k_{ET} = 0.76\text{ns}^{-1}$ , dominating the MQW non-radiative decay rate of  $k_{MQW} = 0.26\text{ns}^{-1}$ . This demonstrates the potential of devices based on this novel structure to exhibit increased total device efficiencies over more conventional phosphor converted planar LED devices.

## References

- <sup>1</sup>H. P. T. Nguyen, K. Cui, S. Zhang, M. Djavid, A. Korinek, G. a. Botton, and Z. Mi, “Controlling electron overflow in phosphor-free InGaN/GaN nanowire white light-emitting diodes.”, *Nano letters* **12**, 1317–23 (2012).
- <sup>2</sup>S. Li and A. Waag, “GaN based nanorods for solid state lighting”, *Journal of applied physics* **111**, 071101 (2012).

- <sup>3</sup>S. Guha, R. A. Haight, N. A. Bojarczuk, and D. W. Kisker, “Hybrid organic-inorganic semiconductor-based light-emitting diodes”, *Journal of applied physics* **82**, 4126 (1997).
- <sup>4</sup>F. Hide, P. Kozodoy, S. P. DenBaars, and A. J. Heeger, “White light from InGaN/conjugated polymer hybrid light-emitting diodes”, *Applied physics letters* **70**, 2664 (1997).
- <sup>5</sup>G. Heliotis, P. N. Stavrinou, D. D. C. Bradley, E. Gu, C. Griffin, C. W. Jeon, and M. D. Dawson, “Spectral conversion of InGaN ultraviolet microarray light-emitting diodes using fluorene-based red-, green-, blue-, and white-light-emitting polymer overlayer films”, *Applied physics letters* **87**, 103505 (2005).
- <sup>6</sup>G. Heliotis, G. Itkos, R. Murray, M. Dawson, I. Watson, and D. Bradley, “Hybrid Inorganic/Organic Semiconductor Heterostructures with Efficient Non-Radiative Energy Transfer”, *Advanced materials* **18**, 334–338 (2006).
- <sup>7</sup>K. Ema, M. Inomata, Y. Kato, H. Kunugita, and M. Era, “Nearly Perfect Triplet-Triplet Energy Transfer from Wannier Excitons to Naphthalene in Organic-Inorganic Hybrid Quantum-Well Materials”, *Physical review letters* **100**, 257401 (2008).
- <sup>8</sup>H. Nakanotani, K. Masui, J. Nishide, T. Shibata, and C. Adachi, “Promising operational stability of high-efficiency organic light-emitting diodes based on thermally activated delayed fluorescence.”, *Scientific reports* **3**, 2127 (2013).
- <sup>9</sup>G. Itkos, C. R. Belton, G. Heliotis, I. M. Watson, M. D. Dawson, R. Murray, and D. D. C. Bradley, “White light emission via cascade Förster energy transfer in (Ga, In)N quantum well/polymer blend hybrid structures.”, *Nanotechnology* **20**, 275207 (2009).
- <sup>10</sup>T. Förster, “Energiewanderung und Fluoreszenz”, *Die naturwissenschaften* **33**, 166–175 (1946).
- <sup>11</sup>R. M. Clegg, “Forster resonance energy transfer-FRET what is it, why do it, and how it’s done”, in *Fret and flim techniques*, Vol. 33, edited by T. Gadella, 1st edition (Elsevier B.V., 2009), pages 1–57.
- <sup>12</sup>D. Andrews, “A unified theory of radiative and radiationless molecular energy transfer”, *Chemical physics* **135**, 195–201 (1989).
- <sup>13</sup>D. L. Andrews and D. S. Bradshaw, “Virtual photons, dipole fields and energy transfer: a quantum electrodynamical approach”, *European journal of physics* **25**, 845–858 (2004).
- <sup>14</sup>J. Hill, S. Heriot, O. Worsfold, T. Richardson, A. Fox, and D. Bradley, “Controlled Förster energy transfer in emissive polymer Langmuir-Blodgett structures”, *Physical review b* **69**, 041303 (2004).
- <sup>15</sup>D. Basko, G. La Rocca, F. Bassani, and V. Agranovich, “Förster energy transfer from a semiconductor quantum well to an organic material overlayer”, *The european physical journal b* **8**, 353–362 (1999).
- <sup>16</sup>M. Achermann, M. a. Petruska, S. Kos, D. L. Smith, D. D. Koleske, and V. I. Klimov, “Energy-transfer pumping of semiconductor nanocrystals using an epitaxial quantum well.”, *Nature* **429**, 642–6 (2004).

- <sup>17</sup>M. Achermann, M. a. Petruska, D. D. Koleske, M. H. Crawford, and V. I. Klimov, “Nanocrystal-based light-emitting diodes utilizing high-efficiency nonradiative energy transfer for color conversion.”, *Nano letters* **6**, 1396–400 (2006).
- <sup>18</sup>S. Chanyawadee, P. G. Lagoudakis, R. T. Harley, M. D. B. Charlton, D. V. Talapin, H. W. Huang, and C.-H. Lin, “Increased color-conversion efficiency in hybrid light-emitting diodes utilizing non-radiative energy transfer.”, *Advanced materials (deerfield beach, fla.)* **22**, 602–6 (2010).
- <sup>19</sup>C. R. Belton, G. Itskos, G. Heliotis, P. N. Stavrinou, P. G. Lagoudakis, J. Lupton, S. Pereira, E. Gu, C. Griffin, B. Guilhabert, I. M. Watson, a. R. Mackintosh, R. a. Pethrick, J. Feldmann, R. Murray, M. D. Dawson, and D. D. C. Bradley, “New light from hybrid inorganic-organic emitters”, *Journal of physics d: applied physics* **41**, 094006 (2008).
- <sup>20</sup>H. V. Demir, S. Nizamoglu, T. Erdem, E. Mutlugun, N. Gaponik, and A. Eychmüller, “Quantum dot integrated LEDs using photonic and excitonic color conversion”, *Nano today* **6**, 632–647 (2011).
- <sup>21</sup>G. Heliotis, E. Gu, C. Griffin, C. W. Jeon, P. N. Stavrinou, M. D. Dawson, and D. D. C. Bradley, “Wavelength-tunable and white-light emission from polymer-converted micropixelated InGaN ultraviolet light-emitting diodes”, *Journal of optics a: pure and applied optics* **8**, S445–S449 (2006).
- <sup>22</sup>S. Nizamoglu, B. Guzelturk, D.-W. Jeon, I.-H. Lee, and H. V. Demir, “Efficient nonradiative energy transfer from InGaN/GaN nanopillars to CdSe/ZnS core/shell nanocrystals”, *Applied physics letters* **98**, 163108 (2011).
- <sup>23</sup>M. Campoy-Quiles, G. Heliotis, R. Xia, M. Ariu, M. Pintani, P. Etchegoin, and D. D. C. Bradley, “Ellipsometric Characterization of the Optical Constants of Polyfluorene Gain Media”, *Advanced functional materials* **15**, 925–933 (2005).
- <sup>24</sup>V. N. Bliznyuk, S. A. Carter, J. C. Scott, G. Klärner, R. D. Miller, and D. C. Miller, “Electrical and Photoinduced Degradation of Polyfluorene Based Films and Light-Emitting Devices”, *Macromolecules* **32**, 361–369 (1999).
- <sup>25</sup>L. Romaner, A. Pogantsch, P. Scandiucci de Freitas, U. Scherf, M. Gaal, E. Zojer, and E. List, “The Origin of Green Emission in Polyfluorene-Based Conjugated Polymers: On-Chain Defect Fluorescence”, *Advanced functional materials* **13**, 597–601 (2003).
- <sup>26</sup>J. Rindermann, G. Pozina, B. Monemar, L. Hultman, H. Amano, and P. Lagoudakis, “Dependence of Resonance Energy Transfer on Exciton Dimensionality”, *Physical review letters* **107**, 236805 (2011).
- <sup>27</sup>P. L. Hernandez-Martinez, A. O. Govorov, and H. V. Demir, “Generalized Theory of Forster-Type Nonradiative Energy Transfer in Nanostructures with Mixed Dimensionality”, *The journal of physical chemistry c* **117**, 10203–10212 (2013).
- <sup>28</sup>V. M. Agranovich, Y. N. Gartstein, and M. Litinskaya, “Hybrid resonant organic-inorganic nanostructures for optoelectronic applications.”, *Chemical reviews* **111**, 5179–214 (2011).

<sup>29</sup>S. Blumstengel, S. Sadofev, C. Xu, J. Puls, and F. Henneberger, “Converting Wannier into Frenkel Excitons in an Inorganic/Organic Hybrid Semiconductor Nanostructure”, *Physical review letters* **97**, 237401 (2006).



---

# Exciton Localization and its Effect on Non-radiative Energy Transfer in III-Nitride based Organic/Inorganic Hybrids

---

Utilizing the self-assembly post growth technique for nanorod fabrication as shown in the previous chapter, it is possible to effectively generate non-radiative energy transfer coupling from InGaN/GaN MQWs to a light emitting polymer. It is expected that exciton localization of InGaN/GaN quantum wells significantly affects the carrier recombination of InGaN based LEDs. As FRET is a direct exciton coupling, these localization effects also have the potential to influence FRET and the behaviour of hybrid structures. As will be shown in this chapter, temperature dependent PL and temperature dependent TRPL measurements are performed on InGaN/GaN MQW nanorods coated with F8BT in order to investigate the effect of exciton dimensionality on FRET coupling in the hybrid organic/inorganic light emitting structures described in the previous chapter.

### **6.1 Localization Effects in III-Nitride Materials**

As discussed in Chapter 4, exciton localization is not only strong in InGaN alloys, but also is responsible for the high performance of InGaN based LEDs despite there is a high density of defects still present in hetero-epitaxial III-nitride materials[1–4]. In spite of the importance of exciton localization in InGaN alloy, there is still ongoing debate about the dominant causes of localization in InGaN alloy. Inhomogeneity in InGaN alloys through the formation of indium nitride rich clusters has been observed by transmission electron microscope (TEM), reported by several independent researchers using TEM and other techniques such as Raman optical techniques[1, 5–7].The clustering of InN rich regions in InGaN leads to some regions where the local bandgap energy is reduced due

to the higher mole fraction of InN. These narrower bandgap clusters have been generally accepted to localize excitons away from non-radiative recombination centres, such as threading dislocations.

However, it is worth noting that there exist some different views on the formation mechanism of exciton localization, studied by TEM. It is true that electron beams can cause some damage during the TEM measurements, leading to the appearance of some In clustering if the electron dose used is too high. Our group and also another group have reported that the In clustering can be generated during the TEM measurements. However, it does not simply exclude the existence of In segregation in InGaN alloy. In any way, the indium segregation or so-called phase separation depends on indium content, the higher the indium content, the more easily indium segregation appears. Furthermore, the indium segregation also depends on InGaN thickness and growth conditions for InGaN.

As discussed in Chapter 4, there are several features of the photoluminescence from InGaN/GaN quantum wells that displays inhomogeneity and the presence of localized states in InGaN quantum wells, such as the broad PL spectra of InGaN quantum wells and the "s-shift" in temperature dependent PL indicating redistribution between localized states. Sub-wavelength resolved micro PL measurements were conducted by Schomig et al. in order to probe emission from individual localization centres in InGaN quantum wells[8]. Extremely narrow linewidths of the PL of individual localization centres were observed down to 0.8meV.

## 6.2 Energy Transfer Dependence on Localization

In 1999 Basko et al. developed a theoretical description of FRET between an inorganic quantum well and an organic material film deposited on top of the inorganic structure, where the difference between energy transfer for free and localized excitons was considered[9]. This study was limited to the linear case, the equivalent of low carrier densities where the carrier dynamics are not complicated by many body effects such as carrier scattering. The calculations of FRET were based on the joule losses of the polarization field of the quantum well dipole with penetration into the organic material which is proportional to the imaginary part of the dielectric function of the organic material. In the case of the free excitons, Equation 6.1 is used to describe the coupling between dipoles in two planes.

$$V(k, z) \propto ke^{-kz} \quad (6.1)$$

Where  $V(k, z)$  is the dipolar coupling strength,  $k$  is the in-plane exciton wavevector, and  $z$  is the out of plane separation between the quantum well and organic material planes. The equation clearly indicates that for small and large values of wavevector the FRET coupling strength is low with maximum FRET at an intermediate value of  $k$ . Basko et al. then continued to examine the FRET process of localized excitons in the quantum well, and proposed that the in-plane wavevector is no-longer a plane-wave as the carriers

are modified by a random potential due to fluctuations in alloy composition or quantum well width. The nature of the change in FRET behaviour was found to be dependent on the localization length scale where the energy transfer lifetime is proportional to  $L^2$  where  $L$  is the localization length in the case where  $L \ll L_b$  where  $L_b$  is the quantum barrier length (the out of plane separation of organic and inorganic excitons). Where for  $L \gg L_b$  the energy transfer lifetime is proportional to  $L^{-1}$ .

The original description of FRET by Förster does not exhibit intrinsic temperature dependence[10, 11]. However, the excitonic properties of inorganic semiconductors such as III-nitrides sensitively depends on temperature, for instance, the IQE of InGaN quantum wells. As was shown in Chapter 4, the IQE of InGaN MQWs drops with increasing temperature due to the thermally induced de-localization of carriers from potential fluctuations, leading to increased non-radiative recombination. From Equation 6.2, the original derivation of FRET rate has a dependence on  $Q_D$ , the quantum yield of the energetic donor (in this case the InGaN quantum well).

$$k_t \propto \left( \frac{R_0}{r_{DA}} \right)^6 \quad (6.2)$$

Where  $R_0^6 \propto Q_D$  and the quantum yield depends on the radiative and non-radiative recombination lifetimes of the carriers in the quantum well, and as the non-radiative recombination rate increases with temperature, it would be expected that the FRET rate would decrease with increasing temperature. The temperature dependence of FRET from an InGaN quantum well as energetic donor is likely to exhibit a change to this temperature dependence as the thermally activated de-localization of excitons in InGaN quantum wells not only changes the quantum yield of the quantum well, but also the exciton wavevectors will be changed for localized or free excitons. The temperature dependence of FRET using an InGaN quantum well as energetic donor was observed using colloidal quantum dots[12] and a light emitting polymer[13]. In both of these studies an increase in FRET rate with increasing temperature was found in temperature ranges below room temperature (25 – 200K and 8 – 75K respectively). In these studies, the exact nature of the temperature dependence was not probed but the departure from the expected quantum yield dependent reduction in FRET rate with temperature, highlighting that the change in localization of quantum well excitons plays an important role. Rindermann et al. used Equation 6.1 investigate the influence of the changes in exciton localization on FRET rate between a GaN/AlGaIn single quantum well with a thin capping layer and a light emitting polymer layer deposited on top of the AlGaIn cap[14]. In this work, as the quantum well material is a binary compound, the local potential fluctuations were ascribed to quantum well thickness variations (as opposed to alloy compositional fluctuations reported in InGaIn quantum wells). These local potential fluctuations act as carrier localization centres that can be thermally activated at corresponding sample temperatures. The thermal distribution of localized and free excitons was is related to the localization energy and the

Image not available in electronic version.  
Please find original at citation in the text.

Figure 6.1: A figure by Rindermann et al. showing schematically the distribution of exciton wavevectors for localized and free excitons[15]

density of states of localized and free excitons shown in Figure 6.1 by Rindermann et al.[15]. Based on this argument, the FRET rate and efficiency were measured for a GaN quantum well with AlGaN barriers (a thin top AlGaN capping layer with a thickness of 4 nm) and a light emitting polymer F8BT, as a function of sample temperature. Time resolved PL techniques were used to study the change in recombination rate of the GaN quantum well due to the FRET process in hybrid samples as discussed in Chapter 5. The FRET rate was found to remain constant with temperature below 50K, where excitons are predominantly localized, the FRET rate then increased to a maximum at 130K where free excitons are thought to dominate. Finally, a slow reduction in FRET rate was observed with further increasing temperature as the exciton wavevector increases further.

### **6.3 Temperature Dependent Optical Properties of InGaN/GaN MQW Nanorods**

As discussed in Chapter 4 the optical properties of InGaN quantum wells exhibit localization related behaviour. As the excitonic localization is sensitive to temperature, it is necessary to study exciton localization dependence of FRET in hybrid InGaN/GaN MQW nanorods coated with a light emitting polymer by means of temperature dependent PL and TRPL measurements. Blue emitting InGaN/GaN MQWs were grown on c-plane sapphire substrates by our MOCVD using our high temperature AlN buffer technique, as described in the previous chapters. Following an initial surface treatment of the substrate at a high temperature under H<sub>2</sub>, an AlN buffer layer with a thickness of 100 – 500nm was directly deposited on the sapphire substrate, and then a thick GaN layer was subsequently grown at 1130°C prior to the growth of ten periods of InGaN quantum wells with GaN barriers. The typical InGaN well thickness is 2.5nm, and the GaN barrier is 10nm. The top-down self assembly Ni mask nanorod fabrication processed was then applied as described in

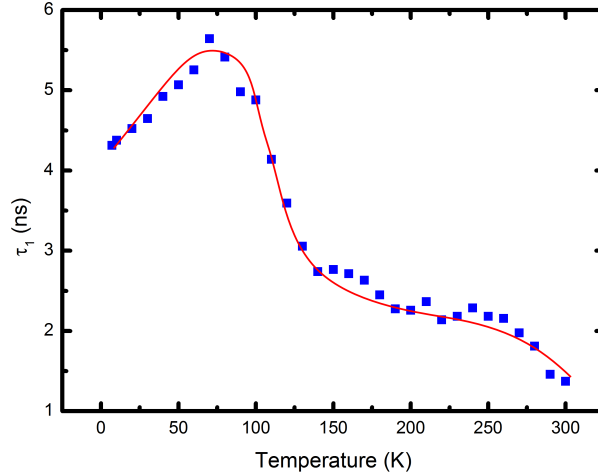


Figure 6.2: The temperature dependent recombination lifetime of InGaN/GaN MQW nanorods. The lifetime increases slightly from 10K to 70K where drops quickly until a temperature of 140K where the rate of lifetime reduction is reduced. A line to guide the eye is shown through the measured data points.

detail in Chapter 4. This resulted in InGaN/GaN MQW nanorods showing a strong PL emission at 455 nm at room temperature. For comparison, two identical nanorod samples have been prepared, one with a coating of F8BT as described in the previous chapter, another as a control, where a layer of polymethyl-methacrylate (PMMA), a transparent insulating polymer, was deposited on the nanorod surface and does not show any FRET.

TRPL measurements have been performed on the control MQW, the InGaN/GaN nanorod array with PMMA coating, the temperature dependent PL lifetime is shown in Figure 6.2 where the lifetimes are fitted based on with a standard bi-exponential function as in the previous chapter. The lifetime shows an initial increase with increasing temperature from 7K up to 70K before dropping quickly, and then decreasing at a reduced rate above 140K. As discussed in Chapter 4, the initial increase in lifetime is due to a combination of the thermalized excitons in the quantum wells[16, 17] and the redistribution to deeper localized states, leading to emission with longer wavelengths and therefore longer radiative lifetimes as a result of the polar nature of c-plane nitrides[18]. This thermally induced redistribution demonstrates the presence of localized states in the InGaN quantum wells. As temperature is further increased, the lifetime quickly drops due to the thermal activation of non-radiative recombination centres. At temperatures above  $\approx 140$ K the rate of decrease of lifetime with increasing temperature is reduced, indicating that a significant fraction of excitons are de-localized.

Temperature dependent PL measurements were carried out for the control sample to understand the localization properties of the InGaN MQWs. This allowed the determination of an activation energy related to the localization of excitons in the MQW as discussed in Chapter 4. An Arrhenius plot is presented in Figure 6.3 (a) exhibiting an activation energy, which is equivalent to a temperature of 160K. The full width at half maximum

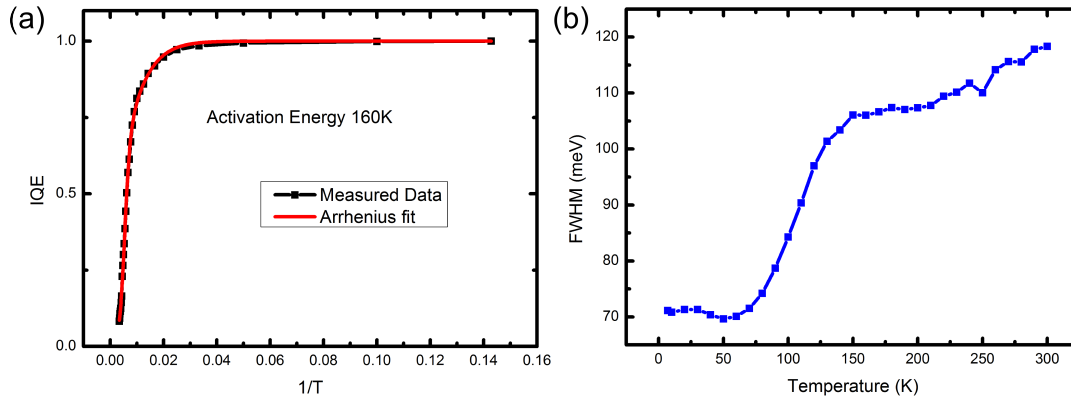


Figure 6.3: (a) an Arrhenius plot of the integrated PL intensity of the PMMA coated control InGaN/GaN MQW nanorod sample yielding an activation energy corresponding to a temperature of 160K. (b) the PL full width at half maximum values as a function of temperature, a turning point is clear at a temperature of 150K corresponding to significant degree of de-localization of excitons in the InGaN MQWs

(FWHM) of the PL emission peaks were measured as a function of temperature, given in 6.3 (b). The FWHM shows a significant increase at  $\approx 70$ K before reaching another turning point at 150K where the increase in FWHM becomes very slow. This behaviour can be understood again as a signature of localized states in the InGaN quantum well. At low temperatures excitons are trapped in localization centres. With increasing temperature, the excitons obtain enough thermal energy in order to escape the localization centres, thermalizing between localization states with different localization depths[19]. The temperatures that correspond to the activation energies obtained through the Arrhenius fitting, the FWHM temperature dependence and the TRPL lifetime temperature dependence (160K, 150K and 140K respectively) are all in reasonably good agreement, indicating that significant thermal de-localization of excitons occurs at around 150K.

## 6.4 Temperature Dependent Non-radiative Energy Transfer due to Exciton Localization

The non-radiative energy transfer between InGaN/GaN MQW nanorods and the F8BT coating has been studied using the same TRPL technique described in the previous chapter. The PL lifetimes of the hybrid sample with InGaN/GaN MQW nanorods coated with F8BT and the control sample with a PMMA coating have been measured as a function of temperature under identical conditions. The sample temperature was varied from 7 to 300K using a Janis optical cryostat. The measured TRPL data is shown in Figure 6.5 at several temperatures from 7 – 300K. After measuring TRPL, the PL decay transients were fitted based on a standard bi-exponential function and the dominant fast decay time taken as the representative PL lifetime as usual. The decay rates of the two samples are shown in Figure 6.5, where the decay rate  $k$  is the reciprocal of the exponential lifetime

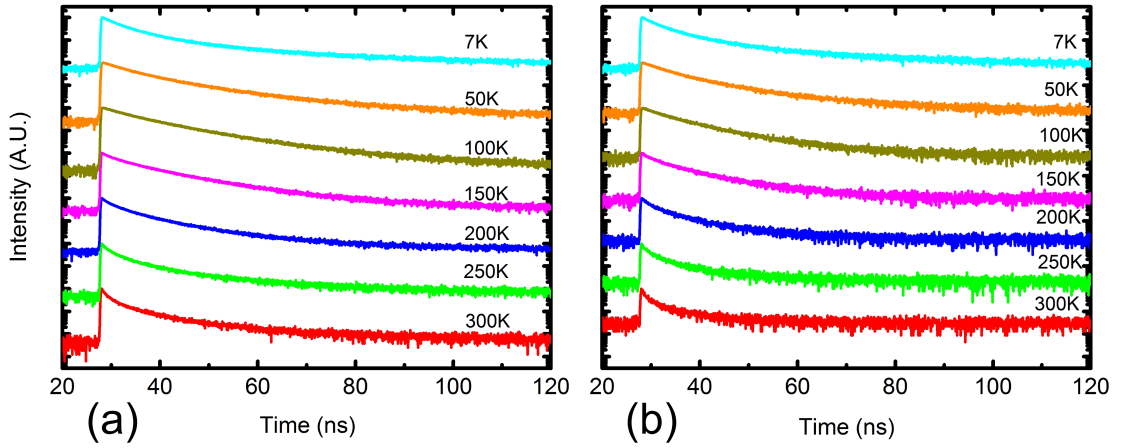


Figure 6.4: The measured TRPL decay data at various temperatures for the InGaN/GaN MQW nanorods in the control sample: PMMA coated nanorods (a) and hybrid sample: F8BT coated nanorods (b). The intensities at different temperatures have been offset for clarity.

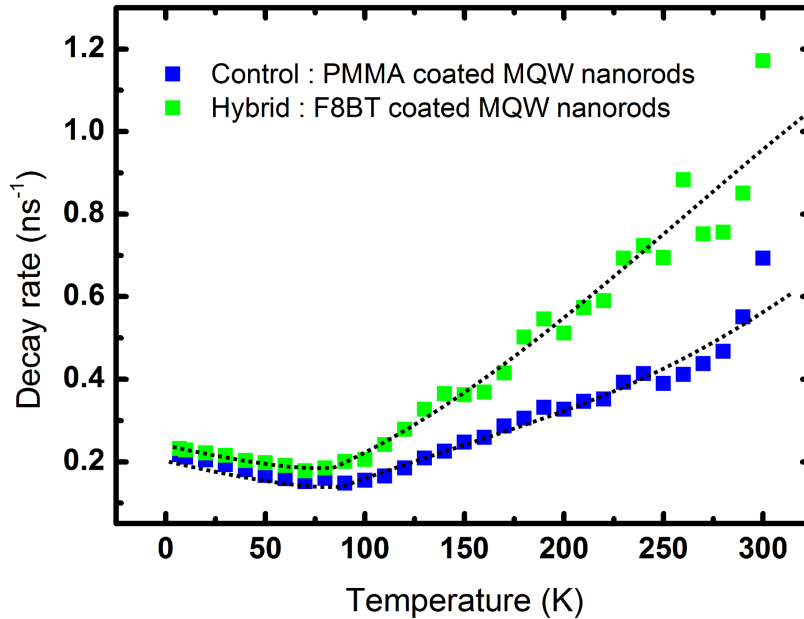


Figure 6.5: The decay rate of both PMMA coated MQW nanorod control sample and F8BT coated hybrid MQW nanorod sample as a function of temperature. A clear difference in the temperature dependence is visible at temperatures above 70K.

$k_{pl} = \frac{1}{\tau_{pl}}$ . Figure 6.5 clearly shows that the decay rate of the hybrid sample is higher than that of the control sample at all temperatures. This is expected, as was shown in the previous chapter, the hybrid sample has an additional non-radiative decay channel due to FRET, which modifies the recombination rate into  $k_{hyb} = k_r + k_{nr} + k_{ET}$ . Above 70K the difference between the hybrid and control decay rates changes significantly, where the decay rate of the hybrid sample becomes faster than that of the control sample. In order to gain better understanding of this behaviour, the non-radiative energy transfer rate

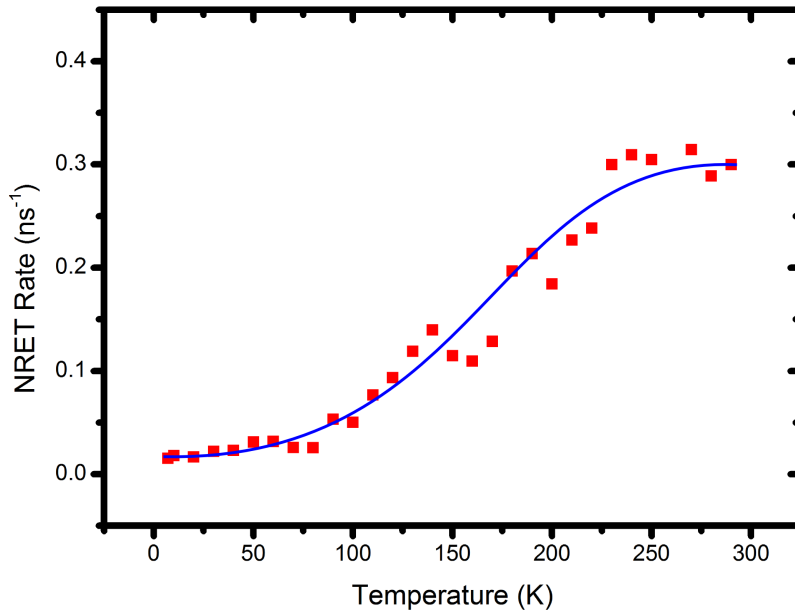


Figure 6.6: Temperature dependent non-radiative energy transfer rate. The rate is initially low until a temperature of 80K where the rate increases before saturating at a temperature of 230K. A guide for the eye is drawn through the data points.

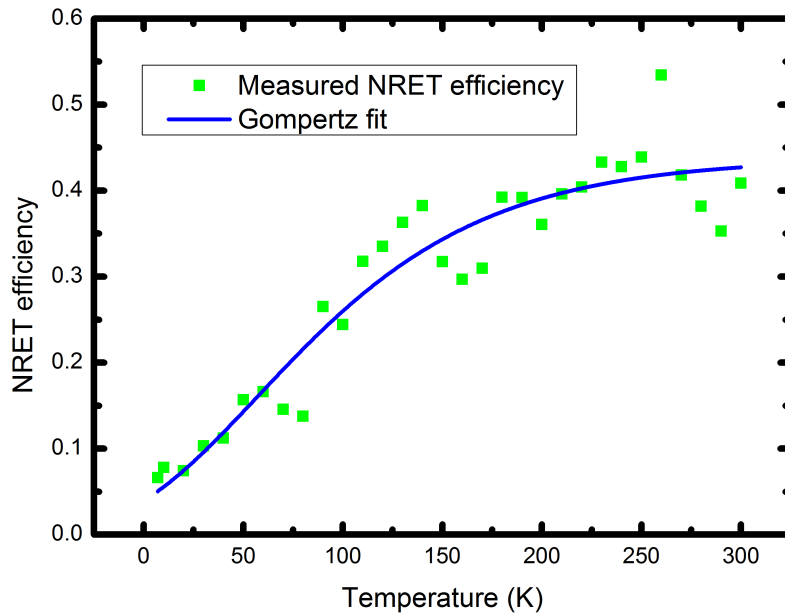


Figure 6.7: Non-radiative energy transfer efficiency as a function of temperature for hybrid nanorod samples. A sigmoidal fit is also plotted to extract a maximum gradient at a temperature of 70K corresponding to the onset of significant thermal de-localization of MQW excitons.



and efficiency were calculated from the measured decay rates of the hybrid and control samples. Using the hybrid  $k_{hyb}$  and control  $k_{MQW}$  decay rates:

$$k_{ET} = k_{hyb} - k_{MQW} \quad (6.3)$$

And:

$$\eta_{ET} = \frac{k_{ET}}{k_{ET} + k_{MQW}} \quad (6.4)$$

The energy transfer rate for the hybrid sample is plotted as a function of temperature, shown in Figure 6.6. A clear trend of increasing non-radiative energy transfer rate is visible with increasing temperature. The NRET rate stays relatively constant until a temperature of 70K where NRET rate begins to increase. At 230K the NRET rate appears to saturate. The increase in NRET rate with increasing temperature is due to the delocalization of excitons as a result of thermalization effects in the InGaN quantum wells, which leads to an increase in plane wavevector. Equation 6.1 shows that the NRET rate will increase until a certain level as the exciton wavevector increases. The relatively wide range between the onset of the increase in NRET rate and saturation (70K to 230K) can be understood based on the significant inhomogeneity of InGaN, unlike the GaN quantum well studied by Rindermann et al. [14, 15], InGaN as a ternary alloy, is subject to not only well width fluctuations but also alloy segregation as an additional localization mechanism.

The NRET efficiency obtained using Equation 6.4 is plotted as a function of temperature in Figure 6.7. The general trend in behaviour is similar to that of the NRET rate, with an increasing NRET efficiency with increasing temperature. However, it is worth highlighting that there are some differences. The NRET efficiency as a function of temperature can be empirically fit with a Gompertz sigmoidal function as described by Equation 6.5.

$$y = ae^{-e^{-k(x-x_c)}} \quad (6.5)$$

Where,  $a$  is the value of  $y$  at which it saturates,  $x_c$  is the centre value of  $x$  at which  $y = \frac{a}{e}$ . The Gompertz sigmoidal function is used to describe an exponential growth, which is limited by a factor such as a lack of resources. In this case, the NRET efficiency is related to the population of localized and de-localized excitons which is determined by the thermal energy of carriers and the distribution of localization energies in the InGaN material. This empirical fitting yields an  $x_c$  value of 70K, this temperature where the function reaches the largest gradient, which represents the de-localization of InGaN MQW excitons. This temperature correlates well with the onset of de-localization observed in the change in PL lifetime and the change in PL FWHM behaviour. As Figure 6.2 shows, 70K is the turning point at which MQW PL lifetime starts to drop due to thermal activation of non-radiative recombination centres. Further examining Figure 6.3 (b) the FWHM of the PL emission peak starts to increase significantly at around 60K. The NRET efficiency shows a saturation of the significant increase in NRET efficiency at a temperature of  $\approx 150$ K. This

temperature is in good agreement with the thermal activation energy obtained by Arrhenius plot (160K), the change in TRPL lifetime corresponding to de-localization (140K) and the plateau in FWHM at (150K). Therefore this peak in NRET efficiency clearly coincides with the thermal de-localization of MQW excitons.

There are two significant differences between the NRET rate and NRET efficiency temperature dependences: the initial behaviour at low temperatures and the saturation temperature. The initial increase in NRET efficiency occurs immediately with increasing temperature from 7K, while the NRET rate in this range remains almost constant in the same temperature range until a temperature of 80K before rising significantly with further increasing temperature. To understand this, the temperature dependent lifetime plotted in Figure 6.2 is important, showing that the lifetime of the carriers in the InGaN/GaN MQWs initially increases with temperature up to 70K as a result of the redistribution of carriers between localized states with a general move from shallow to deeper localized states, as stated previously. In this temperature range, the excitons in the InGaN MQWs are still predominantly localized. Therefore, it is expected that there is no significant change in the exciton wavevector and consequently the NRET rate is not expected to increase. Equation 6.4 shows that as the decay rate of the InGaN/GaN MQW  $k_{MQW}$  decreases, the NRET efficiency will increase and can be understood as a reduction in competition between MQW recombination processes and NRET.

The reason for the difference in the temperature at which the NRET rate and NRET efficiency saturate is less clear, there are several possible causes for this type of behaviour. It is worth noting that there are several differences between structures reported here and those reported by Rindermann et al.[14, 15]. In the case of a single quantum well with an organic overlayer, the energy transfer is simplified to that between two planes. In contrast, the hybrid structures presented here show a completely different geometry, leading to major differences in the energy transfer dynamics. The coupling between two planes given by Equation 6.1 shows the dependence on the in-plane exciton wavevector, while in our sample the quantum wells essentially appear as disks embedded in an organic medium. In this case the separation of MQW and F8BT excitons varies with in-plane propagation of the MQW excitons. As was discussed in 5, due to the short range of NRET coupling, only an outer ring of these quantum disks can contribute to NRET. Localized excitons, by their nature are fixed in position and the dimensions of this nanorod outer ring will not change. However, once excitations are thermally de-localized, they are free to move throughout the nanorod, depending on the exciton mobility. This leads to a significant change in the effective sizes of the two regions as a result of the change in exciton mobility due to thermal activation.

## 6.5 Summary

The temperature dependence of exciton localization in InGaN has been used in order to study the effect of exciton dimensionality on non-radiative energy transfer between InGaN/GaN MQW nanorods and a light emitting polymer. Temperature dependent TRPL measurements allowed to the NRET rate to be examined as a function of temperature. A pronounced increase of NRET rate and efficiency is seen with increasing temperature. The NRET efficiency was found to increase by a factor of 6.7 at room temperature (300K) in comparison to low temperature (7K). The onset of this increase in NRET rate and efficiency was found to correspond to the thermally activated delocalization of excitons in the InGaN quantum wells.

## References

- <sup>1</sup>D. Gerthsen, E. Hahn, B. Neubauer, A. Rosenauer, O. Schon, M. Heuken, and A. Rizzi, “Composition Fluctuations in InGaN Analyzed by Transmission Electron Microscopy”, *Physica status solidi (a)* **177**, 145–155 (2000).
- <sup>2</sup>P. Ruterana, S. Kret, A. Vivet, G. Maciejewski, and P. Dluzewski, “Composition fluctuation in InGaN quantum wells made from molecular beam or metalorganic vapor phase epitaxial layers”, *Journal of applied physics* **91**, 8979 (2002).
- <sup>3</sup>M. J. Galtrey, R. a. Oliver, M. J. Kappers, C. J. Humphreys, D. J. Stokes, P. H. Clifton, and A. Cerezo, “Three-dimensional atom probe studies of an In<sub>x</sub>Ga<sub>1-x</sub>N/GaN multiple quantum well structure: Assessment of possible indium clustering”, *Applied physics letters* **90**, 061903 (2007).
- <sup>4</sup>K. Okamoto and Y. Kawakami, “High-Efficiency InGaN/GaN Light Emitters Based on Nanophotonics and Plasmonics”, *Ieee journal of selected topics in quantum electronics* **15**, 1199–1209 (2009).
- <sup>5</sup>D. Behr, J. Wagner, a. Ramakrishnan, H. Obloh, and K.-H. Bachem, “Evidence for compositional inhomogeneity in low In content (InGa)N obtained by resonant Raman scattering”, *Applied physics letters* **73**, 241 (1998).
- <sup>6</sup>Y. Narukawa, Y. Kawakami, M. Funato, S. Fujita, S. Fujita, and S. Nakamura, “Role of self-formed InGaN quantum dots for exciton localization in the purple laser diode emitting at 420 nm”, *Applied physics letters* **70**, 981 (1997).
- <sup>7</sup>J. Jinschek, R. Erni, N. Gardner, A. Kim, and C. Kieselowski, “Local indium segregation and band gap variations in high efficiency green light emitting InGaN/GaN diodes”, *Solid state communications* **137**, 230–234 (2006).
- <sup>8</sup>H. Schömig, S. Halm, A. Forchel, G. Bacher, J. Off, and F. Scholz, “Probing Individual Localization Centers in an InGaN/GaN Quantum Well”, *Physical review letters* **92**, 106802 (2004).

- <sup>9</sup>D. Basko, G. La Rocca, F. Bassani, and V. Agranovich, “Förster energy transfer from a semiconductor quantum well to an organic material overlayer”, *The european physical journal b* **8**, 353–362 (1999).
- <sup>10</sup>T. Forster, “Energiewanderung und Fluoreszenz”, *Die naturwissenschaften* **33**, 166–175 (1946).
- <sup>11</sup>R. M. Clegg, “Forster resonance energy transfer-FRET what is it, why do it, and how it’s done”, in *Fret and flim techniques*, Vol. 33, edited by T. Gadella, 1st edition (Elesvier B.V., 2009), pages 1–57.
- <sup>12</sup>S. Rohrmoser, J. Baldauf, R. T. Harley, P. G. Lagoudakis, S. Sapra, A. Eychmuller, and I. M. Watson, “Temperature dependence of exciton transfer in hybrid quantum well/nanocrystal heterostructures”, *Applied physics letters* **91**, 092126 (2007).
- <sup>13</sup>G. Itskos, G. Heliotis, P. Lagoudakis, J. Lupton, N. Barradas, E. Alves, S. Pereira, I. Watson, M. Dawson, J. Feldmann, R. Murray, and D. Bradley, “Efficient dipole-dipole coupling of Mott-Wannier and Frenkel excitons in (Ga,In)N quantum well/polyfluorene semiconductor heterostructures”, *Physical review b* **76**, 035344 (2007).
- <sup>14</sup>J. Rindermann, G. Pozina, B. Monemar, L. Hultman, H. Amano, and P. Lagoudakis, “Dependence of Resonance Energy Transfer on Exciton Dimensionality”, *Physical review letters* **107**, 236805 (2011).
- <sup>15</sup>J. J. Rindermann, G. Pozina, B. Monemar, L. Hultman, H. Amano, and P. G. Lagoudakis, “The effect of exciton dimensionality on resonance energy transfer: advances for organic color converters in hybrid inorganic/organic LEDs”, in, Vol. 8255, edited by B. Witzigmann, M. Osinski, F. Henneberger, and Y. Arakawa (Feb. 2012), page 82550I.
- <sup>16</sup>J. Feldmann, G. Peter, E. Göbel, P. Dawson, K. Moore, C. Foxon, and R. Elliott, “Linewidth dependence of radiative exciton lifetimes in quantum wells”, *Physical review letters* **59**, 2337–2340 (1987).
- <sup>17</sup>S. F. Chichibu, Y. Kawakami, and T. Sota, “Emission Mechanisms and Excitons in GaN and InGaN Bulk and QWs”, in *Introduction to nitride semiconductor blue lasers and light emitting diodes*, edited by S. Nakamura and S. F. Chichibu (CRC PRESS, 2000), pages 153–270.
- <sup>18</sup>Y.-H. Cho, G. H. Gainer, a. J. Fischer, J. J. Song, S. Keller, U. K. Mishra, and S. P. DenBaars, “S-shaped temperature-dependent emission shift and carrier dynamics in In-GaN/GaN multiple quantum wells”, *Applied physics letters* **73**, 1370 (1998).
- <sup>19</sup>J.-H. Chen, Z.-C. Feng, H.-L. Tsai, J.-R. Yang, P. Li, C. Wetzel, T. Detchprohm, and J. Nelson, “Optical and structural properties of InGaN/GaN multiple quantum well structure grown by metalorganic chemical vapor deposition”, *Thin solid films* **498**, 123–127 (2006).

---

## Surface Passivation of InGaN/GaN MQW Nanorods and the Effect on Non-radiative Energy Transfer

---

### 7.1 Background

Although strong non-radiative energy transfer has been achieved as a result of using our nanorod structures as described in Chapter 4, it is still necessary to make further improvements in terms of practical applications. It is well-known that surface state issues exist in nanorod array structures, which is expected to significantly modify the band structure and thus the population of carriers such as excitons at the region between the InGaN/GaN MQWs and the F8BT, the critical area for the FRET process to occur. In order to effectively suppress the surface state issue, passivation of semiconductor surfaces is generally used in the fabrication of semiconductor devices. Bulk crystalline semiconductors are typically considered under the assumption of an infinite period potential created by the crystal lattice. When this lattice changes or stops, carriers in the material exhibit significantly modified behaviour. For a semiconductor surface, the potential is modified from that in the periodic lattice potential due to the presence of the surface bonds. These surface bonds form surface states and pin the Fermi level at the energy of these surface states. With the Fermi level pinned by surface states, a space charge is formed at the surface which not only significantly affects the carrier recombination dynamics of the material (so-called surface recombination, a non-radiative recombination through the surface states), but also modifies the band positions relative to the bulk semiconductor. The surface of both polar and non-polar GaN has been measured to exhibit upward band bending (increasing energy) at surfaces indicating that the band bending is due to charged surface states as opposed to the effects of polarization[1]. For GaN, this effect leads to electron depletion at the surface while the surface state effect causes InN to possess a surface electron accumulation layer as a result of the pinning of Fermi level at about 0.8eV above the

conduction band minimum. The transition between electron depletion and accumulation is predicted to occur at 30% indium composition, which is higher than the 16% used for the growth and fabrication of the blue emitting InGaN/GaN MQWs presented in this work [2].

Passivation of surface states involves the deposition of another material on the exposed surface to suppress the generation of surface states by the exposed bonds at the surface, reducing the Fermi pinning, and therefore the band bending. In conventional III-V semiconductors such as GaAs, surface state non-radiative recombination is very severe, and thus passivation of surface states is crucial [3]. The bond structure of GaN is a mixture of covalent and ionic, and is different from most conventional semiconductor materials that are significantly more covalent. This difference in bond structure influences the nature of the surface states and thus reduces the non-radiative recombination rate at surface states compared with GaAs [4].

Martinez et al. demonstrated that sulphur coatings can passivate surface states in GaN, which is similar to the GaAs system[5]. By means of the treatment of GaN surfaces with ammonium and sodium sulphide solutions, sulphide coatings were prepared on GaN surfaces, leading to a reduction in recombination at surface states and consequently an increase in PL intensity. Electrical measurements on the fabricated Schottky contacts to the passivated GaN shows that the passivation has effectively removed the effect of surface states on Fermi pinning at the surface. This highlights the potential for surface passivation techniques in effectively reducing or eliminating band bending at surfaces.

Typical surface passivation in semiconductor materials processing involves the use of dielectric materials such as silicon dioxide and silicon nitride deposited by chemical vapour deposition techniques. [6]. However, so far, there have only been a limited number reports on the passivation on III-nitride nanostructures[7, 8] without a clear consensus and of course, there are no studies of the passivation effect on the non-radiative energy transfer between inorganic semiconductor and organic semiconductor.

In this chapter, a new approach for the surface passivation on InGaN/GaN MQW nanorods has been developed, effectively suppressing the surface state, and significantly improving the FRET process between the InGaN/GaN MQW excitons and the F8BT excitons.

## **7.2 Sample Preparation and Optical Characterization**

In order to study the effect of surface passivation on the optical properties of InGaN/GaN MQW nanorods, a set of 10 periods of InGaN/GaN MQWs with blue emission were used. The structure is identical to that used in Chapter 6. Silicon nitride was deposited on the surface the InGaN/GaN MQW nanorod samples by PECVD. Silicon nitride was chosen as the passivation material as the precursor gasses  $\text{NH}_3$  and  $\text{SiH}_4$  will not lead to the formation of a native oxide layer on the GaN surface[6], simplifying the

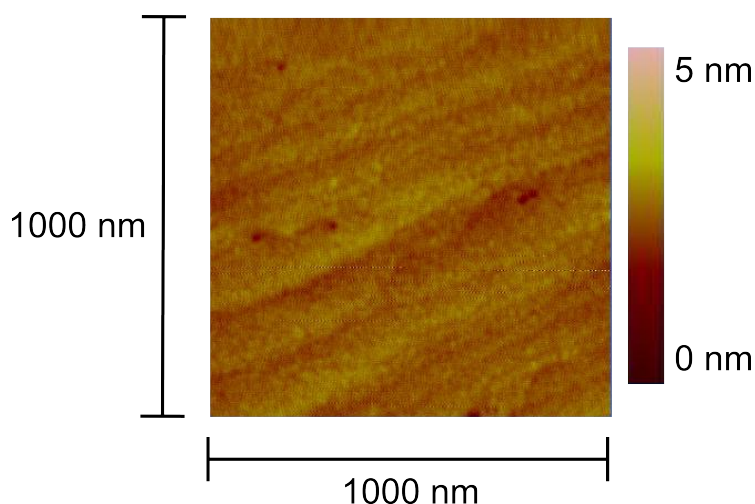


Figure 7.1: AFM image of a planar film of silicon nitride deposited on to GaN. The silicon nitride is visible as a roughening of the surface.

passivation mechanism. A range of different deposition times (0, 45, 60, 90, 180, 360 and 540 seconds) were used to control the layer thickness. Characterizing the thickness of films deposited on a three dimensional structures is challenging. In order to make an accurate estimation of film thickness, depositions were performed on planar substrates under identical conditions, characterized using ellipsometry. For the deposition on the planar substrates, the film thicknesses have been found to linearly depend on deposition time in a wide range from 8nm to 100nm . It is worth highlighting that the PECVD process is not completely isotropic and the deposition rate on vertical surfaces may be less than that on horizontal surfaces. Furthermore the shadowing effects of adjacent nanorods may also lead to a reduction in the rate of deposition on the sidewalls of the nanorods. An AFM image of the silicon nitride deposited on a planar GaN layer is shown in Figure 7.1. The deposited film is conformal as the two-dimensional lattice steps of the underlying GaN which is typical for our GaN grown using our high temperature AlN buffer are still visible. The surface rms roughness is increased from 0.1nm for the GaN to 0.2nm for the silicon nitride coated sample.

Photoluminescence measurements were carried out on the set of passivated nanorod samples with a 375nm laser diode as excitation source at room temperature, presented in Figure 7.2. It shows a significant improvement in the PL intensity as a result of increasing SiN thickness due to the passivation effect compared to the bare nanorod sample. In order further study the influence of the passivation on the optical properties, temperature dependent PL measurements have been carried out. The PL spectra were measured at both room temperature (300K) and low temperature (7K), where the ratio of the integrated PL intensity at 300K to that at 7K can be used to compare their IQE. It needs to be highlighted that the absolute value of IQE obtained though this approach is not accurate, but it is reasonable for the purposes of making comparisons as long as the measurements are performed under identical conditions, such as excitation power. The nominal IQE as a function of silicon nitride deposition thickness is presented in 7.3. Compared with the

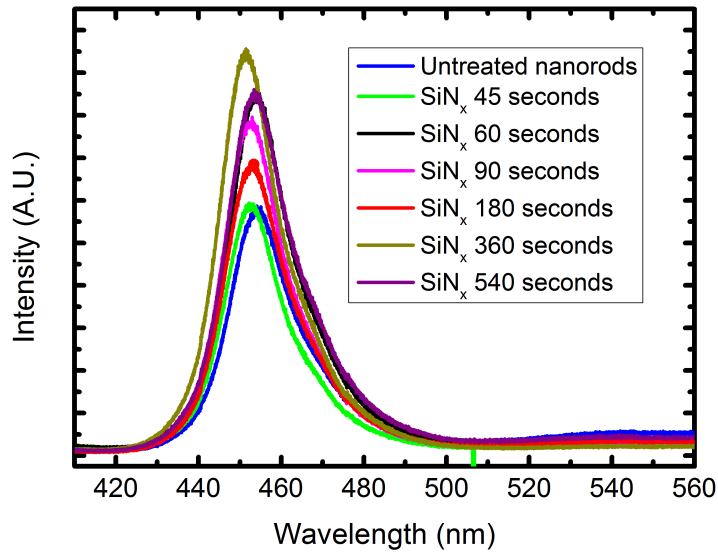


Figure 7.2: Room temperature PL spectra of the passivated InGaN/GaN MQW nanorod samples.

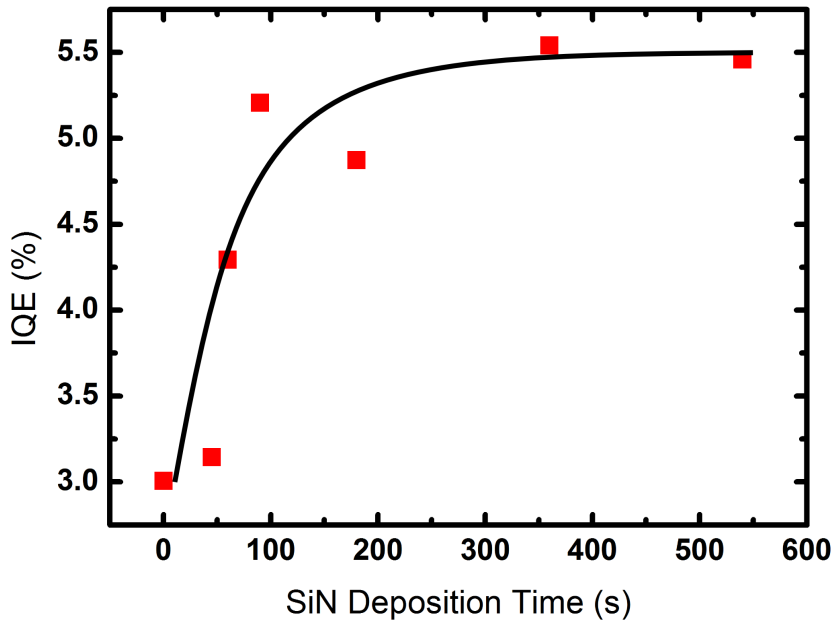


Figure 7.3: Internal quantum efficiency for InGaN/GaN MQW nanorods with different thicknesses of silicon nitride surface passivation. The IQE values were calculated based on the room temperature / low (7K) temperature integrated PL intensity ratios. A guide line for the eye is shown through the measured data points.



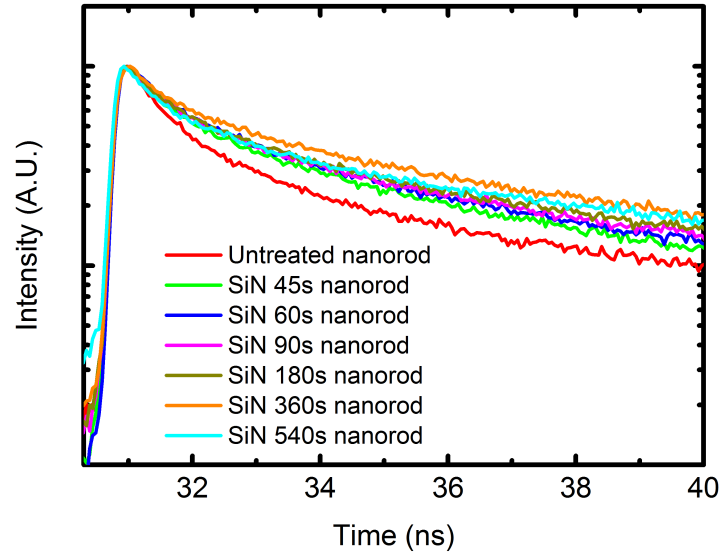


Figure 7.4: Room temperature TRPL of the InGaN/GaN MQW nanorods without treatment, and with various thicknesses of silicon nitride. The decay of the untreated sample is clearly faster than all of the treated samples.

untreated sample, the IQE of the samples coated with SiN quickly increases and saturates at an increased level by a factor of 1.8. Further increasing the SiN thickness beyond 90 seconds for the deposition will not lead to further improvement in IQE. TRPL measurements have also been performed on the set of passivated InGaN/GaN MQW nanorods and untreated nanorods at room temperature. The measured data is shown overlaid in Figure 7.4 and indicates that the untreated sample has faster decay than all of the treated samples. The recombination lifetimes of the samples are given in Figure 7.5, showing a clear increase in lifetime for the passivated MQW nanorod samples over the un-passivated sample, which is consistent with Figure 7.3. This behaviour also supports the conclusions drawn in Chapter 4, namely, the longer decay observed in the InGaN/GaN MQW nanorods than that of the as grown MQWs at room temperature is due to a reduction in non-radiative recombination.

### 7.3 Enhanced FRET due to Passivation of Nanorods

As the non-radiative energy transfer process studied in the hybrid InGaN/GaN MQW nanorods with F8BT coating is a short range effect, the effect of surface states could potentially be significant on the FRET process. A set of InGaN/GaN MQW nanorod samples have been fabricated in order to investigate this effect,. Silicon nitride films were deposited by PECVD with varying deposition times before spin coating F8BT onto the surface of the nanorods. A control set of samples were also prepared with identical silicon nitride deposition, with an insulating PMMA coating for comparison purposes.

Figure 7.7 shows the NRET rate of the hybrid InGaN/GaN MQW nanorod samples as

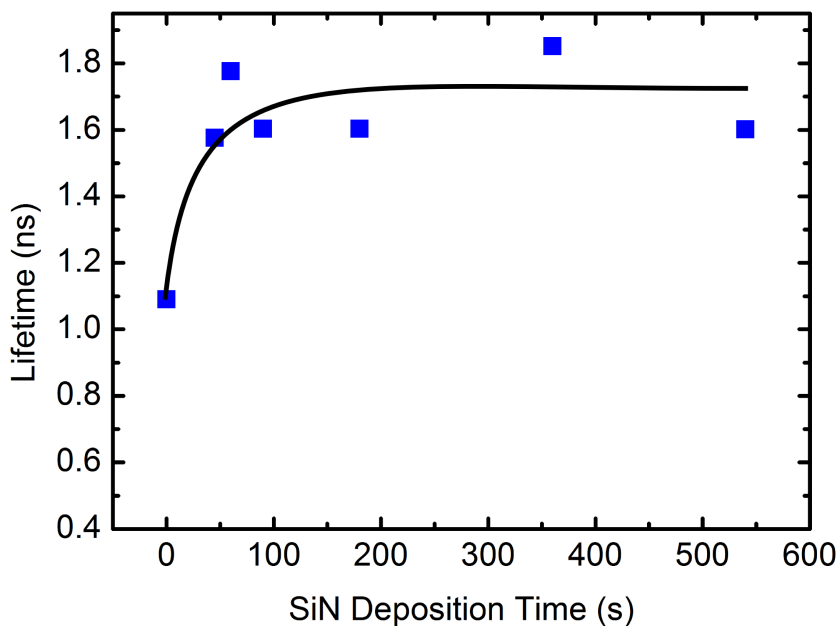


Figure 7.5: TRPL derived room temperature lifetimes of the InGaN/GaN MQW nanorod samples with silicon nitride deposition time. The lifetime of all passivated samples is increased compared to the untreated sample. A guide for the eye is shown with the measured data points.

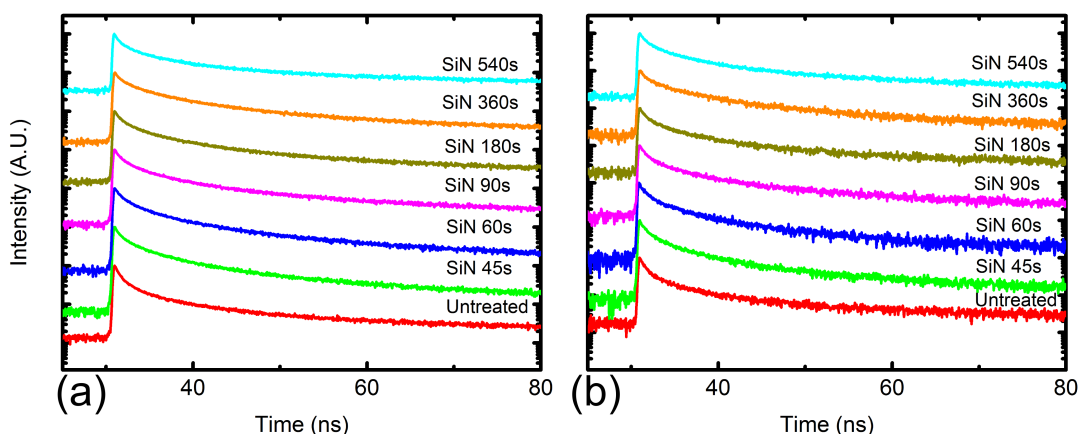


Figure 7.6: Room temperature TRPL of the InGaN/GaN MQW nanorods without treatment, and with various thicknesses of silicon nitride. (a) shows the decay of the PMMA coated control samples and (b) shows the decay if the hybrid F8BT coated samples.

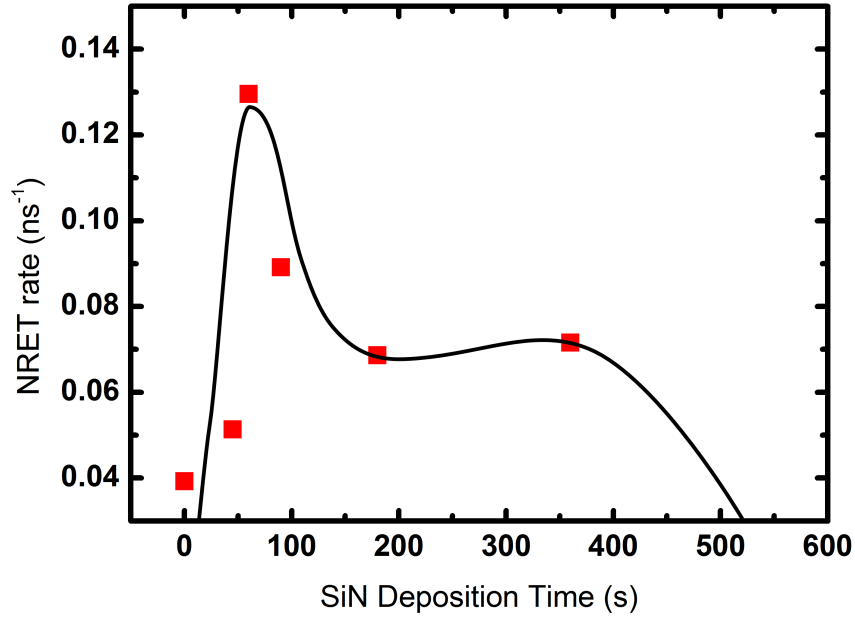


Figure 7.7: Non-radiative energy transfer rate of the hybrid InGaN/GaN MQW nanorod samples with silicon nitride passivation layer deposition time. The NRET rate increases with silicon nitride passivation thickness, with an apparent peak for 60 seconds of silicon nitride deposition. A guide for the eye is draw through the data points.

a function of SiN deposition time, indicating that the NRET rate increases with increasing the silicon nitride deposition time (equivalent to increasing passivation thickness) up to 60 seconds and then reduces with further increasing the deposition time. A remarkable increase in the NRET rate can be seen, with NRET rate enhanced by a factor of more than 3 compared with the untreated sample, meaning that the deposition of SiN massively enhances the energy transfer between the InGaN/GaN excitons and the F8BT excitons

Due to the large exposed surface area of nanorod structures, surface states and surface effects can potentially play a significant role in the carrier dynamics. Chan et al. attributed the long PL decay components of InGaN MQW nanorods to trapping of carriers in surface traps as a consequence of the presence of surface states[9]. Calarco et al. investigated surface states in GaN nanowires grown by MBE[10] and performed photo-conductivity measurements on a number of individual GaN nanowires with different diameters. For small nanowire diameters the photo-conductivity was found to increase exponentially with nanowire diameter up to a threshold diameter, above which the photo-conductivity increases linearly with further increasing diameter. A simple model based on surface states has been proposed in order to explain these two different kinds of behaviour. As a result of surface states, both the conduction and valence bands are proposed to bend to higher energies than in the bulk due to the space charge generated by pinning effect, and thus this band bending leads to the formation of an electron depletion region at the surface of the nanowires. The width of this depletion region depends on the diameters of the nanowire, for example, thin nanowires do not allow the bands to return to the bulk

Image not available in electronic version.  
Please find original at citation in the text.

Figure 7.8: Schematic of the band structure as a function of nanowire diameter[10]. For nanowires with diameters greater than the critical diameter, a neutral, bulk-like region exists in the nanowire centre.

level (the level in the centre of the nanorods), while above a critical diameter, the bands are able to return to the bulk band energies. This is shown schematically in Figure 7.8 by Calarco et al. The increasing barrier height with increasing nanorod diameter is responsible for the initial exponential increase in photoconductivity as the barrier to non-radiative recombination at surface states increases. Further increases in nanowire diameter above the critical diameter does not lead to a further rise in the barrier height. For the self assembled nanorods presented in this thesis, typical diameters are 220nm, significantly larger than the critical diameter, which is 80-100nm, reported by Calarco et al. This implies that the bands in the self assembled nanorods studies in this thesis are likely to be fully bent.

## **7.4 Dependence of Energy Transfer on Surface State Passivation**

The deposition of SiN on the surface of sidewalls of the nanorods is expected to generate two effects: (1) passivate surface states; (2) increase the spatial separation between the InGaN/GaN MQW excitons and the F8BT excitons.

The passivation is expected to enhance the FRET process. As pointed out by Calarco et al., the existence of surface states pins the Fermi level, leading to band bending and a depletion region at the surface of GaN nanorods[10]. This depletion region will effectively increase the separation between the excitons from InGaN/GaN MQW and the F8BT excitons. Therefore, this depletion region is very significant in terms of hybrid structures, as this is also the region where FRET is most significant (due to the short range of the FRET process).

The influence of the passivation on the band structure is depicted schematically in

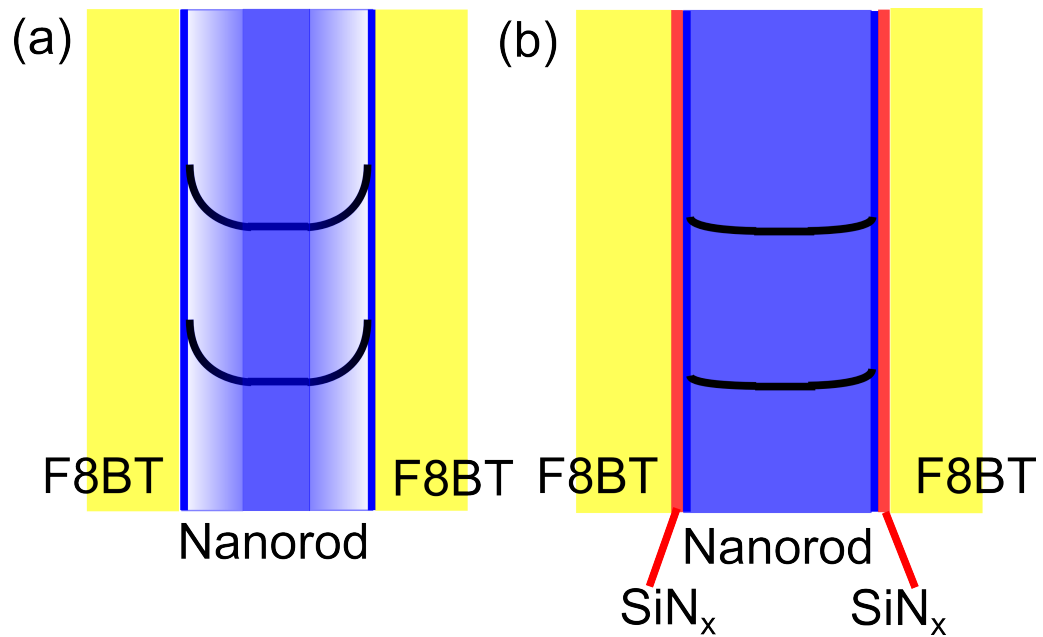


Figure 7.9: A schematic showing a nanorod with F8BT coating. (a) is a hybrid nanorod with no passivation, the band bending due to surface states leads to depletion in the edges on the nanorod where FRET is most likely. (b) shows a hybrid nanorod with silicon nitride passivation, with the surface states passivated the band bending and depletion is reduced, increasing the carrier density in the high FRET region of the outer ring of the nanorod.

Figure 7.9. Figure 7.9 (a) shows that the depletion region (without passivation) leads to an increase in the effective separation between the InGa<sub>0.5</sub>N<sub>0.5</sub>/Ga<sub>0.5</sub>N MQWs and the F8BT, while Figure 7.9 (b) clearly demonstrates that the silicon nitride passivation effectively suppresses the surface states, leading to a significant reduction in band bending. Firstly, this will facilitate an increase in the exciton population in the outer region of the nanorods, generating a higher population of carriers which can be involved in the FRET process. Secondly, it also leads to a reduction in the effective separation between the InGa<sub>0.5</sub>N<sub>0.5</sub>/Ga<sub>0.5</sub>N MQWs and the F8BT, thus enhancing the FRET process.

On the one hand, longer deposition times of SiN (thicker films) is expected to enhance the passivation effect, in particular, for our case where the SiN needs to be deposited on the surface of the Nanorod sidewalls. On the other hand, a thicker SiN layer will reduce the FRET process due to an increase in the effective separation, as the FRET is very sensitive to the separation and the typical working range is around 10nm. The expected behaviour of FRET with increasing passivation layer thickness is expected to be a competition, between the initial increase of FRET due to passivation of surface states and reduction in the FRET rate due to the spatial separation induced by the presence of the passivation layer. This behaviour describes an optimum thickness of SiN, where the NRET rate will be a maximum, with lower NRET rates with either thinner films (due to unpassivated surface states) or thicker films (increased exciton separation due to the SiN barrier). This behaviour can clearly be seen in Figure 7.7, where the untreated sample shows low NRET rate, with NRET reaching a maximum for samples with a 60 second SiN deposition, before dropping for samples with longer SiN deposition times.

The effect of the silicon nitride on the nanorod surfaces is not only to passivate surface states, but with increasing thickness of silicon nitride, the separation between MQW excitons and F8BT excitons will increase. As shown in Chapters 5 and 6, increasing the exciton separation will reduce the FRET rate. The expected behaviour of FRET with increasing passivation layer thickness is expected to be a competition, between the initial increase of FRET due to passivation of surface states and reduction in the FRET rate due to the spatial separation induced by the presence of the passivation layer. In-order to understand this competition, the effectiveness of the passivation by silicon nitride in reducing band bending and the exact exciton separation dependence of FRET in these three dimensional structures needs to be quantitatively known. As a focus of further research, more extensive passivation studies using different thicknesses of passivation layer and different passivation materials are required.

## 7.5 Summary

A simple passivation process for application in the fabrication of the hybrid organic polymer and InGaN/GaN nanostructures has been developed, leading to a significant suppression in surface states, and thus a significant enhancement in the FRET between InGaN/GaN MQW excitons and the F8BT excitons. The efficiency of the FRET can be increased by a factor more than three compared with the structure without the passivation process. A simple model based on surface state has been established, supporting the conclusion.

## References

- <sup>1</sup>S. Chevtchenko, X. Ni, Q. Fan, a. a. Baski, and H. Morkoc, “Surface band bending of a-plane GaN studied by scanning Kelvin probe microscopy”, *Applied physics letters* **88**, 122104 (2006).
- <sup>2</sup>T. D. Veal, P. H. Jefferson, L. F. J. Piper, C. F. McConville, T. B. Joyce, P. R. Chalker, L. Considine, H. Lu, and W. J. Schaff, “Transition from electron accumulation to depletion at InGaN surfaces”, *Applied physics letters* **89**, 202110 (2006).
- <sup>3</sup>C. K. Yong, K. Noori, Q. Gao, H. J. Joyce, H. H. Tan, C. Jagadish, F. Giustino, M. B. Johnston, and L. M. Herz, “Strong carrier lifetime enhancement in GaAs nanowires coated with semiconducting polymer.”, *Nano letters* **12**, 6293–301 (2012).
- <sup>4</sup>A. Costales, M. a. Blanco, A. Martin Pendas, A. K. Kandalam, and R. Pandey, “Chemical Bonding in Group III Nitrides”, *Journal of the american chemical society* **124**, 4116–4123 (2002).
- <sup>5</sup>G. L. Martinez, M. R. Curiel, B. J. Skromme, and R. J. Molnar, “Surface recombination and sulfide passivation of GaN”, *Journal of electronic materials* **29**, 325–331 (2000).

- <sup>6</sup>S. a. Chevtchenko, M. a. Reshchikov, Q. Fan, X. Ni, Y. T. Moon, a. a. Baski, and H. Morkoc, “Study of SiNx and SiO<sub>2</sub> passivation of GaN surfaces”, *Journal of applied physics* **101**, 113709 (2007).
- <sup>7</sup>C. Shi, C. Zhang, F. Yang, M. J. Park, J. S. Kwak, S. Jung, Y.-h. Choi, X. Wang, and M. Xiao, “Reducing the efficiency droop by lateral carrier confinement in InGaN/GaN quantum-well nanorods”, *Applied physics letters* **101**, 18 (2013).
- <sup>8</sup>L.-Y. Chen, H.-H. Huang, C.-H. Chang, Y.-Y. Huang, Y.-R. Wu, and J. Huang, “Investigation of the strain induced optical transition energy shift of the GaN nanorod light emitting diode arrays.”, *Optics express* **19 Suppl 4**, A900–7 (2011).
- <sup>9</sup>C. C. S. Chan, B. P. L. Reid, R. a. Taylor, Y. Zhuang, P. a. Shields, D. W. E. Allsopp, and W. Jia, “Optical studies of the surface effects from the luminescence of single GaN/InGaN nanorod light emitting diodes fabricated on a wafer scale”, *Applied physics letters* **102**, 111906 (2013).
- <sup>10</sup>R. Calarco, M. Marso, T. Richter, A. I. Aykanat, R. Meijers, A. V D Hart, T. Stoica, and H. Lüth, “Size-dependent photoconductivity in MBE-grown GaN-nanowires.”, *Nano letters* **5**, 981–4 (2005).





---

## Conclusions and Further Work

---

### 8.1 Summary of Results

#### InGaN/GaN Nanorod Arrays

A post growth nanorod fabrication process was employed to fabricate nanorod arrays using InGaN/GaN MQW wafers. The process involves the deposition of SiO<sub>2</sub> followed by a thin Ni layer on the surface of the wafer. Thermal annealing causes the Ni film to self-organize into nanoislands, which can then act as an etch mask. Reactive ion etching followed by inductively coupled plasma etching are used to etch through the MQW layer resulting in arrays of MQW nanorods.

Fabrication of these array structures results in significantly increased room temperature photoluminescence intensity compared to the as-grown wafer. The room temperature IQE was measured to increase significantly compared to the as-grown wafers for InGaN/GaN MQWs at emission wavelengths from violet to green. The increase in PL intensity is accompanied by a blue-shift in emission wavelength. This correlates with strain relaxation observed in the InGaN MQW nanorods confirmed by XRD RSM measurements.

Time resolved PL measurements highlighted that the room temperature PL lifetime of the MQW nanorod structures is significantly enhanced compared to the as grown wafer. This indicates a significant reduction in non-radiative recombination in the nanorod structures. A model based on the reduction of excitonic diffusion to non-radiative recombination centres by lateral confinement of the nanorod structures was proposed to account for this behaviour.

## **Hybrid Organic/Inorganic Nanorod Structures Using Non-radiative Energy Transfer**

Using the InGaN/GaN MQW nanorod arrays, hybrid structures were fabricated by depositing a light emitting polymer surrounding the nanorods. Combining blue emitting MQW nanorods and yellow emitting light emitting polymer produced a novel white light emitting structure. These novel structures exhibit efficient non-radiative energy transfer (NRET) from the MQWs to the light emitting polymer. The NRET process is a near-field effect and as such is limited to short range (typically  $< 10\text{nm}$ ), the nanorod structure efficiently allows the separation of MQW and light emitting polymer to be reduced to within this range. Time resolved PL measurements show a significantly increased PL decay rate in the hybrid MQW nanorods compared to the as etched MQW nanorods. This decrease is attributed to the additional non-radiative decay channel as energy is non-radiatively transferred to the light emitting polymer. The NRET efficiency was calculated to be 73% after being corrected for the volume contribution of the near-field region.

### **The Influence of Exciton Localization on Non-radiative Energy Transfer**

Due to the direct excitonic coupling of NRET, the dimensionality of excitons in the InGaN MQWs can affect the energy transfer process. The dimensionality of InGaN MQW excitons can be changed from localized to delocalized by thermally activating the localization centres with increasing temperature. Temperature dependent time resolved PL measurements showed that the NRET efficiency increases by a factor of 6.7 from 7K to 300K. The delocalized excitons at room temperature exhibit significantly higher energy transfer efficiency than the localized excitons at cryogenic temperatures.

### **Passivation of Nanorod surfaces and Increased Non-radiative Energy Transfer Efficiency**

Due to the large exposed surface area of the nanorod arrays, surface states are a potential issue. A surface passivation technique was used, namely, deposition of a thin layer of SiN on the surface of nanorod arrays. The passivated MQWs showed an increased room temperature IQE compared to unpassivated samples. An increase in room temperature PL lifetime for the passivated samples indicates that non-radiative surface recombination is partially quenched.

The passivation technique was applied to fabricate hybrid structures where a SiN layer was deposited on the nanorod surfaces before deposition of the light emitting polymer layer. Varying the SiN thickness demonstrated, at optimum thickness, a three fold increase in the energy transfer efficiency of the hybrid structures compared to the unpassivated samples. A model based on a reduction of band bending at the surface caused by surface state passivation is proposed. The reduction in surface band bending reduces the surface depletion region, increasing the density of carriers in the outer region of the

nanorods, hence reducing effective exciton separation. This reduction in separation leads to increased energy transfer efficiency. Increasing the thickness of SiN further, reduces then energy transfer efficiency and is understood by increasing the physical separation.

## 8.2 Further Work

This project has demonstrated the benefits of the nanorod structures which can dramatically improve the optical properties of InGaN/GaN MQWs. The fabrication of nanorod arrays also lead to the fabrication of hybrid organic/inorganic white light emitters with high efficiency non-radiative energy transfer. The non-radiative energy transfer process allows for potentially higher efficiency white LEDs. In order to extend this work the next major landmark is the fabrication of an electrically injected hybrid white light emitting device based on these novel hybrid nanorod arrays. Previous work by the group in Sheffield has demonstrated the ability to fabricate electrically injected MQW nanorod array LEDs. In order to fabricate electrically injected hybrid devices the main challenge is to complete the processing required to fabricate an inorganic nanorod LED (contact deposition, annealing) within the limitations of the stability of the organic material. This will require processing to be carried out without the presence of oxygen. The temperature stability of organic materials also requires consideration. The wide variety of organic materials available, and yet to be investigated, may allow material with better thermal stability to be chosen. In order to achieve the best results, a compromise will be required on the contact annealing temperature. Further research is needed on the fabrication of Ohmic contacts at low temperature for the hybrid structures. The use of Pd/Au metals without a thermal annealing process can be used to produce ohmic contacts on p-GaN and is a promising technique for application to these novel structures. To improve the performance of these hybrid devices the use of blends of various polymer materials could be used. This will allow precise tuning of the colour quality of the emission of the devices.

Further work is required to better understand the nature of the energy transfer process, such as the difference in the temperature dependence of the energy transfer efficiency and energy transfer rate in the hybrid structures. Based on the work in this thesis the differences are most likely related to the change in excitonic diffusion length as a result of the lateral confinement of the nanorod structures. In order to investigate this it is recommended that nanorods with different diameters are fabricated to enable the investigation of the temperature dependence of NRET rate and efficiency. This would allow the influence of the nanorod lateral confinement on the energy transfer process to be isolated.

The passivation process could be further improved by using other passivation techniques. The use of a technique such as atomic layer deposition (ALD) would allow very accurately controlled deposition thicknesses of passivating materials. Alternative passivation processes such as chemical treatments would also be worth investigating. The typical process for surface passivation in III-V materials is the use of sulphides. This technique

would allow the passivation of surface states without the inclusion of a significant thickness of passivation material and is therefore of particular interest for the passivation of hybrid structures.

---

## List of Figures

---

1.1	The phase out of inefficient incandescent lighting sources brought into effect by European legislation [6] . . . . .	14
1.2	The luminous efficacies of various lighting technologies plotted for the year of their development by Narukawa et al. [4] . . . . .	15
1.3	The bandgap energies of various semiconductors plotted against their lattice constants . . . . .	16
1.4	The number of papers published with keywords GaN as a function of publication year from Akasaki and Amano [21] . . . . .	18
1.5	Efficiency droop of InGaN MQW based LEDs of various wavelengths by Cho et al. [41] . . . . .	21
1.6	An image from Krames et al. [50] showing the quantum efficiencies of LEDs of different materials systems at various wavelengths. The so called "green gap" between high efficiency blue and red emitting LEDs is clear. With the human eye responsivity plot centred in the green/yellow spectral region . . . . .	22
2.1	A schematic showing the simplified band structure of a direct and an indirect semiconductor . . . . .	30
2.2	Possible carrier excitation and relaxation mechanisms. (a) absorption of a photon with $E > E_g$ (b) Spontaneous emission from band edge (c) Excitonic recombination (d) Donor acceptor recombination (e) Non-radiative recombination via defects or deep level states . . . . .	33
2.3	An InGaN/GaN quantum well with schematic electron and hole wavefunctions shown in the conduction and valence bands respectively . . . . .	35
2.4	Band structures of an un-doped semiconductor, an unbiased p-n junction and a p-n junction under forward bias . . . . .	36

2.5	An InGaN/GaN quantum well the effect of the quantum confined Stark effect on schematic electron and hole wavefunctions shown as the bands are tilted and the wavefunction overlap is reduced . . . . .	38
2.6	Localization shown in the conduction band as a function of position . . .	40
2.7	The HOMO and LUMO bands of a molecule, with optical transitions displayed, absorption of a photon of energy $\hbar\omega$ , non-radiative relaxation, and radiative recombination with release of phonon with energy $\hbar\omega'$ . . .	42
2.8	Bonded carbon atoms in a chain, showing the $\pi$ orbitals and the delocalized, conjugated $\pi$ orbitals that allow carrier transport . . . . .	42
2.9	A schematic taken from [40], showing their non-radiative energy transfer pumped white emitting structure. With InGaN quantum well excitons non-radiatively coupled to down converting quantum dots through the thin top barrier layer. Re-printed from Nature Publishing . . . . .	43
2.10	An image from [42], showing a schematic of the two nanostructured samples designed to couple InGaN quantum wells to nanocrystal quantum dots by non-radiative energy transfer. . . . .	44
3.1	A schematic diagram of the photoluminescence excitation system built for this work . . . . .	53
3.2	Low temperature PL and PLE of three InGaN MQW samples with different quantum well growth times and therefore different quantum well widths. A sigmoidal fit to the InGaN absorption edge is show for the two samples with larger Stokes like shift . . . . .	53
3.3	A schematic diagram of the time correlated single photon counting system set up for this work . . . . .	54
3.4	Typical decay profile for an InGaN MQW sample, plotted in log scale, the non-mono-exponential shape is apparent . . . . .	55
3.5	The Witec confocal system, with Princeton instruments monochromator and Andor CCD. . . . .	58
3.6	The glovebox used to spin coat light emitting polymer materials in an oxygen free atmosphere. . . . .	60
4.1	AFM images of the GaN surface for a conventional two-step growth (left) and the high temperature AlN buffer technique used in Sheffield (right). .	65
4.2	XRD rocking curves showing the increase in crystal quality of GaN films grown on the high temperature AlN buffer compared to GaN films grown using the standard two-step growth technique. The rocking curve of the high temperature AlN buffer layer is shown on the right. . . . .	65
4.3	A schematic of the structure of the typical InGaN/GaN 10 quantum well sample grown in Sheffield used in this work (not to scale). . . . .	66

4.4	XRD $\omega - 2\theta$ scan data showing an as grown epi-wafer with 10 InGaN quantum wells with GaN barrier layers. The GaN, InGaN and AlN peaks as visible along with satellite peaks. The results of fitting are shown in Table 4.1 . . . . .	67
4.5	Photoluminescence measurements of the InGaN/GaN 10 quantum well as grown wafer (a) at a sample temperature of 12K with an peak emission wavelength of 452.8nm and (b) at room temperature with a peak emission wavelength of 444.2nm . . . . .	68
4.6	(a) Temperature dependent time integrated PL spectra with PL intensity decreasing with increasing temperature. (b) An Arrhenius plot of Integrated PL intensity against $1000/T$ showing the reduction in PL intensity with increasing temperature . . . . .	69
4.7	Temperature dependent peak emission energy for the 10 quantum well InGaN/GaN sample. A characteristic s-shift can be seen, with an initial red-shift from $T = 12K$ to $T = 90K$ followed by a blue-shift until $T = 200K$ where emission red-shifts again until room temperature. . . . .	70
4.8	Time resolved photoluminescence data measured for the blue emitting InGaN 10 quantum well described previously. TRPL decay traces are plotted at different sample temperatures with a clear difference in behaviour from long, slow decay at low temperature (12K) to very fast decay at room temperature (300K). . . . .	71
4.9	The PL decay, radiative and non-radiative lifetimes of the InGaN/GaN 10 quantum well sample are presented as a function of temperature. . . . .	72
4.10	A schematic showing the nanorod fabrication procedure used . . . . .	73
4.11	(a) SEM image of a self assembled array of Ni nanoislands after thermal annealing, for use as a dry etch mask. (b) SEM image of SiO <sub>2</sub> nanorods, after RIE etch . . . . .	74
4.12	SEM images of the etched nanorods, with typical diameters of 220nm . . . . .	74
4.13	Photoluminescence of an InGaN MQW as-grown epiwafer compared with the sample after the fabrication of a nanorod nanorod array . . . . .	75
4.14	Time integrated PL spectra of the three InGaN/GaN MQW nanorod samples with emission wavelengths in the violet, blue and green spectral regions. The corresponding as-grown epiwafer samples are shown in black. All nanorod samples show an increase in PL intensity and a blueshift in emission wavelength. . . . .	76

4.15	X-ray diffraction reciprocal space map (RSM) of the (a) as-grown green emitting MQW wafer and the (b) corresponding nanorod sample. The as grown wafer shows the InGaN satellite peak positions in allong the fully strained line, showing the InGaN MQWs are fully strained to the GaN barrier lattice constant. The nanorod sample shows the InGaN satellite peak positions between the fully strained and fully relaxed lines indicating partial strain relaxation in the InGaN MQWs. . . . .	77
4.16	Room temperature TRPL traces for the set of MQW nanorods with violet, blue and green emission wavelengths. It is clear that the nanorod samples all show longer decay profiles than their corresponding as grown samples.	77
4.17	Time resolved photoluminescence of InGaN/GaN MQW nanorods at different temperatures. a), b) and c) are violet, blue and green emission wavelengths respectively . . . . .	78
4.18	The TRPL of the series of InGaN/GaN MQW nanorods as a function of temperature after processing to extract the PL, radiative and non-radiative lifetimes. . . . .	79
4.19	The ratio of the radiative and non-radiative lifetimes for the set of violet (a), blue (b) and green (c) emitting InGaN/GaN MQWs. The ratios for the as-grown wafer are compared to the ratios after nanorod fabrication. .	80
4.20	The measured TRPL lifetimes as a function of wavelength for the set of InGaN/GaN MQW nanorod samples with emission wavelengths from violet (a) and blue (b) to green (c). . . . .	81
4.21	A schematic of the effect of lateral confinement on non-radiative recombination. Non-radiative recombination centres are shown in red, it is possible for carriers to migrate to these centres and recombine in the planar structure (a), nanorods however (b), spatially confine carriers, potentially reducing non-radiative recombination . . . . .	82
5.1	The structure of the polyfluorene co-polymer used in this work F8BT. The F8 unit is on the left with the BT unit on the right. . . . .	94
5.2	The absorption and emission properties of a layer of F8BT deposited on a sapphire substrate from a solution of toluene . . . . .	95
5.3	Photoluminescence of an F8BT film deposited on a single GaN layer on sapphire measured at intervals of 2 – 3 minutes with constant laser exposure. The F8BT film was deposited and measured in air, excitation is with a 375nm laser diode operating at 4mW power in CW mode. A decrease of 68% in peak intensity is observed. The discontinuities are from degradation that occurs between CCD acquisitions as the monochromator scans to a new centre wavelength . . . . .	96



5.4	Photoluminescence of an F8BT film deposited on a single GaN layer on sapphire measured at intervals of 2 – 3 minutes with constant laser exposure. The F8BT film was deposited in a glovebox environment with O <sub>2</sub> levels < 0.5ppm, PL measurement was carried out in a vacuum of (10 <sup>-6</sup> Torr), excitation is with a 375nm laser diode operating at 4mW power in CW mode. No evidence of degradation is observed . . . . .	97
5.5	(a) SEM image of a scratched F8BT film deposited on GaN from a solution of F8BT in toluene with a concentration of 20mg/ml (b) AFM image of the same sample (c) AFM profile measurement used to determine the film thickness . . . . .	97
5.6	(a) a schematic of the hybrid InGaN/GaN MQW nanorod / F8BT structure fabricated, the F8BT is deposited directly onto the nanorod array, minimizing MQW-F8BT separation. (b) This allows for the possibility of FRET between MQW and light emitting polymer. . . . .	98
5.7	(a) SEM cross-sectional image of an F8BT coated nanorod array with nanorod etching depth of 400nm, It is clear that the F8BT is not in contact with the entire nanorod sidewall and that voids are present at the base of the nanorods (b) F8BT coated Nanorods with an etch depth of 800nm showing complete coverage by the F8BT over the entire nanorod sidewalls	99
5.8	Photoluminescence spectra of the MQW emission peak of a bare InGaN/GaN MQW nanorod sample with the corresponding hybrid MQW nanorod sample with an overlayer of F8BT . . . . .	100
5.9	The TRPL decay traces of the bare MQW nanorod sample and the MQW nanorod hybrid sample. The detection wavelength is the MQW emission peak . . . . .	101
5.10	A schematic showing a nanorod of typical diameter 220nm with an outer radius where NRET is possible and an inner radius where the separation between MQW excitons and a the F8BT surrounding the nanorod is too large to allow NRET . . . . .	103
5.11	The absorption spectrum of an F8BT film and the PL emission of the green emitting MQW nanorods, The overlap of emission and absorption is very low, leading to low resonance and therefore low probability of FRET.	103
5.12	The TRPL decay traces of the bare green emitting MQW nanorod sample and the green emitting MQW nanorod hybrid sample. The detection wavelength is the MQW emission peak. The overlapping F8BT decay trace has been removed in the fitting process . . . . .	104
5.13	Confocal photoluminescence maps showing integrated PL intensity of both the MQW emission (a) and the F8BT emission (b). A clear segregation is visible with the MQW emission localized to the MQE nanorods and F8BT emission the inverse of this. . . . .	105

5.14	An overlay of the confocal PL mapping of the integrated PL intensities of InGaN blue MQW emission (Blue) and F8BT yellow emission (Yellow). Showing the mixture of blue and yellow luminescence . . . . .	105
6.1	A figure by Rindermann et al. showing schematically the distribution of exciton wavevectors for localized and free excitons[15] . . . . .	112
6.2	The temperature dependent recombination lifetime of InGaN/GaN MQW nanorods. The lifetime increases slightly from 10K to 70K where drops quickly until a temperature of 140K where the rate of lifetime reduction is reduced. A line to guide the eye is shown through the measured data points. . . . .	113
6.3	(a) an Arrhenius plot of the integrated PL intensity of the PMMA coated control InGaN/GaN MQW nanorod sample yielding an activation energy corresponding to a temperature of 160K. (b) the PL full width at half maximum values as a function of temperature, a turning point is clear at a temperature of 150K corresponding to significant degree of de-localization of excitons in the InGaN MQWs . . . . .	114
6.4	The measured TRPL decay data at various temperatures for the InGaN/GaN MQW nanorods in the control sample: PMMA coated nanorods (a) and hybrid sample: F8BT coated nanorods (b). The intensities at different temperatures have been offset for clarity. . . . .	115
6.5	The decay rate of both PMMA coated MQW nanorod control sample and F8BT coated hybrid MQW nanorod sample as a function of temperature. A clear difference in the temperature dependence is visible at temperatures above 70K. . . . .	115
6.6	Temperature dependent non-radiative energy transfer rate. The rate is initially low until a temperature of 80K where the rate increases before saturating at a temperature of 230K. A guide for the eye is drawn through the data points. . . . .	116
6.7	Non-radiative energy transfer efficiency as a function of temperature for hybrid nanorod samples. A sigmoidal fit is also plotted to extract a maximum gradient at a temperature of 70K corresponding to the onset of significant thermal de-localization of MQW excitons. . . . .	116
7.1	AFM image of a planar film of silicon nitride deposited on to GaN. The silicon nitride is visible as a roughening of the surface. . . . .	123
7.2	Room temperature PL spectra of the passivated InGaN/GaN MQW nanorod samples. . . . .	124

7.3	Internal quantum efficiency for InGaN/GaN MQW nanorods with different thicknesses of silicon nitride surface passivation. The IQE values were calculated based on the room temperature / low (7K) temperature integrated PL intensity ratios. A guide line for the eye is shown through the measured data points. . . . .	124
7.4	Room temperature TRPL of the InGaN GaN MQW nanorods without treatment, and with various thicknesses of silicon nitride. The decay of the untreated sample is clearly faster than all of the treated samples. . . .	125
7.5	TRPL derived room temperature lifetimes of the InGaN/GaN MQW nanorod samples with silicon nitride deposition time. The lifetime of all passivated samples is increased compared to the untreated sample. A guide for the eye is shown with the measured data points. . . . .	126
7.6	Room temperature TRPL of the InGaN GaN MQW nanorods without treatment, and with various thicknesses of silicon nitride. (a) shows the decay of the PMMA coated control samples and (b) shows the decay if the hybrid F8BT coated samples. . . . .	126
7.7	Non-radiative energy transfer rate of the hybrid InGaN/GaN MQW nanorod samples with silicon nitride passivation layer deposition time. The NRET rate increases with silicon nitride passivation thickness, with an apparent peak for 60 seconds of silicon nitride deposition. A guide for the eye is draw through the data points. . . . .	127
7.8	Schematic of the bans structure as a function of nanowire diameter[10]. For nanowires with diameters greater than the critical diameter, a neutral, bulk-like region exists in the nanowire centre. . . . .	128
7.9	A schematic showing a nanorod with F8BT coating. (a) is a hybrid nanorod with no passivation, the band bending due to surface states leads to depletion in the edges on the nanorod where FRET is most likely. (b) shows a hybrid nanorod with silicon nitride passivation, with the surface states passivated the band bending and depletion is reduced, increasing the carrier density in the high FRET region of the outer ring of the nanorod. . . .	129